Dynamic Polarizability and Collective Modes in Narrow-Band Electron Systems

by

Cyprian Lewandowski

MSci & ARCS in Physics with Theoretical Physics, Imperial College London (2015)

Submitted to the Department of Physics
in partial fulfillment of the requirements for the degree of

Doctor of Philosophy

at the

MASSACHUSETTS INSTITUTE OF TECHNOLOGY

June 2020

Author .....
Department of Physics
May 13, 2020

Certified by .....
Leonid S. Levitov
Professor of Physics
Thesis Supervisor

Accepted by .....
Nergis Mavalvala
Professor of Physics, Associate Department Head

Dynamic Polarizability and Collective Modes in Narrow-Band Electron Systems

by

Cyprian Lewandowski

Submitted to the Department of Physics
on May 13, 2020, in partial fulfillment of the
requirements for the degree of
Doctor of Philosophy

Abstract

The family of moiré materials, in particular the magic angle twisted bilayer graphene, has emerged recently as a platform to study strongly interacting physics. This thesis analyzes the impact of the ultranarrow Bloch bands and strong electron-electron interactions on the dynamical polarization response of these systems. Strong interactions alter the collective charge dynamics in a number of interesting ways, in particular by stiffening the frequency-momentum dispersion of surface plasmons and making it much stronger than that of the underlying narrow-band carriers. Strongly dispersing plasmons pierce through the particle-hole continuum and extend in the forbidden energy band above it. This behavior enables decoupling of plasmons from particle-hole excitations. Such over-the-band plasmons are unable to decay into particle-hole pairs and thus are not subject to Landau damping. As a result, plasmons acquire longer lifetimes as well as an enhanced spatial optical coherence. The optical coherence manifests itself in spatial interference patterns that provide telltale signatures of over-the-band plasmons that are readily accessible in near-field imaging experiments. We further show that the over-the-band plasmon dispersion remains robust in the presence of ordering of the narrow-band carriers. The specific examples of a Wigner crystal and a Mott-Hubbard order, worked out in detail, show that interaction-driven gap opening has no impact on the over-the-band plasmon dispersion. Lastly, we consider the implications of the mechanisms behind the over-the-band behavior for achieving of unidirectional collective modes. We present a new mechanism for plasmon nonreciprocity the magnitude of which is controllable through the strength of electron-electron interactions, which makes it particularly pronounced in the moiré materials.

Thesis Supervisor: Leonid S. Levitov
Title: Professor of Physics

Acknowledgments

Much like different types of interactions shape the collective response of a solid, so have the interactions with different people during my time at MIT shaped me as a physicist. I am grateful to everyone who helped me throughout my PhD and so before starting with a discussion of collective properties of an actual solid, I would like to thank everyone whose support made this PhD crystallize.

First and foremost, I would like to thank my advisor Leonid Levitov. I had the privilege to learn from Leonid as his PhD student for the past five years, but also as a summer undergraduate student here in 2014, and as his teaching assistant in Theory of Solids. I am thankful for his time, all our scientific discussions and his thought-provoking questions, the insights and ideas he shared with me, as well as the way and pace he shared them. Leonid has a unique perspective and foresight in physical matters, a great focus on experimental consequences, and an impressively precise style of scientific writing. Working with Leonid has fundamentally enhanced my understanding of physics and the clarity of my scientific writing. It has also strengthened my restraint to jump to conclusions and deepened my appreciation of experimental results. It has made me a more resilient and thorough physicist. Crucially, it has inspired me and taught me how to ask questions thus opening a world of opportunities and over time, in a seamless manner, developed in me the independence required to explore these questions and to discover. I look forward to the journey ahead of me and I hope to research and teach and mentor in a manner worthy of the teaching and guidance I have received from Leonid. Thank you Leonid.

An exciting aspect of my PhD was the opportunity, thanks to Leonid's encouragement, to collaborate with other researchers on both the experimental and theoretical side of the aisle. I would like to thank Joseph Stroscio, Nikolai Zhitenev, Christopher Gutiérrez, Daniel Walkup, and Fereshte Ghahari for sharing their data on graphene quantum dots and for their interest in modelling of the data. The work on graphene quantum dots would not have been possible without the guidance of Joaquin Rodriguez-Nieva, whom I would like to thank for helping me both personally

and professionally during my early years here at MIT. I would also like to thank Eli Zeldov and his student Aviram Uri. Aviram's probing questions about the nature of drift currents and his deep physical intuitions taught me a lot. Working with Andrea Young, Joshua Island and Michael Zaletel was highly educational and a lot of fun - thank you. I am also grateful for the opportunity to have worked with Francisco Guinea on recent projects, which was a great chance for me to be exposed to the inner thinking of a great physicist.

The Condensed Matter Theory (CMT) department was to a large extent my home for the past five years. I am thankful to all CMT professors for the stimulating academic environment. Liang Fu for being on my oral exam committee where his question left me perplexed, the Theory of Solids class, where he shared with us some of his out-of-the-box intuition, and for his insightful questions during seminars. Mehran Kardar for showing me in the first year what a true Statistical Mechanics class is. Patrick Lee for his Theory of Solids class which taught both solids but also physical thinking which was made clear every time with his words, "I pulled a fast one on you". Marin Soljačić for being on my oral exam committee and for inviting me to some of his group meetings. Senthil Todadri for being with me along my academic journey: being my academic advisor and for being a committee member in both my oral exam and thesis defense. The CMT postdocs were my role models and I value all of our discussions. In particular I would like to thank Brian Skinner, Jonathan Ruhman, and Debanjan Chowdhury for all of our conversations and their willingness to discuss my ideas. The CMT graduate students have been the emotional support group that I much needed throughout the PhD. Michał Papaj and Michael DeMarco for their friendship, joint problem set solving, revision for the oral exam and, in later years, academic support on many levels. Ali Fahimniya for his friendship, recent collaborations and reading a draft of this thesis. I would like to thank my past and present fellow group members: Oles Shtanko, Jian Feng Kong, Jun Yong Khoo, Zhiyu Dong, Margarita Davydova, and Olumakinde Ogunnaike for both the fruitful and the not-so-fruitful discussions which were all helpful ultimately. I also value all the interactions with Vladyslav Kozii, Michael Pretko, and Hamed Pakatchi who

shared with me their experience-gained wisdom.

I would also like to thank the graduate students from my cohort as I fondly remember all of the interactions we had, especially during the first year. Working on the problem sets with Reynier Cruz Torres, interacting socially with Sameer Abraham and Kushal Seetharam, discussing the nitty-gritty of condensed matter experiments with Dahlia Klein, and analyzing the intricacies of the US tax system with Constantin Weisser, are cherished memories. I would also like to thank the MIT Polish Society for the supply of pierogis, movie screenings, barbecues and for the occasional much needed break from work.

I was privileged to be a part of the Center for Integrated Quantum Materials. Through it I had the opportunity to interact with many brilliant scientists from different institutions. In particular I would like to thank Amir Yacoby and Philip Kim for sharing their experimental data and for leading the research thrusts I was a member of. The opportunity to listen to any presentation by Joseph Checkelsky, whose enthusiasm for physics is contagious and inspiring, was for me a highlight of any CIQM event and always boosted my morale. I am also thankful to Raymond Ashoori for sharing his pristine experimental data and for being on my thesis committee.

It would be a grave omission not to acknowledge the support of the Academic Programs Office staff. I feel that the physics department and the graduate programme would cease to exist without the guidance and support of Cathy Modica, Sydney Miller, and Lesley Keaney. Their incredible professionalism and organization enable physics graduate students to focus on their research and their thoughtfulness makes us feel welcome and part of the community from the onset. Thank you.

I would also like to thank my family: my mum for her constant encouragement and for providing me with the opportunities I had in life - without her support I would not be where I am today; my grandmother for our weekly calls and for accepting my childhood experiments -breaking the lightbulbs and burning the curtains could have easily marked the end of my scientific explorations had she been less tolerant; and my brother for his moral support and relaxing discussions on all aspects of personal and professional life. Dziękuję.

In acknowledgment of everything I gained: collaborations; knowledge; scientific thinking; memories; friends, in all the different places: lecture theaters; classrooms; offices; physics graduate lounge; libraries; socials; exam halls; on Skype; on Zoom; corridors; the gym; friends' homes; restaurants, I sincerely apologize for any omissions. Thank you to everyone who, in some way or another and to whatever extent, made my PhD such an amazing journey. Thank you.

Cambridge, Massachusetts

May 13, 2020

Contents

List of Figures

Chapter 1

Introduction

1.1 Surface plasmons: collective modes with tunable dispersion

Plasmons are collective excitations in solids in which many electrons move together synchronized by long-range Coulomb interactions [1, 2, 3, 4, 5]. The wide interest in plasmons stems from their hybrid charge-field character, a property that makes these excitations central to the research at the frontier of electronics and photonics [6, 7, 8]. This is a vibrant and, presently, rapidly evolving field which spans a vast variety of topics. This section provides a brief survey of different types of plasmon modes and describes the recent developments triggered by the advent of graphene plasmonics, in particular the broad-band tunability of plasmons in graphene-based nanostructures [9, 10, 11, 12]. In subsequent sections we discuss the new opportunities that are enabled by the recently discovered narrow electron bands in twisted bilayer graphene [13, 14, 15] and related materials [16, 17, 18].

There are several reasons plasmons play a central role in science and technology. One is that these excitations describe the response of charge and current dynamics in conductors to external AC fields. They are therefore essential for our understanding of the coupling between EM radiation and matter, and for designing and controlling it in experiments. The dynamical response of materials described by plasmons explains a

variety of electron-interaction-driven phenomena in condensed matter physics such as the dynamical compressibility, reflectivity of metals, the correlated insulating behavior, the Kohn anomalies, and many others [19, 4, 20]. On a practical side, plasmons underpin a variety of optoelectronics applications including the ones of high current interest [9] such as ultrasensitive optical biosensing [21, 22, 23], photonic metamaterials [24], light harvesting [8, 25], optical nanoantennas [26] and quantum information processing [27, 28, 29, 30].

One aspect of plasmons that sets them apart from other collective modes in solids is that their properties are widely tunable by various knobs [6, 7, 8]. Plasmonic frequencies, which correspond to periodicity of charge and field oscillations in time, span the range from the optical and UV down to the low infrared [19, 20]. Crucially, the spatial wavelength of charge density oscillations comprising the plasmon is not photon-like but is considerably shorter. This is so because the inertia of electron movement in the plasmon excitation is greater than that of the electromagnetic field of photons [31]. The relatively short wavelength values enable the behaviors of interest [9, 10, 12] such as mode squeezing, high nonlinear couplings or anharmonicities. The mode character, its frequency and dispersion $\omega_{\rm p}(\mathbf{q})$ take on different forms for systems of different dimensionality [19] and geometry [31]. This variety is illustrated in Fig. 1-1 and Fig. 1-2, and will be discussed in detail below.

To set the stage for this discussion, we start by reviewing plasmons in a 3D electron gas. The 3D bulk plasmons in isotropic and homogeneous metals are purely longitudinal charge-density waves [19]. The frequency value for these oscillations is set by the plasma frequency

$$\omega_{pl} = \omega_{\rm p}(0) = \sqrt{\frac{4\pi n e^2}{m}}\,, \tag{1.1}$$

which is a measure of electrons' inertia: the higher the effective mass m, the lower is the oscillation frequency; the higher the carrier density n, the stronger is the effective Coulomb energy driving the oscillations. For metallic densities [20] of $n \approx 10^{20}$ cm^{-3} and for approximately bare electron mass m, Eq.(1.1) yields typical values of

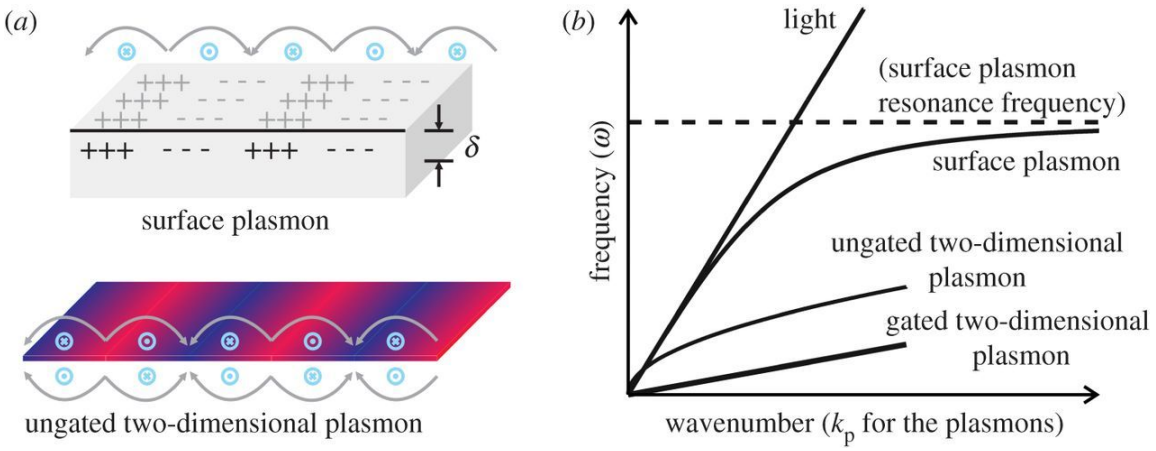

Figure 1-1: (a) Pattern of charge displacements (± signs) on the surface, defined by skin depth δ, of a 3D metal (upper picture) and on the surface of a 2D materials (bottom picture). Gray and blue arrows correspond to the electric field and magnetic fields respectively. (b) Comparison of plasmon dispersions in different systems. Dispersion of plasmons in a two-dimensional system shows a gentler dependence on wavenumber as compared to plasmons at the interface of a 3D metal and a dielectric. Figures in (a) and (b) are reproduced from Ref. [31].

around $\omega_{pl} \approx 4$ eV. This puts bulk 3D metal plasmons in the UV part of the light spectrum allowing for experimental detection of plasma excitations from energy-loss measurements of monoenergetic electron beams, transmitted or reflected by a sample [19].

In 2D materials the frequency of plasmon excitations is similarly set by the charge density and the effective carrier mass. The characteristic plasmon frequency, at momenta on the order of the Fermi wavevector $k_F \approx \sqrt{2\pi n}$, is [32, 33, 34]

$$\omega_{\rm p}(q = k_F) \approx \sqrt{2\pi v_F n e^2}\,, \tag{1.2}$$

where $v_F \approx k_F/m$ is the Fermi velocity and m, as before, is the carrier mass. However unlike in the case of 3D materials, in 2D systems the charge density is, in general, many orders of magnitude lower than that characteristic of metals (on the order of $10^{11} - 10^{12}\ cm^{-2}$) [35]. These low carrier densities together with relatively slow, compared to the speed of light, Fermi velocities give rise to a characteristic frequency

for plasmon oscillations

$$\omega_{\mathrm{p}}(q = k_F) \approx 0.11\sqrt{\frac{n}{10^{12}\ cm^{-2}}}eV\,, \tag{1.3}$$

which can be further reduced by a dielectric constant κ of the encapsulating materials. In the above estimate we used the value $v_F = 10^6$ m/s corresponding to monolayer graphene [36]. In particular for graphene, these energy scales place its plasmons in a regime relevant for studying light-matter coupling in the visible light frequencies or realization of robust and cheap photodetectors of terahertz radiation [11, 37].

2D materials allow for even greater tunability of plasmon properties than the 3D systems [35, 36, 38]. For example, charge density can be reversibly varied in the same sample with an application of a gate potential [39] without a need for chemical doping as done in 3D. This allows to tune the characteristic plasmon frequency Eq.(1.3) by few orders of magnitude. By stacking several 2D materials together or by introducing more gates, a previously metallic system can become an insulator [40] or a system without spin-orbit coupling can develop one [41]. The nature of plasmons can therefore be probed at different regimes: low and high temperatures (compared to chemical potential); low and high frequencies (again compared to chemical potential); insulating, metallic or semi-metallic fillings; and many more. This synergy between tunability of plasmon properties and that of 2D electron systems therefore allows to study the dynamical response of the same electronic system with both greater ease and in greater detail.

While the characteristic frequency of plasmon oscillations is set by charge density, the qualitative behavior of the plasmon dispersion is controlled by the different form a Coulomb interaction takes in different system dimensionalities [19, 20]. Just like the plasmons in 3D, plasmons at the surface of a 2D material are synchronized by the long-range Coulomb interaction. This interaction however, unlike the motion of charges, is not constrained to the plane of the material but rather permeates through whole of the 3D space. This in turn translates into a plasmon mode being gapped in 3D, but gapless in a 2D system, Fig. 1-2a. The corresponding long-wavelength

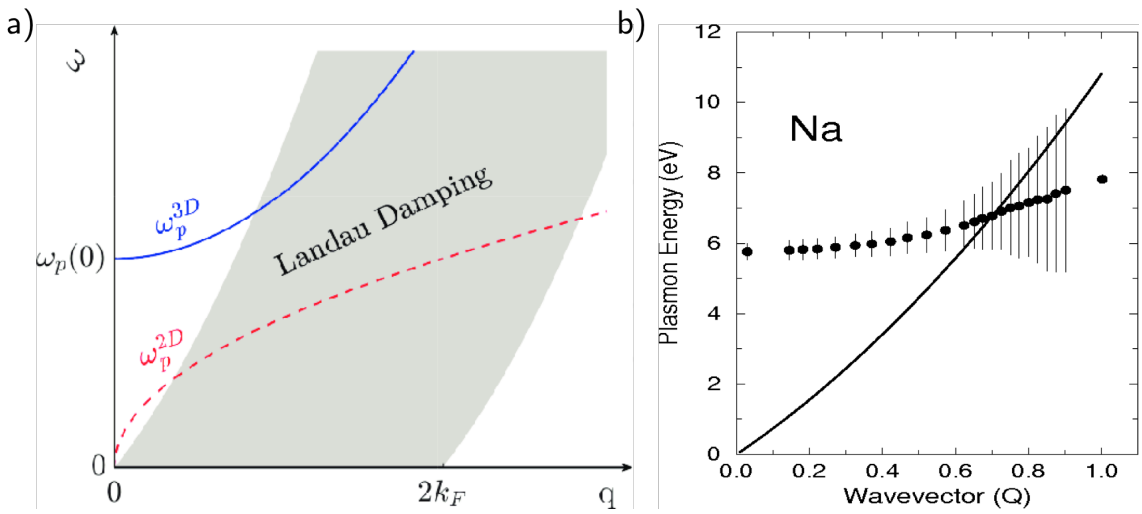

Figure 1-2: (a) Plasmon dispersion in the 2D and 3D systems. A 2D plasmon mode due to a 3D nature of the Coulomb interaction becomes gapless. The shaded region corresponds to the p-h continuum where a plasmon can decay into an electron and a hole (pair-production damping). Taken from Ref. [42]. (b) A plot of an experimentally measured plasmon dispersion in sodium. The error bars correspond to the width of the plasmonic resonance; the straight line indicates the edge of the p-h continuum. Figure is reproduced from Ref. [43].

dispersions are [4, 19, 32, 33, 34]

$$\omega_p^{3D}(q) \approx \omega_{pl}\left(1+\frac{3}{10}\frac{v_F^2 q^2}{\omega_{pl}^2}+\dots\right), \tag{1.4}$$

$$\omega_p^{2D}(q) \approx \omega_0\sqrt{q} \quad \omega_0=\sqrt{2e^2E_F}, \tag{1.5}$$

where, as before, v_F is the Fermi velocity and $E_F = v_F k_F$ is the chemical potential. A typical 2D surface plasmon's dispersion, shown in Fig. 1-1b, exhibits a highly dispersive behavior at a wide range of plasmon wavelengths. This is unlike the 3D behavior, Fig. 1-2a, where the dispersion is relatively weak, $\Delta\omega \sim v_F^2 q^2/\omega_{\rm pl}$, suppressed by the large plasma frequency ω_{pl}, see Eq.(1.4). The strong dependence of the plasmon frequency enables selective excitation of plasmon oscillations of different wavelengths [9, 10, 11, 12].

The 2D materials are essential for high tunability of 2D surface plasmons. This is best seen by comparison with metal surface plasmons [44] that also feature a gapless

dispersion, Fig. 1-1b, characteristic of carriers constrained to a 2D plane. Here the carrier motion is constrained because transverse alternating electric fields can only exist within a thin skin depth of the metal making the system quasi-2D. The resulting pattern of charge displacements, see Fig. 1-1a, for metal surface plasmons is therefore significantly different from the one of 2D surface plasmons. The dispersion of metal surface plasmon modes reflects these different patterns of carrier motion resulting in the characteristic plasmon group velocity being set by the speed of light c. This makes metal surface plasmons much more dispersive than the 2D plasmons where the characteristic plasmon group velocity is set by the Fermi velocity v_F. The range of possible wavelengths, before the dispersion saturates at [19]

$$\omega_s = \frac{\omega_{pl}}{\sqrt{1+\varepsilon_d}}\,, \tag{1.6}$$

is therefore much smaller than the dispersive range of the 2D material plasmons as depicted in Fig. 1-1b. Here ε_d is the static dielectric constant of the dielectric in contact with the metal. The suppression by the dielectric constant allows for the frequency of these plasmons to be similarly reduced at will [8], with the help of sufficiently insulating dielectrics, to bring them into the characteristic frequency scales of the 2D surface plasmons from Eq. (1.3). Unlike the 2D surface plasmons however, the carrier density can not be easily varied. This relative lack of tunability for metal surface plasmons and their strongly dispersive character at small wavelength range set these modes apart from plasmons in 2D materials.

1.2 Plasmon damping mechanisms

For plasmons to exist, oscillating carriers must be able to undergo multiple periods of their motion undisturbed. More precisely, the frequency of electron oscillations $\omega_{\mathrm{p}}(\mathbf{q})$ has to be higher than the frequency of underlying scattering processes to make sure that the electron motion is collisionless on the timescales of charge density oscillations [19, 20]. Provided this condition is met then plasmons should be a well-defined

quasiparticle excitation with a narrow resonance peak. Experimental measurements [31] show that while indeed plasmons are sharply defined at long wavelengths, then as plasmon momentum increases the width of the plasmon resonance broadens, see Fig. 1-2b. This broadening of a quasi-particle resonance indicates a presence of a plasmon damping mechanism.

The frequency-momentum region, shaded area in Fig. 1-2a, where plasmons are rapidly damped is independent of system's dimensionality and persists at zero temperatures as well. These two observations point towards kinematic origins of the damping mechanism. Indeed the damping occurs in the frequency-momentum region where plasmon, which can be understood as a bound electron-hole pair, is permitted to decay into the individual electron and a hole leading to damping via pair production (familiar from particle physics) [2, 19]. The process behind the damping mechanism can be also explained with a wave-surfer analogy wherein the surfer is an electron gaining or losing energy to the plasmon wave depending on whether electron is moving faster or slower than the plasmon wave. With increasing temperature the boundaries of the region where plasmons can become damped by pair-production become broadened. This damping, outside of the otherwise kinematically permitted region, is called the Landau damping (with the pair-production damping sometimes refered to as Zero-T Landau damping) - a famous phenomenon originally predicted [45] and measured [46] in the context of plasma physics.

The necessary frequency-momentum regime for plasmons to be a well-defined oscillation therefore has to avoid the boundaries of the pair-production region. Experimentally this constraint, while allowing for plasmons to be measured and used in practical applications [47, 48, 49, 50], does not eliminate damping. Higher order processes [51, 52, 53], involving scattering with a phonon or impurities, provide missing portion of momentum which brings plasmons into the pair-production damping region. As such it is therefore the presence of the particle-hole (p-h) continuum, in combination with the different scattering processes, which controls the plasmon lifespan. In the following sections we will demonstrate how this limitation can be bypassed in strongly interacting systems by decoupling the frequency scale of plasmon

oscillations from that characteristic of p-h excitations.

1.3 Narrow electron bands in moiré graphene

The experimental discovery of graphene [39] followed by the realization that various 2D materials can be stacked to engineer a wide variety properties of electronic systems [35] made 2D van der Waals heterostructures physics central for theoretical and experimental research. The most recent discovery in this area involves the family of moiré materials (named so for their resemblance of the real-space pattern of atoms and that of moiré patterns in textiles, see Fig. 1-3a), where by placing two (or more) well understood 2D materials on top of each other at various angles, a regime of strongly-interacting physics can be accessed [13, 14, 15]. In the remainder of this section we review recent experimental observations in the field of moiré materials as well as identify the key qualitative features of these electron systems. In the next section we will then discuss how such strongly-interacting systems can be used to provide a "twist" on the properties of the 2D surface plasmons introduced in the previous sections.

The most studied example of the family of moiré materials is the twisted bilayer graphene (TBG) which consists of two monolayer graphenes placed on top of one another. When the two graphene monolayers are rotated to special small angles, referred to as "magic"-angles, their resulting effective electron bandstructure features extremely narrow electron bands [54, 55] (bands 1 and 1' in the Fig. 1-3b). Such a magic angle twisted bilayer graphene (MATBG) has recently emerged as an ideal platform for exploring strongly interacting physics: same sample can display a record-low density superconductivity [14, 15], a Mott insulating regime [13, 56] or even an interaction-driven ferromagnetic behavior [57, 58]. This presence of the flat bands is a unifying feature of the moiré materials, with other systems, such as trilayer graphene [16, 17] or twisted bilayer-bilayer graphene [18, 59], that contain narrow-electron bands similarly exhibiting signatures of strongly interacting physics.

An example phase diagram of magic angle twisted bilayer graphene is shown in

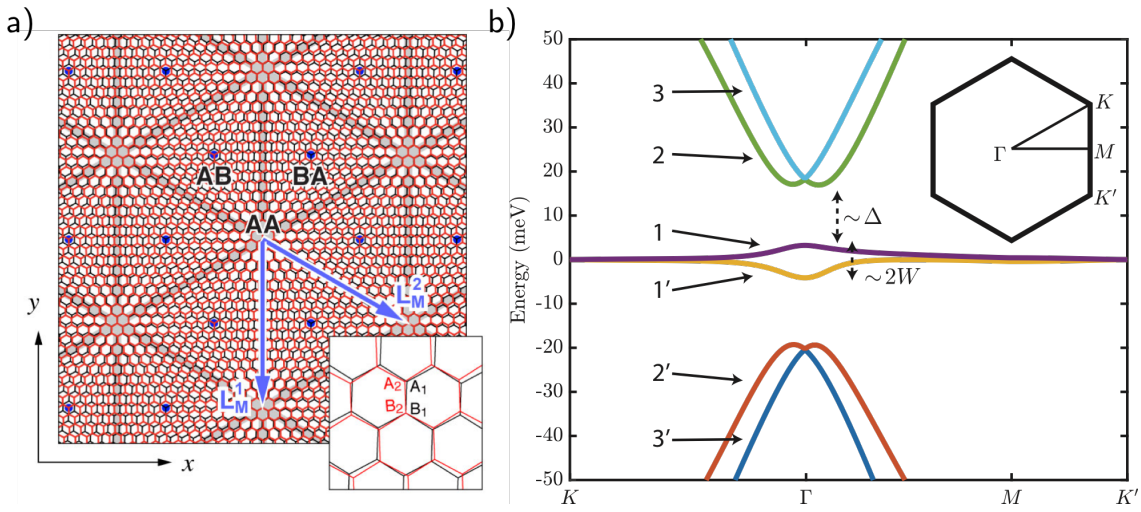

Figure 1-3: (a) Real space pattern of carbon atoms, coming from two graphene sheets rotated with respect to one another, forms an effective moiré lattice. Blue arrows depict the spatial period of the superlattice called the moiré length, L_M. The figure is reproduced from Ref. [60]. (b) A low-energy effective electron bandstructure at a magic angle $\theta = 1.05°$ of a twisted bilayer graphene. The bandstructure features two extremely narrow electron bands (bands 1 and 1') of bandwidth $W \approx 3.75$ meV separated by a large gap $\Delta \approx 14$ meV from the rest of the electronic spectrum. The continuum model [60] used for the calculation is discussed in the Chapter 2.

Fig. 1-4. By varying charge density and filling the two flat bands, see Fig. 1-3b, both a superconducting and an insulating regime can be realized in the same sample. The superconducting state has a record-high critical temperature, for a system of these low carrier densities [14, 61], and the estimated superconducting coupling constant, due to the high density of states present in the flat bands, points towards a strongly coupled superconductor. Twisted bilayer graphene also presents an insulating behavior at fillings where band theory would predict it to be metallic [13]. Both of these observations parallel those made in high-T_C superconductors where the phase-diagram exhibits the same qualitative features [62]. In addition to hosting these two strongly-interacting phenomena, by aligning MATBG with the lattice of the encapsulating material, the MATBG at odd-integer fillings can become also a ferromagnet [57, 58], which origins are attributed to interaction-driven time-reversal symmetry breaking. The simultaneous presence of these examples of a strongly-interacting physics in the same system is behind the recent theoretical and experimental interest in the moiré

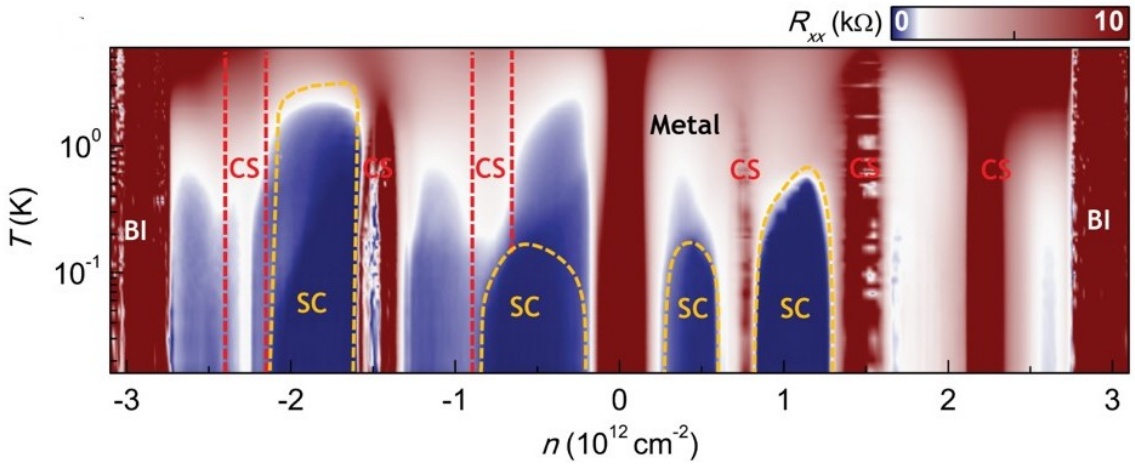

Figure 1-4: A typical temperature-filling phase diagram of a MATBG showing a coexistence of superconducting and correlated regimes in the same sample. Here CS, SC, BI denote correlated state, superconducting state and a band insulator. The figure is reproduced from Ref. [56].

materials.

In order to understand the origins of strong electron-electron interactions in twisted bilayer graphene it is helpful to explain first the geometric origins of the flat electron bands. The effect of twisting two monolayers with respect to one another introduces a spatially slowly varying interlayer hopping [60] with a characteristic superlattice period of $L_M = a/2\sin(\theta/2)$ ($a = 0.246$ nm is the graphene's lattice constant [36]), blue arrows in Fig. 1-3a. For the magic value of $\theta = 1.05°$ the moiré real-space lattice constant is $L_M \approx 13.4$ nm. In momentum space this real-space rotation translates into two graphene Brillioun zones (BZ) rotated by angle θ relative to each other, see Fig. 1-5a. Both BZs are centered at the same Γ point but the K (and K') points of the two layers are separated by a small momentum $4\pi/(3L_M)$. The two K (and K' points) of the two layers give rise to a BZ folding and formation of a Mini-Brillouin Zone (MBZ), depicted in Fig. 1-5a. As a result, the effective bandstructure originates from states of momenta close to those of K (and K') points of the original graphene layers. In vicinity of the K points both graphene monolayers can be approximated through their linear dispersion $\sim v_F k$, thus giving rise to a characteristic energy scale for the MBZ bands of $v_F/L_M \sim 50meV$. A detailed calculation confirms this analysis yielding a bandwidth of $W \approx 3.75$ meV, see Fig. 1-3. We focused here specifically on

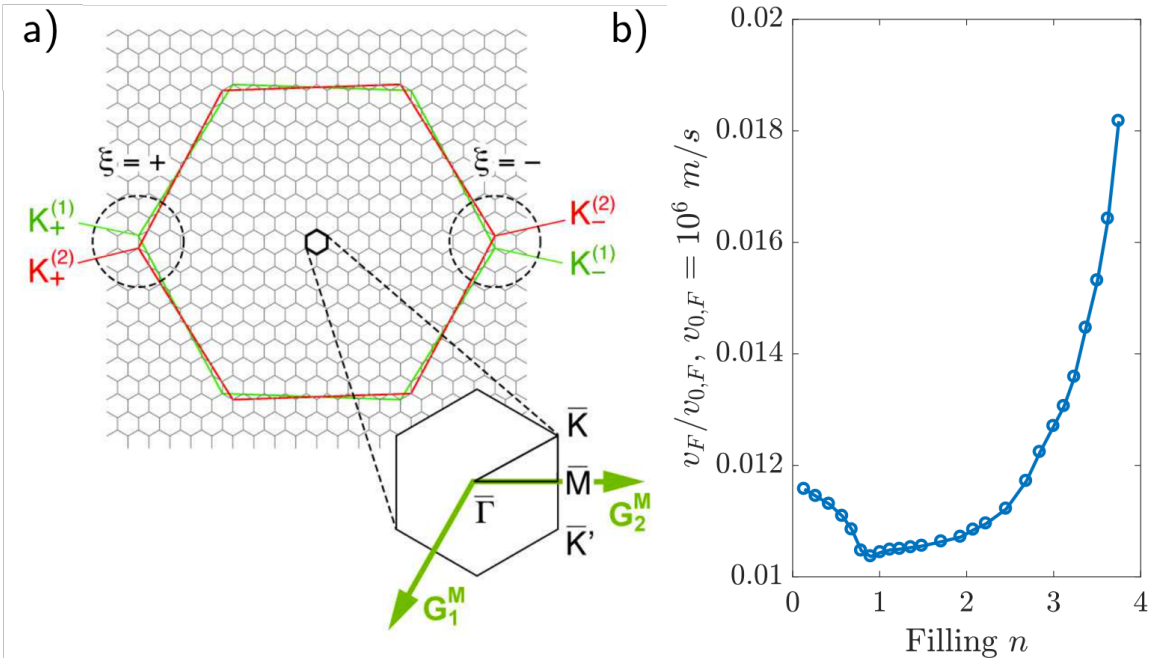

Figure 1-5: (a) Brillouin zone folding in TBG with $\theta = 3.89°$. Two large hexagons represent the first Brillouin zones of graphene layer 1 and 2, and the small hexagon is the mini moiré Brillouin zone of TBG. The Figure is taken from Ref. [60]. (b) Fermi velocity of MATBG at different fillings computed with a realistic bandstructure model discussed in Chapter 2. The Fermi velocity is around two orders of magnitude smaller than the bare graphene velocity, $v_{F,0} = 10^6$ m/s. Here v_F does not vanish at the van Hove singularity of the bandstructure, near filling $n \approx 0.65$, due to a finite mesh resolution.

the case of twisted bilayer graphene, but similar reasoning applies to other moiré flat band materials where the superlattice formation that yields MBZ stems from lattice mismatch, as in the case of trilayer graphene [63, 64], or also small twist angle, as for example in the case of twisted bilayer-bilayer [18].

To quantify the strength of electron-electron interactions in moiré materials it is helpful to compare the characteristic kinetic energy of the carriers to the characteristic Coulomb energy between them. One parameter which quantifies this ratio is the effective fine structure constant

$$\alpha \sim \frac{e^2 k_F}{E_F} = \frac{e^2}{v_F}, \tag{1.7}$$

where we took the typical Coulomb energy as set by Fermi wavelength, $e^2 k_F$, and we

approximated the typical kinetic energy with the Fermi energy E_F. For parabolically dispersing carriers, a more conventional choice would be the r_s parameter [4] which scales with density n and Fermi velocity identically to parameter α defined in Eq.(1.7). The qualitative meaning of the parameter α is clear: the lower is the Fermi energy, which can be reduced either through v_F or carrier density n, the greater the role the Coulomb interaction plays in characterizing carriers behavior.

At the magic twist angle of $\theta \sim 1^\circ$ the effective fine structure constant of TBG exceeds unity, $\alpha{\sim}20-30$. The origins of this enhancement of interactions trace back to the narrow bandstructure which at the magic angle is minimized [54, 55]. This narrow bandwidth in turn translates to low Fermi velocities v_F, $v_F \approx v_{F,\text{graphene}}/100$ as depicted in Fig. 1-5b. For comparison [36, 65], when encapsulated, monolayer graphene has $\alpha{\sim}0.2-0.8$ making MATBG almost a two-orders of magnitudes more strongly coupled system.

1.4 Plasmon modes in moiré graphene

The main claim of the thesis is that the presence of strong electron-electron interactions in narrow-band materials leads to a separation of energy scales between plasmons and p-h excitations. The presence of strong interactions, characterized by the large values of α, pushes the 2D surface plasmon dispersion into the energy gap above the p-h continuum, as demonstrated in Fig. 1-6. In this region plasmons decouple from e-h pair excitations which quenches the damping mechanisms discussed in Sec. 1.2. While the mechanisms behind the over-the-band plasmons are present in all narrow electron bands, the analysis will focus on the MATBG introduced in the previous section as there these over-the-band plasmons can be directly probed.

The new behavior is illustrated in Fig. 1-6, showing plasmon mode for a narrow-band model that mimics the key features of the TBG band. Mode dispersion (red line) is conventional at energies less than the bandwidth, $\omega \lesssim W$, c.f. Fig. 1-2. At lowest energies, plasmon mode is positioned outside the p-h continuum; this suppresses the pair-production damping introduced in Sec. 1.2, but does not protect the mode from

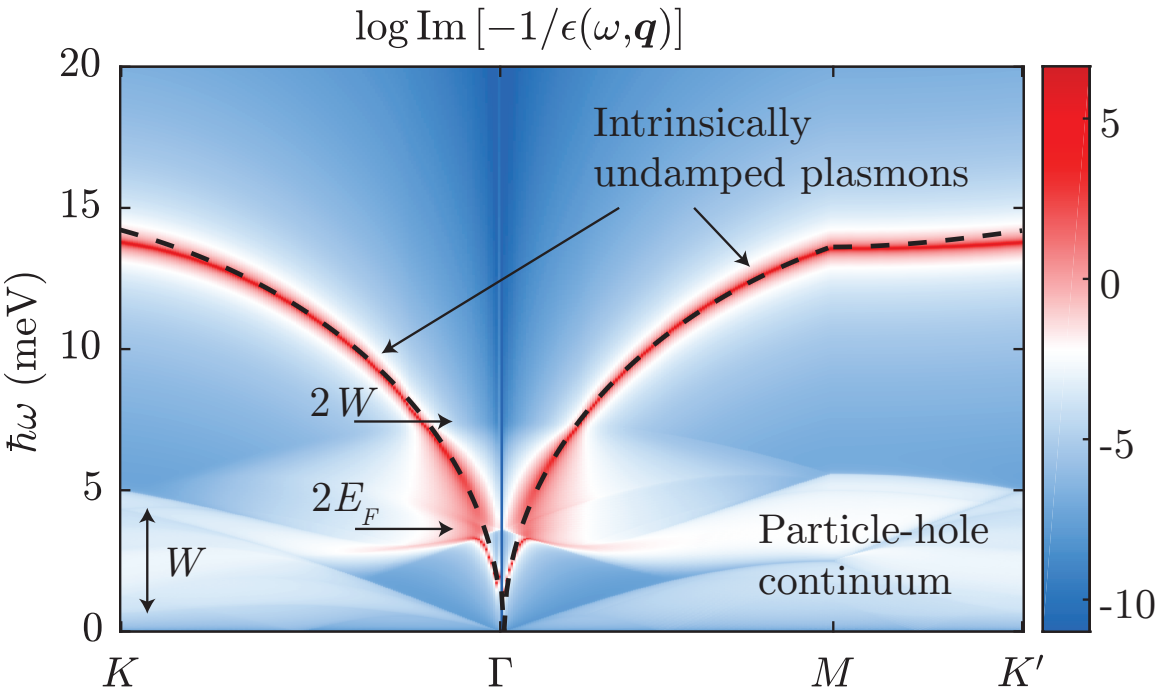

Figure 1-6: Electron loss function $\mathrm{Im}\,(-1/\varepsilon(\omega, \mathbf{q}))$ for a narrow-band toy model (the hexagonal tight-binding model, introduced in Chapter 2). Parameter values are chosen to mimic TBG bands (bandwidth $W = 3.75$ meV, lattice periodicity $L_M = 13.4$ nm, Fermi energy in the conduction band at $E_F \approx 1.81$ meV); log scale is used to clarify the relation between different features. Arrows mark the interband p-h continuum edges. Plasmon dispersion (red line) is fitted with $\omega_{\mathrm{p}}(q) = \sqrt{\beta_q q}$, see Appendix of Chapter 2, (dashed line).

decaying into p-h excitations through disorder scattering or from the conventional $T > 0$ Landau damping [10, 33, 34, 66, 67, 68, 69]. At higher energies, $\omega \sim 2E_F$ (marked by arrow in Fig. 1-6), the mode plunges into p-h continuum and is Landau-damped at $2E_F \lesssim \omega \lesssim 2W$ even at $T = 0$. However, a dramatic change occurs once the mode rises above the p-h continuum. In the forbidden energy gap region, $\omega > 2W$, it becomes *damping-free,* since at these energies there are no free e-h pairs into which plasmon could decay.

As we will see in Chapter 2, mode dispersion has a square-root form characteristic of two-dimensional plasmons [32, 70] from Eq.(1.5). This expression, however, is valid not just at low energies $0 < \omega \lesssim W$ but also at higher energies, $\omega \gg W$, where the mode is undamped. While the dispersion is of the conventional 2D plasmon form, we emphasize that here it takes on a new role, as it describes the plasmon mode at frequencies much higher than the carrier bandwidth, extending to

$$\omega_{\rm p} \sim \sqrt{\alpha} W \gg W, \quad \alpha \sim 20 - 30, \tag{1.8}$$

where the high α values correspond to flat bands in magic-angle moiré graphene as discussed in the previous section. Unlike the conventional plasmons, the square root dispersion Eq.(1.5) is not limited to longest wavelengths. Indeed, as illustrated Fig. 1-6, it extends to wavenumbers which are on the order of the superlattice Brillouin zone width.

We note parenthetically that a number of subtle features of plasmon dispersion pictured in Fig. 1-6 appear to be at odds with the general principles of band theory. For example, every high symmetry point of the Brillouin zone must be a extremum point of band dispersion, namely a local maximum, a local minimum or a saddle point. This would imply that the group velocity $\mathbf{v_g} = \nabla_{\mathbf{q}} \omega_{\rm p}(\mathbf{q})$ vanishes at all high symmetry points (with the exception of the Γ point where the dispersion $\omega_{\rm p}(\mathbf{q})$ has a square root singularity associated with the long-wavelength plasmon oscillations). Somewhat disconcertingly, the group velocity for the dispersion shown in Fig. 1-6 is small but nonzero at the points M and K. This unphysical behavior is an

artefact of the numerical procedure used in our simulation. To obtain the plasmon dispersion that does not suffer from this problem, a method that accounts for the Umklapp scattering processes can be used, similar to the approach in Refs. [71, 72, 73, 74]. The resulting dispersion relation obtained after these adjustments retains the qualitative characteristics discussed above, such as the $\omega_{\rm p}(\mathbf{q}) \propto \sqrt{q}$ dispersion at long wavelengths and the over-the-band character, and flattens out at the high symmetry points as required by the band theory.

Here we briefly discuss the existing literature. Recent work [75] analyzed inter-band plasmon excitations in TBG, which are dominated by polarization of the bands above the flat band and are distinct from the flat-band plasmons analyzed here. Previous experiments [76] reported observation of plasmons in TBG, however their appeal for constructing undamped over-the-band collective modes remained unnoticed in graphene literature. Also, plasmons in narrow bands were analyzed in the context of high-T_c superconductivity [77], finding that plasmon mode can rise above the flat band. However, in cuprates, unlike moiré graphene, the narrow band is not separated from higher bands by a forbidden energy gap, and thus the mode studied in Ref. [77] will plunge into a higher band before acquiring an undamped character. Our prediction of the undamped over-the-band plasmons in TBG and their potential subsequent observation therefore constitute an uncharted territory.

In addition to predicting a large separation of energy scales for plasmons and particle-hole excitations and the quenching of Landau damping, we explore the robustness of this behavior to the ordering in narrow bands. We approach the problem of describing dynamical response of a narrow-band system from two extreme limits:

- Free fermions coupled by long-range Coulomb forces: diagrammatic perturbation theory and the Random Phase Approximation.

- Strongly interacting regime: electrons form an ordered crystal state; collective charge oscillations can be described as "phonon modes".

The details of the diagrammatic perturbation theory approach are presented in Ch.2, while the opposite limit is discussed in the Ch.3. The remaining sections of the intro-

duction summarize results of both approaches and discuss experimental consequences.

1.4.1 The RPA approach

In order to determine properties of plasmons, such as damping or dispersion relation, in a systematic way it is helpful to study the dynamical dielectric function $\varepsilon(\omega, \mathbf{q})$. An applied electric field inside a material becomes screened by the dielectric function $\varepsilon(\omega, \mathbf{q})$ with different limits of ω, $\mathbf{q}$ corresponding to different physical regimes [19, 20]. The limit of $\omega \to 0$ corresponds to static screening, also called the Thomas-Fermi screening, where dielectric function is real, while the limit of $q \to 0$ describes the optical absorption. If in the optical limit the dielectric function becomes imaginary, that indicates that light can be absorbed to excite electron-hole pairs. The knowledge of the dynamical dielectric function is therefore necessary to understand electronic properties of solids as argued in Sec. 1.1.

Plasmons correspond to charge density oscillations which arise in response to a driving external AC electric field. To establish a collective response inside a material the Coulomb interaction needs to be long-range, i.e. not screened, as the motion of charges has to be synchronized. This constrains the real part of the dielectric function to vanish. As hinted above, imaginary part of the dielectric function is related to energy loses and damping due to electron-hole pair production or other decay mechanisms. For the density oscillations not to become damped it is also necessary for the imaginary part of the dielectric function to vanish as well. Therefore plasmon dispersion corresponds to the the nodes of the dielectric function [4, 19]

$$\varepsilon(\omega_{\mathrm{p}}(\mathbf{q}), \mathbf{q}) = 0\,, \tag{1.9}$$

with the imaginary part of the dispersion, if exists, indicating damping.

The task of determining plasmon dispersion therefore reduces to finding the dynamical dielectric function. It is defined as [4]

$$\varepsilon(\omega, \mathbf{q}) = 1 - V_{\mathbf{q}}\Pi(\omega, \mathbf{q})\,, \tag{1.10}$$

where $V_{\mathbf{q}}$ is electron-electron interaction and $\Pi(\omega, \mathbf{q})$ is an object called polarization function (see below). Here the Coulomb interaction is given by 2D Fourier transform of the 3D $1/r$ potential, which yields

$$V_{\mathbf{q}} = \frac{2\pi e^2}{\kappa q} \,. \tag{1.11}$$

The parameter κ quantifies the amount of static dielectric screening of the surrounding material. Note that as compared to a 3D Fourier transform of a Coulomb interaction which goes as $\propto 1/q^2$ here the additional constrain of charges to a 2D plane results in much slower decay of the interaction with momentum q. This different momentum dependence of a Coulomb interaction in 3D and 2D was discussed in the Sec. 1.1 as the explanation for the qualitatively different dispersion of plasmons in 3D and 2D.

The function $\Pi(\omega, \mathbf{q})$ is the polarization function of an electronic system, which quantifies strength of electron density-density correlations. To compute it exactly it is necessary to solve a fully interacting electron problem. Under the assumptions that density-density correlations are small, i.e. electrons are free particles that are weakly perturbed by the Coulomb interaction, the polarization function can estimated with the Random Phase Approximation (RPA) [4]

$$\Pi(\omega, \mathbf{q}) = \sum_{\mathbf{k},s,s'} \frac{(f_{s,\mathbf{k}+\mathbf{q}} - f_{s',\mathbf{k}}) F^{ss'}_{\mathbf{k}+\mathbf{q},\mathbf{k}}}{E_{s,\mathbf{k}+\mathbf{q}} - E_{s',\mathbf{k}} - \omega - i0} \,. \tag{1.12}$$

This form, which follows directly from the linear response theory for free electrons [19], can be justified by a diagrammatic approach known as the "large-N" expansion [4]. Here the sum $\mathbf{k}$ ranges over the crystal momenta, s, s' are band indices, $f_{s,\mathbf{k}}$ is the Fermi-Dirac distribution for a dispersion $E_{s,\mathbf{k}}$, and $F^{ss'}_{\mathbf{k}+\mathbf{q},\mathbf{k}}$ is the overlap of Bloch wavefunctions (see Chapter 2).

To determine the dispersion of over-the-band modes we focus on the frequency regime $\omega \gg W$ of the polarization function Eq.(1.12). A detailed analysis of all frequency limits of the above expression Eq.(1.12) is presented in the Chapter 2. For now let us assume that there are no higher bands in the system and that the

momentum q is smaller than the Fermi wavelength k_F. Under these assumptions polarization function has to have an asymptotic form [51, 78]

$$\Pi(\omega, \mathbf{q}) \approx \frac{2}{\pi} W \frac{q^2}{\omega^2}\,, \tag{1.13}$$

where W, the characteristic scale of p-h excitations, is set by the system's bandwidth. In contrast, in the frequency regime $\omega \ll E_F$ the characteristic scale of p-h excitation would be set by the chemical potential E_F and give

$$\Pi(\omega, \mathbf{q}) \approx \frac{n}{m}\frac{q^2}{\omega^2} \approx \frac{2}{\pi} E_F \frac{q^2}{\omega^2}\,, \tag{1.14}$$

which is the well known classical "acceleration" result [4]. Returning to the limit of $\omega \gg W$, we find that the corresponding plasmon dispersion is then

$$\omega_{\mathrm{p}}(\mathbf{q}) \approx \sqrt{4\alpha W v_F q} \quad \text{for } q < k_F,\, \omega > E_F\,. \tag{1.15}$$

Note that as required this has the same form as the 2D surface plasmon dispersion discussed in Sec. 1.1 in Eq.(1.5), but with a characteristic energy scale set by the bandwidth W. By analizing the asymptotic large-q form of the Eq.(1.12), we can show that for q on the order of the reciprocal lattice spacing, the dispersion saturates at an energy scale $\omega_{\mathrm{p}} \approx \sqrt{\alpha} W$. Since $\alpha \gg 1$ this dictates a plasmon dispersion extending far above the p-h continuum as shown in Fig. 1-6. This is the new behavior present only in strongly interacting systems.

1.4.2 A realistic TBG model

Although the origins of the over-the-band plasmon behavior can be understood simply through the kinematic arguments presented above, it is necessary to verify that the same conclusions are reached using a realistic model of TBG's bandstructure. We extended therefore the polarization function analysis to a continuum model of TBG [60], the bandstructure of which is shown in Fig. 1-3. We find that indeed plasmon dispersion extends above the p-h continuum exhibiting the over-the-band behavior,

see Fig. 1-7. The conventionally dispersing part of the plasmon, $\omega < E_F$, is too small to be seen given the narrow-bandstructure and the low chemical potential (here $E_F = 0.289$ meV for half-filling).

The form of the TBG plasmon dispersion (red bright feature) however does not agree with the analysis of the previous section. Specifically the formula $\omega_{\rm p} \approx \sqrt{\alpha}W$ overestimates the saturation frequency as indicated by the predicted dispersion from Eq.(1.15) shown as a dashed line in Fig. 1-7. At high momenta, unlike the predicted from of Eq.(1.15), the dispersion does not continue to rise but rather starts to decrease. The origins of this behavior are explained if more bands are included in the calculation as discussed in Chapter 2. The contribution of interband transitions to the non-flat bands (bands $2, 2', \ldots$ from Fig. 1-3) pushes the dashed dispersion, which comes from intraband transitions only, down in energy. The scale for the plasmon frequency, provided that α is large enough to ensure that modes go over-the-band continuum, therefore turns out to be set by the geometric mean of the bandwidth W and the bandgap Δ, $\omega_{\rm p} \sim \sqrt{\Delta W} \approx 7$ meV, as these are the two energy scales that control the interband transitions to higher bands.

1.4.3 Suppression of the Landau dissipation

From the knowledge of the dielectric function, in addition to the plasmon dispersion, it is also possible to extract information about the lifetime of the collective excitation. A quantity which naturally depicts both, the dispersion relation and the plasmon spectral width, is the electron loss function

$$EELS(\omega, \mathbf{q}) = \mathrm{Im}\left(\frac{-1}{\varepsilon(\omega, \mathbf{q})}\right) = \frac{\mathrm{Im}\,\varepsilon(\omega, \mathbf{q})}{\mathrm{Re}^{\,2}\varepsilon(\omega, \mathbf{q}) + \mathrm{Im}^{\,2}\varepsilon(\omega, \mathbf{q})}\,. \tag{1.16}$$

In the vicinity of $\varepsilon(\omega, \mathbf{q}) = 0$, EELS is a Lorentzian peaked at the plasmon frequency $\omega_{\rm p}(\mathbf{q})$ of width $\mathrm{Im}\,\varepsilon(\omega, \mathbf{q})$. Away from the plasmon dispersion, EELS also gives information about the optical absorption as in the p-h continuum imaginary part of the dielectric function becomes non-zero.

To verify that damping for plasmons above the p-h continuum is indeed quenched,

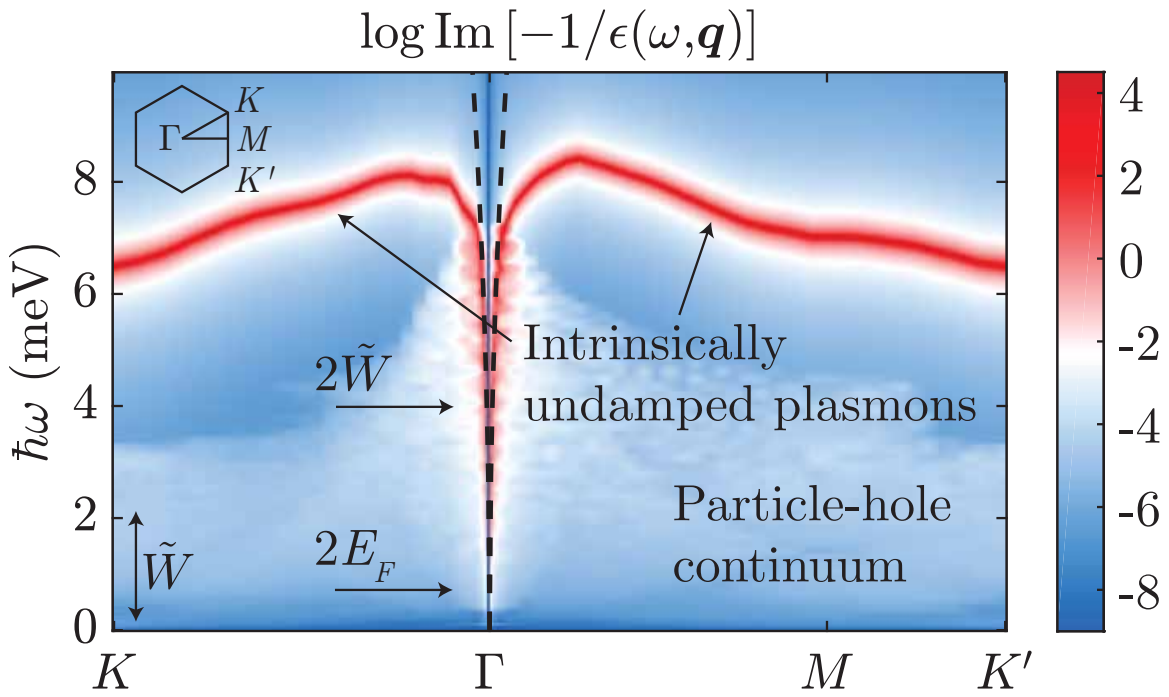

Figure 1-7: Electron loss function $\mathrm{Im}\,(-1/\varepsilon(\omega,\mathbf{q}))$ for TBG bandstructure. The Fermi energy value $E_F = 0.289$meV corresponds to electron band half-filling; and set the average background dielectric constant is $\kappa = 3.03$ (typical of an air/TBG/hBN heterostructure). Log scale is used to clarify the relation between different features. Arrows mark the approximate interband p-h continuum edges, obtained for the effective bandwidth $\tilde{W} \approx 2$ meV (see text). Plasmon dispersion (red line) at small q is fitted with $\omega_{\mathrm{p}}(q) = \sqrt{\beta_q q}$ (dashed line), demonstrating a significant deviation from the typical 2D plasmon dispersion at large q. In the calculation we used both flat-bands and the next conduction/valence non-flat bands, and verified that higher bands do not alter the quantitative and qualitative behavior.

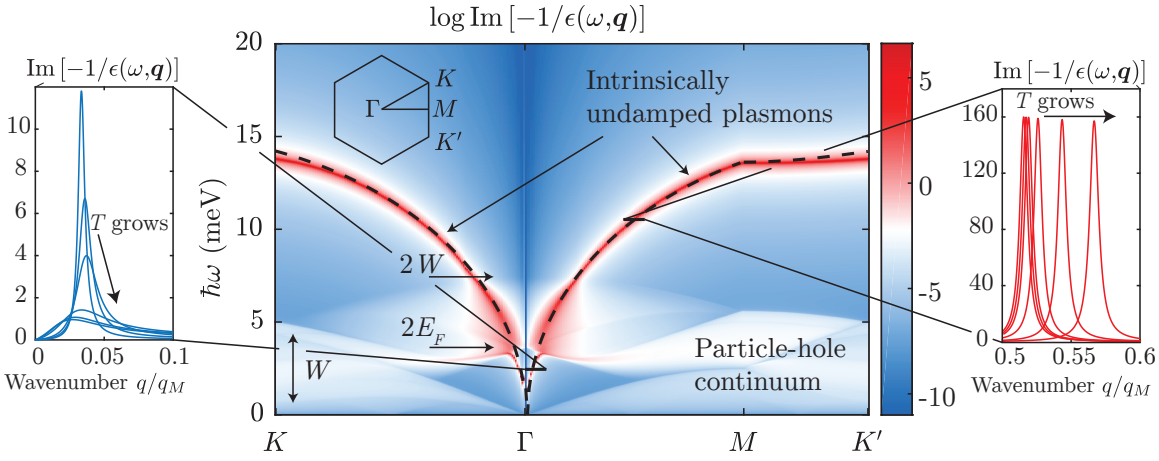

Figure 1-8: Plasmon resonance width as a function of temperature for the over-the-band (right) and conventional (left) plasmons. We see that increasing temperature broadens the resonance of conventional plasmons, but the resonance of the over-the-band plasmons remains fixed at its intrinsic value. In the plot the temperature is varied until $T = E_F$.

we consider how does the plasmonic resonance vary with increasing temperature. To that end we evaluate the polarization function from Eq.(1.12) at various temperatures and plot the corresponding loss function. We find that for plasmons above the continuum the resonance does not broaden with temperature, (see Fig. 1-8), beyond what is set by the intrinsic damping (the zero temperature broadening). For conventional plasmons, their dispersion broadens with increasing temperature as expected by the Landau damping mechanism. We note that this behavior persists up to temperatures comparable with the plasma frequency. Until these high temperatures, the only role rising temperature has on the over-the-band plasmons is to bring the plasmon resonance down in frequency as visible in the right figure of Fig. 1-8.

1.4.4 Experimental signatures

Decoupling of the plasmon mode from the spectrum of p-h excitations gives rise to a direct experimental signature: enhanced spatial coherence of plasmon waves. When decoupled from the p-h continuum, a decay of plasmons through scattering with impurities is inhibited as a p-h pair production is suppressed. This implies that plasmon wave propagating through a narrow-band materials will maintain its

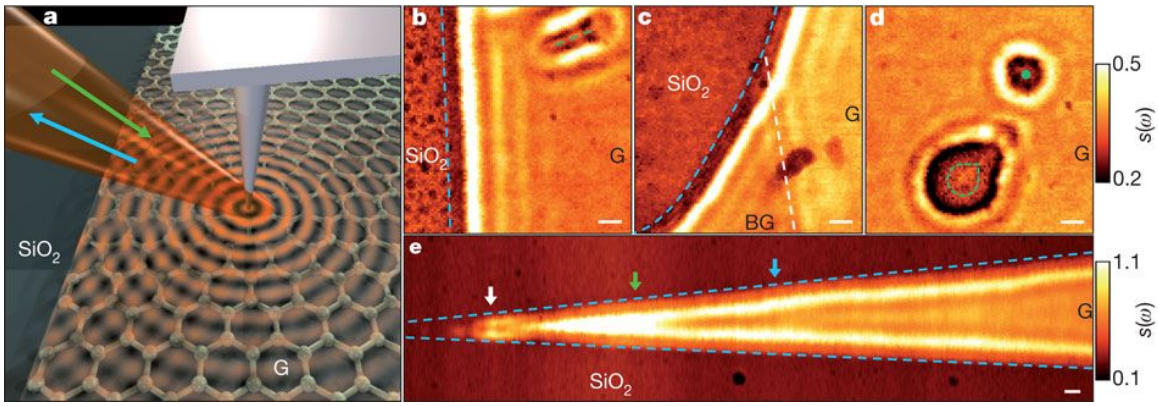

Figure 1-9: (a) An experimental setup of a near-field optical microscopy measurement taken from Ref. [49]. The green and blue arrows indicate the incoming and reflected light. The red circles under the tip illustrate the launched plasmon waves. (b)-(e) Measured SNOM signal amplitudes close to graphene edges (blue dashed lines) and defects (green dashed lines and green dot), and at the boundary between single (G) and bilayer (BG) graphene (white dashed line). See Ref. [49] for a detailed discussion of all the features seen in the measurements.

coherence as it scatters off impurities since the number of plasmons remains the same. In particular, this process will lead to speckle-patterns in near-field microscopy measurements - a smoking gun signature which we now discuss.

A scanning near-field optical microscopy [49, 50] (SNOM) is a measurement in which a plasmon is excited and detected by a metallic tip, see a schematic in Fig. 1-9a. In a SNOM experiment, electromagnetic wave propagates down the metallic tip which resides just above sample's surface. The EM wave in the tip excites a plasmon which then propagates away until it encounters defects or boundaries, from which it gets reflected and part of its wavefront travels back to the tip. The plasmon signal is then picked up and interferes with the signal inside the tip either constructively or destructively depending on the optical path travelled. Due to this strong optical path sensitivity, moving the tip slightly therefore allows for the plasmon wavelength to be accurately measured.

Unlike conventional plasmons which become rapidly damped away from reflecting objects, Fig. 1-9b-e, the over-the-band modes maintain phase coherence in scattering with impurities or other defects. The plasmon wave therefore maintains its phase, just like a laser reflecting from grained surface, leading to a speckle pattern measurable by

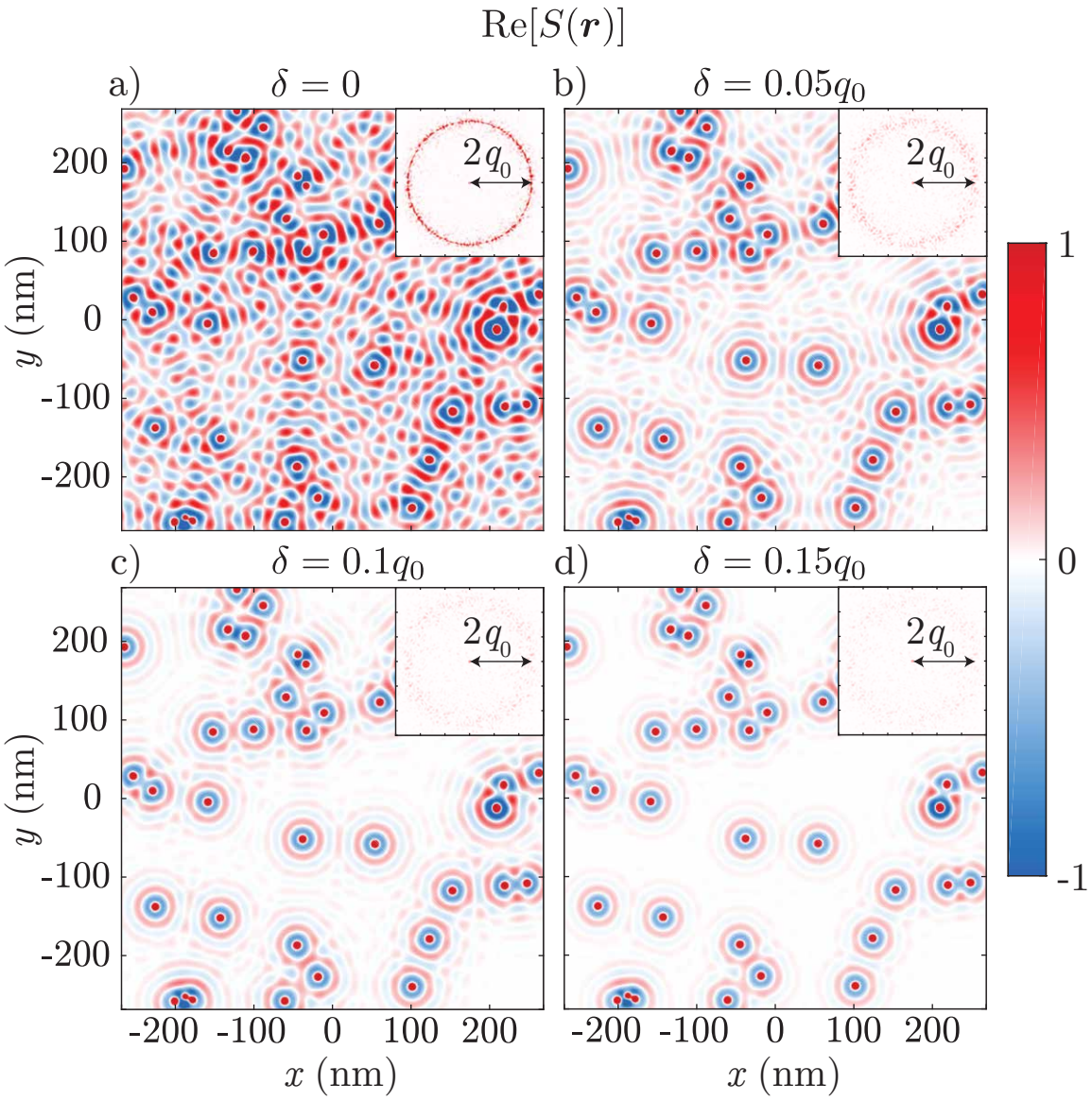

Figure 1-10: (a,b,c,d) Speckle patterns arising due to optical coherence of undamped plasmons in scanning near-field microscopy signal $S(\mathbf{r})$, introduced in Chapter 2, at various ratios of the incoherent to coherent damping δ/q_0. The insets show the corresponding square of the speckle pattern's Fourier transform amplitude $|S_{\mathbf{k}}|^2$. In all panels, for clarity of comparison, we set the plasmon momentum as $q_0 = q_M/2 \approx 0.14$ nm^{-1} and vary only the ratio δ/q_0. The disorder is taken as 40 randomly placed delta functions.

a SNOM tip, Fig. 1-10a. In particular, the smoking-gun signature is present in the Fourier transform of the signal which, if phase coherence is maintained, will show a sharp resonance at double the plasmon wavelength (here the factor of two arises from the forth and back optical path travelled by the plasmon). As amount of incoherent

damping enters into the system, for example via phonons, the sharpness of the speckle pattern and the resonance decreases Fig. 1-10b-d.

1.4.5 Plasmon modes in a Wigner crystal

The opposite limit to the RPA analysis is to start from the assumption that interactions dominate and treat the kinetic motion of electrons as a perturbation. In the absence of kinetic energy, electrons want to minimize their potential energy and thus arrange themselves in a lattice. Such an electron crystal is called a Wigner solid [79], due to its similarity with crystals, and is depicted in Fig. 1-11a. It has been experimentally observed in several systems [80, 81, 82] and postulated [83] to exist in MATBG as well.

To determine dispersion of plasmons in this strongly interacting regime, we need to find the collective modes of electron lattice oscillations. The Wigner solid can be modelled under the same assumptions under which properties of crystals are understood, i.e. the atoms comprising the lattice are rigidly fixed in their positions. Collective oscillations of a crystal lattice are phonons, the dispersion of which can be obtained from classical physics. We apply then the same reasoning to a Wigner crystal and assume that electrons oscillate about their equilibrium positions. The task of determining plasmons of this electron solid therefore reduces to finding the dispersion of phonons of this electronic "crystal" [84, 85, 86, 87].

For a plasmon-like collective motion of "atoms" of the Wigner crystal to arise there has to be a long-range interaction which synchronizes their motion [84]. Microscopically this interaction would be a Coulomb potential, but the task of determining its precise form starting from the $1/r$ form is complicated. We resort therefore to a simple model, which captures the nature of the interaction. We model the Wigner crystal as oscillators arranged in a 2D lattice with period a. Here the lengthscale $a \sim 1/\sqrt{n}$ is set by the charge density n (reminiscent of the Wigner-Seitz radius r_s). At equilibrium, the potential energy of the system is minimized, thus the interaction vanishes and the system is charge neutral. A displacement of an oscillator from equilibrium corresponds to an electron-hole pair dipole forming in real space. Such

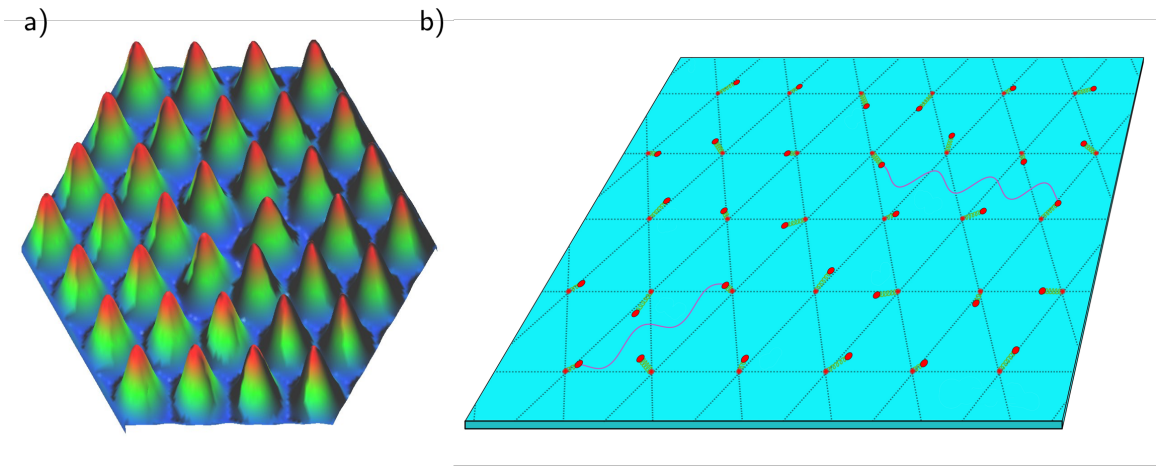

Figure 1-11: (a) An electron density of a Wigner lattice obtained from Monte-Carlo simulations. Source: Cambridge QMC group. (b) Schematic depiction of a Wigner crystal where displacements of electrons from their equilibrium positions can be thought of as giving rise to a dipole moment (green springs). These dipole moments interact (red lines) with one another through a long-range Coulomb interaction driving a synchronization that gives rise to the collective modes. Figure taken from [88].

a dipole can then interact with other dipoles, c.f. Fig. 1-11b, through a long range dipole-dipole interaction. This interaction will drive then the synchronization that gives rise to the collective motion.

With these simplifications in place, we can write the toy-model of the Wigner crystal. The Hamiltonian of the problem is then simply given by

$$H = \sum_{\mathbf{r}} \frac{\mathbf{p}_{\mathbf{r}}^2}{2m} + \frac{m\omega_0^2}{2}\mathbf{q}_{\mathbf{r}}^2 + \frac{1}{2}\sum_{\mathbf{r},\mathbf{r}'} W_{ij}(\mathbf{r}-\mathbf{r}')q_{\mathbf{r},i}q_{\mathbf{r}',j}\,, \tag{1.17}$$

where the $p_{\mathbf{r}}$ and $\mathbf{q}_{\mathbf{r}}$ are the momenta and the displacement positions of the oscillators. Here $W_{ij}(\mathbf{r}-\mathbf{r}') = \frac{\partial^2}{\partial r_i \partial r'_j}\frac{e^2}{|\mathbf{r}-\mathbf{r}'|}$ is the long-range dipole interaction. We note that we assumed all oscillators to have the same mass m and oscillation frequency ω_0. The latter assumption, known in the context of solid state physics as the Einstein phonon model, here is introduced for simplicity as we are seeking modes which dispersion will extend above the single-particle oscillation frequency ω_0 as seen in the RPA analysis.

This Wigner crystal defined through Eq.(1.17) admits two collective modes: one longitudinal, stiff, and one transverse, soft. The long-wavelength dispersion of these

two modes is

$$\omega_{1,\mathbf{k}} \approx \omega_0\sqrt{1+\tilde{\alpha}ka}, \quad \omega_{2,\mathbf{k}} \approx \omega_0, \quad ka \ll 1\,.$$

In the above equations we introduced a dimensionless coupling, a ratio of potential to kinetic energy of the Hamiltonian Eq. (1.17), in analogy to the fine structure constant in the RPA analysis:

$$\tilde{\alpha} = \frac{2\pi e^2}{m\omega_0^2 a^3}$$

Dispersions of both modes are shown in Fig. 1-12. We see that the longitudinal mode corresponds to the over-the-band plasmon dispersion, similarly scaling like $\propto \sqrt{\tilde{\alpha}}$, while the soft mode mimicks the p-h continuum. The Einstein approximation makes both modes gapped and causes the soft-mode to be centered near the p-h excitation frequency ω_0.

To gather further insight into the origins of the over-the-band behavior we consider the pattern of the underlying oscillations that give rise to the two modes of Fig. 1-12. The weakly dispersing mode forms a narrow band. Physically, it describes transverse oscillations in which displacements of different oscillators are nearly perpendicular to the wavevector $\mathbf{k}$ (at $ka \ll 1$). In this band, displacements of different oscillators are weakly coupled by the long-range dipole forces, which thus explains its weak dispersion with energy set only by the oscillation frequency of individual harmonic oscillators. In contrast, the stiff band describes longitudinal oscillations in which displacements of different oscillators are parallel to the wavevector $\mathbf{k}$ (at $ka \ll 1$). This drives a strong coupling between the dipole moments leading to its strong dispersive character.

The analogy between the effective Wigner crystal parameter $\tilde{\alpha}$ and the effective fine structure constant of TBG graphene α can be made more concrete. We can construct an effective Fermi velocity v_F and through it define the "Fermi energy" for this model:

$$v_F \approx \omega_0 a\,, \quad E_F \approx \frac{1}{2}mv_F^2\,. \tag{1.18}$$

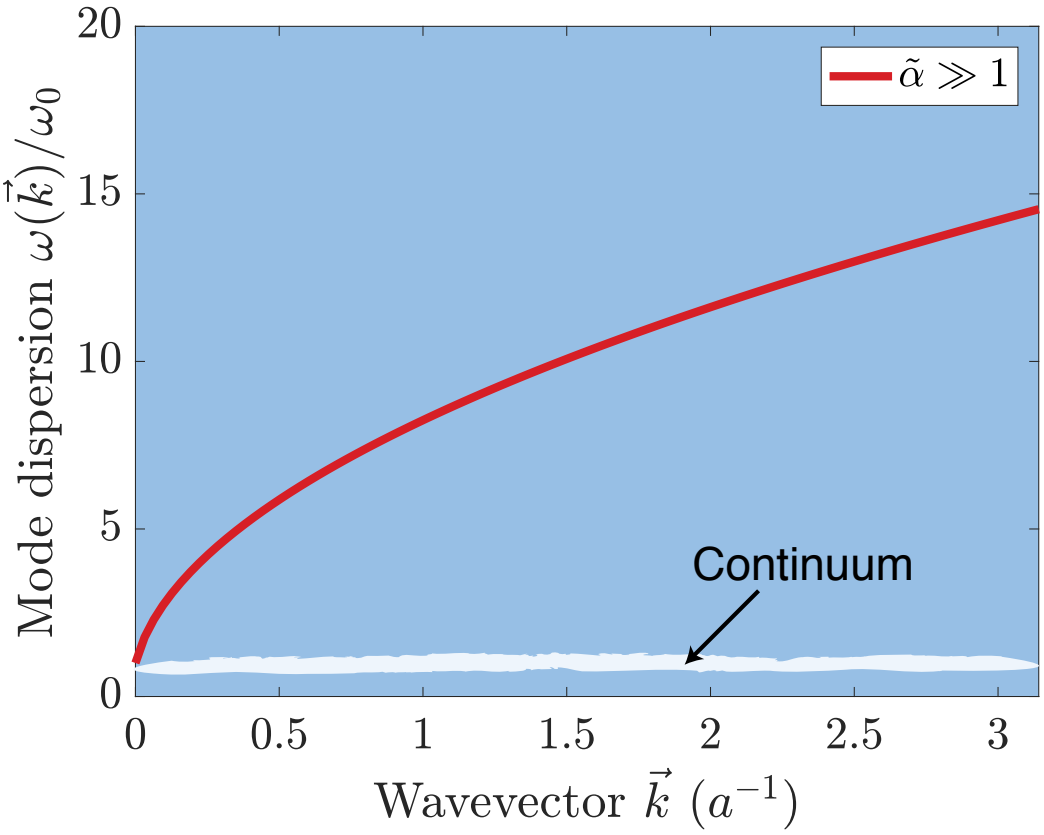

Figure 1-12: Wigner crystal exhibits two collective modes: a longitudinal one, stiff, corresponding to the over-the-band modes (red); a transverse one, soft, mimicking the p-h continuum (white). While the energy scale for the over-the-band mode in a Wigner solid is set by the p-h excitation energy scale ω_0, as in the case of the RPA analysis, strong interactions give rise to a parametric enhancement of their frequency by a factor $\tilde{\alpha} \gg 1$.

Since the narrow-band system Fermi momentum k_F is on the order of the reciprocal lattice spacing $k_F \approx \pi/a$, it shows that in fact $\tilde{\alpha}$ and the effective fine structure constant α are the same two quantities.

Both the collective modes of the Wigner solid, Fig. 1-12c, and the plasmons of the narrow-electron band system obtained through a free-particle approximation, Fig. 1-6, manifest the over-the-band behavior. This surprising conclusion that a method targeted at a weakly interacting system agrees with results of, essentially, a non-perturbative analysis of a strongly interacting model can be ultimately traced back to the microscopic origins of the over-the-band behavior: strongly coupled electron-hole pairs. In the context of the MATBG RPA analysis these can be identified as interband transitions while in the Wigner solid case they correspond to longitudinal oscillations of electrons that form an electric dipole. In both cases the system can be described as a lattice of harmonic oscillators and, therefore, the RPA approximation, that in its roots relies on a harmonic description of collective electron oscillations [3, 89, 2], agrees with the harmonic analysis of a Wigner solid from Eq.(1.17) which explains the robustness of the over-the-band behavior.

1.5 Some implications of over-the-band plasmons

The over-the-band modes in narrow-band materials exist only because of strong electron-electron interactions. As discussed in the previous sections, these modes pierce through the particle-hole continuum to emerge inside the energy gap between electron bands and thus become decoupled from the spectrum of electronic excitations. Such behavior is unlike that seen in conventional materials, Fig. 1-2a, where plasmon's dispersion at large momenta ultimately ends inside the continuum [32, 33, 34, 53]. The mechanisms behind the over-the-band plasmons were analyzed in the previous sections with the smoking-gun signature being the speckle-patterns measurable in SNOM measurements. In this section we discuss potential applications of the over-the-band plasmons.

1.5.1 Probing correlated states

In a correlated insulator at integer fillings interactions open a gap at the Fermi level. TBG exhibits such correlated insulating behavior at integer fillings and so it is necessary to address how will the gap opening affect the over-the-band modes. In the Chapter 3, we find that over-the-band plasmons exist irrespective of the nature of the correlated state. This is best exemplified by the Fig. 1-13 which shows a plasmon mode (bright red feature) inside an insulating regime where the gap at the Fermi level (see the inset) is opened by interactions.

The presence of the ordered state helps to elucidate the microscopic mechanisms behind the over-the-band behavior. Specifically, in the correlated insulator regime the only electronic transitions that contribute to the behavior seen in Fig. 1-13 originate from interband terms. These interband transitions, schematically depicted as blue arrows in the inset of Fig. 1-13, can be thought of as strongly-coupled particle-hole excitations. The microscopic origins of the over-the-band modes are therefore the same as the one behind the stiff mode of the Wigner solid from the previous section.

The large momentum behavior of the over-the-band modes turns out to be robust with only the subtle details of the plasmon dispersion being sensitive to the underlying properties of the low-energy electronic excitations. As discussed with help of the Eq. (1.15) the energy scale for plasmons is set by the characteristic scale of interband transitions. The size of the interaction induced energy gap, δu, therefore affects the characteristic energy scale of interband transitions, and softens plasmon dispersion:

$$\omega_{\mathrm{p}} \approx \sqrt{4\alpha W \left(1 - \frac{\delta u^2}{W^2}\right) v_F q} \quad \text{for} \quad \omega_{\mathrm{p}} \gg W \tag{1.19}$$

This behavior is to be expected as a gap between bands, here the δu, reduces the Bloch wavefunction overlap. A measurement of the plasmon stiffness at fillings just away and at the integer insulating value, therefore should allow to quantify the correlated energy gap, δu, giving rise to a new experimental probe of a correlated state.

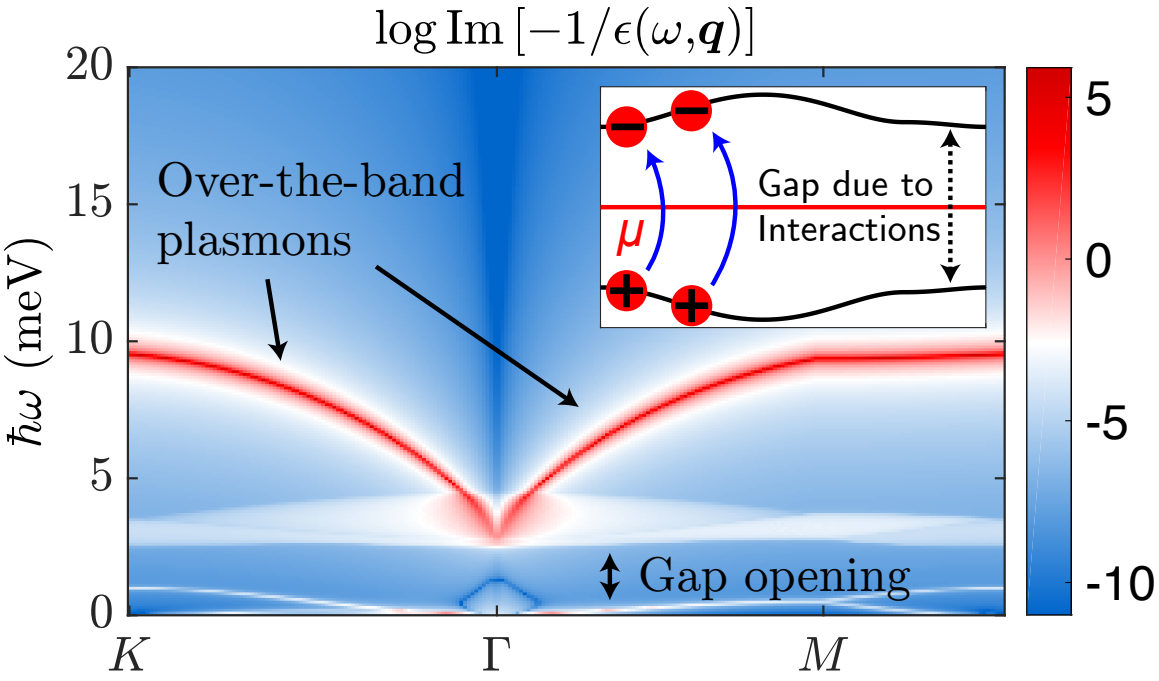

Figure 1-13: Electron loss function $\mathrm{Im}\,(-1/\varepsilon(\omega, \mathbf{q}))$ for a narrow-band toy model of a correlated Mott-Hubbard insulator. Interactions lead to a gap opening (see inset) at a Fermi level μ. Parameter values are chosen to mimic TBG bands (bandwidth $W = 3.75$ meV, lattice periodicity $L_M = 13.4$ nm, Fermi energy is placed inside the gap at $\mu = 0$ meV); log scale is used to clarify the relation between different features.

1.5.2 Plasmonic nonreciprocity driven by band hybridization in moiré materials

Time-reversal symmetry (TRS) breaking leads to the emergence of unidirectional modes, such as the chiral edge states of the quantum Hall effect [90, 91, 92], the quantum anomalous Hall effect [93, 94, 95, 96, 97], or the topological photonic crystals [98, 99, 100, 101, 102]. However, such modes, while holding exceptional promise for development of new devices, often require specific experimental conditions, such as strong magnetic fields, significant magnetic doping or a large macroscopic size of a device. This means that they are not easily susceptible to miniaturization necessary for the technological applications, which usually benefit from the on-chip integration on a nanoscale, or they cannot be easily coupled to electromagnetic radiation and hence provide greater experimental utility.

For these reasons, one of the alternative platforms in which nonreciprocity is a

highly sought-after property are the 2D surface plasmons [103, 104, 105, 106, 107, 108, 109, 110, 111, 112, 113, 114, 115]. An example of a plasmon dispersion relation with a TRS preserved is presented in Fig. 1-14(a). While a nonreciprocity in the plasmon dispersion, $\omega_{\rm p}(\mathbf{q}) \neq \omega_{\rm p}(-\mathbf{q})$, can be induced using magnetic field [116, 117, 118, 119], the 2D plasmon platform allows for an appealing alternative based on driving electric current through the devices - the so-called plasmonic Doppler effect [111, 112, 113, 114, 115, 120]. The essence of this phenomenon boils down to a simple Galilean transformation that distinguishes plasmons moving along and against the electric current. Electron flow modifies the plasmon dispersion with a correction, $\Delta\omega_{\rm p}^{(c)} \sim \mathbf{u}\cdot\mathbf{q}$, proportional to the drift velocity $\mathbf{u}$ and plasmon momentum $\mathbf{q}$. This current-induced nonreciprocity $\Delta\omega_{\rm p}^{(c)}$ of the plasmon dispersion is the conventional plasmonic Doppler effect.

Unfortunately, even in pristine 2D graphene samples, the drift velocity is a small fraction of the Fermi velocity [121, 122] and hence the relative magnitude of the Doppler effect [111]

$$\frac{\Delta\omega_{\rm p}^{(c)}(\mathbf{q})}{\omega_p^0(\mathbf{q})} \sim \frac{1}{\alpha}\frac{u}{v_F}\frac{\omega_p^0(\mathbf{q})}{|\mu|}, \quad \omega_p^0(\mathbf{q}) = \sqrt{4\alpha E_F v_F q} \tag{1.20}$$

is a small correction on the order of $\sim 3\%$ to the graphene plasmon dispersion in the absence of electron drift, $\omega_p^0(\mathbf{q})$ [9, 33, 34]. The presence of the parameter α in the drift-free part of the plasmon dispersion $\omega_{\rm p}^0(\mathbf{q})$ leads to a property $\omega_{\rm p}^0(\mathbf{q}) < |\mu|$ in realistic 2D material scenarios with $\alpha \lesssim 1$, and thus is an additional limitation in attempts to observe the conventional Doppler effect.

The narrow electron bands of moiré materials, in addition to being characterized by $\alpha \gg 1$, are also strongly hybridized with the rest of the electron bandstructure. This strong band hybridization leads to another, fundamentally quantum in nature, source of plasmonic nonreciprocity. This effect results in an asymmetry of the plasmon dispersion (as demonstrated in Fig. 1-14b), which is strongly enhanced by an

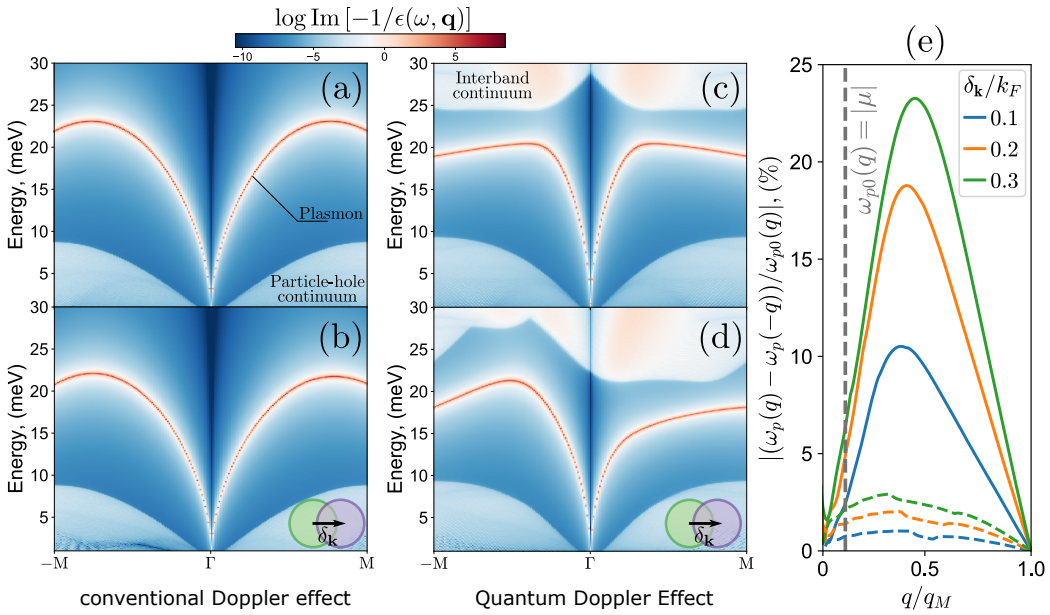

Figure 1-14: (a, b) Electron loss function of a unhybridized narrow-band toy-model (a) without and (b) with applied electric current at zero temperature. The conventional Doppler effect imposes only a small change on the plasmon dispersion. (c, d) Electron loss function of a hybridized narrow-band toy-model (c) without and (d) with applied electric current at zero temperature. Current flow leads to a TRS breaking and induces a nonreciprocity (asymmetry) in the plasmons' dispersion between positive and negative momenta. In (b,d) we set $\delta_{\mathbf{k}}/k_F = 0.3$. (e) A comparison of relative asymmetry between positive and negative momenta at several electron flow values (blue, orange, green). Here $\delta_{\mathbf{k}}$ is an electric-field-driven momentum shift of the Fermi surface. The dashed lines correspond to a conventional Doppler effect present in any system, Eq.(1.20). When bands become narrow and hybridized, strong asymmetry develops (the "Quantum Doppler effect", solid line), which origin is purely a consequence of a non-vanishing interband wavefunction overlap. The dielectric function plots (a-d) are obtained by numerically evaluating the polarization function from Eq.(1.12) using a tight-binding model described in the Chapter 4.

additional factor of α:

$$\Delta\omega_{\rm p}^{(q)}(\mathbf{q}) \sim \alpha \frac{\Delta_h^2 v_F q}{|\mu|^3} \mathbf{u}\cdot\mathbf{q}\,, \qquad \frac{\Delta\omega_{\rm p}^{(q)}(\mathbf{q})}{\omega_p^0(\mathbf{q})} \sim \frac{u}{v_F}\frac{\Delta_h^2 \omega_p^0(\mathbf{q})}{|\mu|^3}\frac{q}{k_F}\,. \tag{1.21}$$

Here Δ_h is the strength of hybridization between the two bands that opens up a gap between them. This linear dependence on α gives rise to a relative frequency shift that is amplified by the fine structure factor α unlike the conventional Doppler effect $\Delta\omega_{\rm p}^{(c)}(\mathbf{q})$. The origin of this additional source of plasmonic nonreciprocity can

be traced back to the electron bandstructure where individual bands are hybridized with one another. This is in contrast to the conventional plasmon Doppler effect, where the microscopic origins of the nonreciprocity can be ultimately understood simply through a shift of the reference frame, largely independent of the material parameters [120, 114]. A comparison of these two sources of nonreciprocity is shown in Fig. 1-14(c) for a narrow-electron band system with $\alpha \gg 1$ in the cases with and without band hybridization. As soon as the plasmon frequencies reach above the chemical potential $\omega_{\mathrm{p}}(\mathbf{q}) \gtrsim |\mu|$, a plasmon regime guaranteed by the presence of strong interactions $\alpha \gg 1$ as discussed in the previous sections, the quantum correction to the Doppler effect dominates over the conventional Doppler effect leading to a strong enhancement of plasmonic nonreciprocity.

This new source of plasmonic non-reciprocity in over-the-band modes has immediate consequences of both practical and fundamental importance. First of all, as mentioned above, it opens a pathway to development of optoelectronic devices with suppressed backscattering [98, 123, 124, 125, 126], for example plasmonic isolators based on Mach-Zehnder interferometers [127, 128], making the quantum doppler effect a valuable addition to the nanophotonics toolbox. Moreover, the drift-based mechanism enables a highly tunable electrical control of nonreciprocity on a nanoscale by simply controlling the current flow in the device. This on-chip compactness and tunability are in contrast to the mechanisms that employ the magnetic-based approaches. Finally, introducing a nonreciprocity to the dispersion of plasmons with quenched Landau damping is particularly appealing, as it paves a way towards a practical realization of various theoretical predictions, such as the Dyakonov-Shur instability [120], that were previously limited by the plasmonic lifespan.

1.6 Thesis outline

In this thesis, I discuss how strong electron-electron interactions present in narrow-band materials can give rise to a new type of plasmon behavior. These new plasmons pierce through the p-h continuum and extend in the forbidden energy band above it to

decouple from p-h excitations. As a material realization of these narrow-band systems we consider the moiré family of materials in particular the magic angle twisted bilayer graphene. We predict enhanced optical coherence for the over-the-band plasmons, which gives rise to a smoking gun signature in near field scanning optical microscopy measurements.

In Chapter 2, the over-the-band plasmon modes are first derived and their experimental signatures, speckle patterns, are identified. We analyze the origins of the over-the-band modes to demonstrate the strong dependence on the effective fine structure constant α. Our analysis is first carried out with the help of a simple toy-model of TBG's bandstructure, which captures the necessary features of the realistic MATBG bandstructure and allows us to identify the necessary ingredients for a system to exhibit over-the-band modes. We then introduce a realistic TBG continuum bandstructure model and use it to determine the dispersion of plasmons in MATBG demonstrating the presence of over-the-band modes.

To verify the robustness of the RPA analysis, in Chapter 3 we study the collective modes inside a correlated Mott-Hubbard insulator and a Wigner crystal. We find that the over-the-band plasmon behavior is robust with only the subtle details of the plasmon stiffness being dependent on the type of the low-energy order present in the system. This sensitivity to the nature of the low-energy state allows the over-the-band plasmons to be used as an experimental probe of the correlated state.

In Chapter 4 we consider the implications of the mechanisms behind the over-the-band behavior for achieving of unidirectional collective modes. We present a new mechanism for plasmon nonreciprocity the magnitude of which is controllable through the strength of electron-electron interactions, which makes it particularly pronounced in the moiré materials.

Finally, in Chapter 5, the main results of the thesis are summarized, and possible further extensions and applications of the over-the-band plasmon mechanism are discussed.

Chapter 2

Intrinsically undamped plasmon modes in narrow electron bands

2.1 Introduction

Landau damping, a process by which collective mode decays into electron-hole pairs, is often taken to be an integral attribute of graphene plasmon excitations[34, 33, 53, 50, 49]. In this chapter we predict extinction of this dissipation mechanism in materials with narrow electron bands such as twisted bilayer graphene (TBG)[129, 130, 54, 55, 131]. Intrinsically undamped plasmons in narrow-band materials arise due to large fine structure parameter values $\alpha = e^2/\hbar\kappa v_F$: strong interactions push plasmon dispersion into the energy gap above the particle-hole (p-h) continuum, as illustrated in Fig.2-1. As discussed below, in this region plasmons become decoupled from particle-hole pair excitations. Dissipation quenching, which is a surprising manifestation of strong coupling physics, is a robust effect that persists up to room temperature and is insensitive to disorder (see Figs.2-1,2-2). Collective charge modes which are damping-free are of keen interest for Quantum Information Science as a vehicle to realize dissipationless photon-matter coupling, high-Q resonators, single-photon phase shifters and other missing components for photon-based Quantum Information Processing toolbox[132]. While extinction of Landau damping is a general effect present in all narrow electron bands, our analysis will focus on TBG flat bands,

a system of high current interest[13, 14, 15, 75, 76] in which undamped plasmons can be directly probed.

2.2 Novel over-the-band behavior

The new behavior is illustrated in Fig.2-1, showing plasmon mode for a narrow-band model that mimics the key features of the TBG band. Mode dispersion (red line) is conventional at energies less than the bandwidth, $\omega \lesssim W$. At lowest energies, plasmon mode is positioned outside the p-h continuum; this suppresses the $T = 0$ Landau damping, but does not protect the mode from decaying into p-h excitations through disorder scattering or from the conventional $T > 0$ Landau damping[33, 34, 66, 10, 67, 68, 69]. At higher energies, $\omega \sim 2E_F$ (marked by arrow in Fig.2-1), the mode plunges into p-h continuum and is Landau-damped at $2E_F \lesssim \omega \lesssim 2W$ even at $T = 0$. However, a dramatic change occurs once the mode rises above the p-h continuum. In the forbidden gap region, $\omega > 2W$, it becomes *damping-free,* since at these energies there are no free e-h pairs into which plasmon could decay. This behavior is manifest in the T dependence of the resonances, which are washed out with increasing temperature at $\omega \lesssim W$ but remain sharp at $\omega > W$ even at $T \sim E_F$ (Fig.2-1 panels b and c).

As we will see, mode dispersion has a square-root form characteristic of two-dimensional (2D) plasmons,[32, 70]

$$\omega_{\rm p}(q) = \sqrt{\beta_q q}, \tag{2.1}$$

with a weak q dependence in β_q, see (2.15). This expression, however, is valid not just at low energies $0 < \omega \lesssim W$ but also at higher energies, $\omega \gg W$, where the mode is undamped. While the dispersion in (2.1) is of the conventional 2D plasmon form, we emphasize that here it takes on a new role, as it describes the plasmon mode at frequencies much higher than the carrier bandwidth, extending to

$$\omega_{\rm p} \sim \sqrt{\alpha} W \gg W, \quad \alpha \sim 20 - 30, \tag{2.2}$$

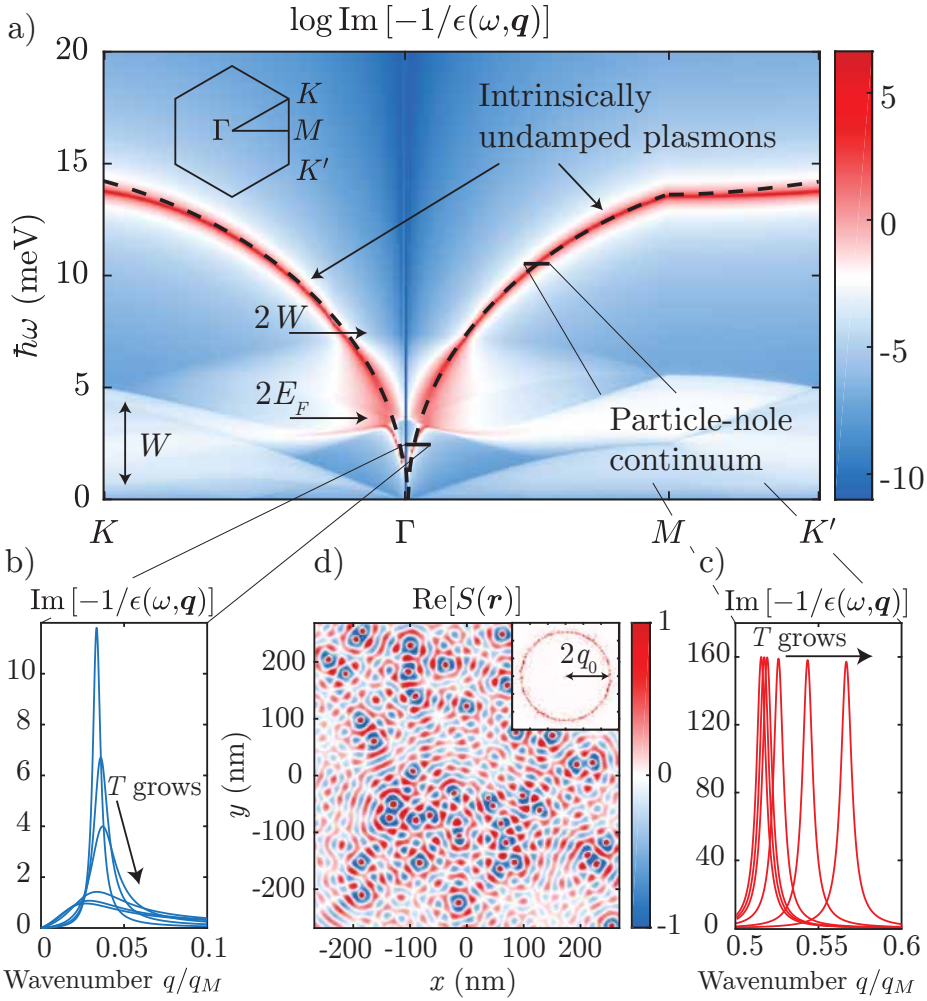

Figure 2-1: (a) Electron loss function $\mathrm{Im}\,(-1/\varepsilon(\omega,\mathbf{q}))$ for a narrow-band toy model (the hexagonal tight-binding model, (2.11)). Parameter values are chosen to mimic TBG bands (bandwidth $W = 3.75$ meV, lattice periodicity $L_M = 13.4$ nm, Fermi energy in the conduction band at $E_F \approx 1.81$ meV); log scale is used to clarify the relation between different features. Arrows mark the interband p-h continuum edges. Plasmon dispersion (red line) is fitted with $\omega_{\mathrm{p}}(q) = \sqrt{\beta_q q}$, (2.1) (dashed line). The difference between Landau-damped (b) and undamped behavior (c) is illustrated by linecuts of plasmon resonances at the locations marked in panel (a), taken at temperatures $T/E_F = 0, 0.075, 0.1, 0.2, 0.3, 0.4$. Resonances broaden with T in (b) and are T-independent in (c) [the residual resonance width models extrinsic damping due to phonons and disorder[52, 9, 48, 47]]. Resonances at the three lowest T values in (c) are slightly offset for clarity. (d) Speckle pattern in scanning near-field microscopy signal[49, 50] $S(\mathbf{r})$, (2.3), due to undamped plasmons; optical coherence is manifest in Fourier spectrum $|S_{\mathbf{k}}|^2$ (inset). Results shown are for plasmon momentum $q_0 = q_M/2 \approx 0.14$ nm^{-1}, where q_M is the distance between points M and Γ, and disorder modeled as 40 randomly placed point defects.

where the high α values correspond to flat bands in magic-angle moiré graphene. Unlike the conventional plasmons, the dispersion in (2.1) is not limited to longest wavelengths. Indeed, as illustrated Fig.2-1a, it extends to wavenumbers which are on the order of the superlattice Brillouin zone width.

Furthermore, the wavelength of the undamped plasmons is only 2-3 times greater than the moiré superlattice period. Such short wavelengths are of great interest for plasmonics and are within resolution of the state-of-the-art scanning near-field microscopy techniques[49, 50] [currently as good as 10nm [133, 7]]. In addition to measuring plasmon dispersion, these techniques can be used to directly visualize the qualitative change in the damping character and strength. Enhanced optical coherence will manifest itself in striking speckle-like interference, as illustrated in Fig.2-1 panel d) and Fig.2-2.

Indeed, because of the absence of Landau damping at the energies of interest, $\omega > W$, and also because these energies are smaller than carbon optical phonon energies, the dominant dissipation mechanism will be elastic scattering by disorder. At low energies, where plasmon mode coexists with p-h continuum, disorder scattering merely assists Landau damping, allowing plasmons to decay into p-h pairs by passing some of their momentum to the lattice. However, at the energies above p-h continuum, $\omega > W$, since the decay into pairs is quenched, disorder will lead to *predominantly elastic scattering* among plasmon excitations. Such scattering preserves optical coherence and is expected to produce speckle patterns in spatial near-field images, as illustrated in Fig.2-1d.

2.3 Experimental consequences

To model this behavior we consider the signal $S(\mathbf{r})$, excited by the scanning tip and measured at the same location. Monochromatic plasmon excitation at energy E is scattered by impurities or defects, and, upon returning to the tip, produces signal

$$S(\mathbf{r}) = J_0 \int d^2\mathbf{r}' G_E(\mathbf{r}-\mathbf{r}')\eta(\mathbf{r}')G_E(\mathbf{r}'-\mathbf{r}), \tag{2.3}$$

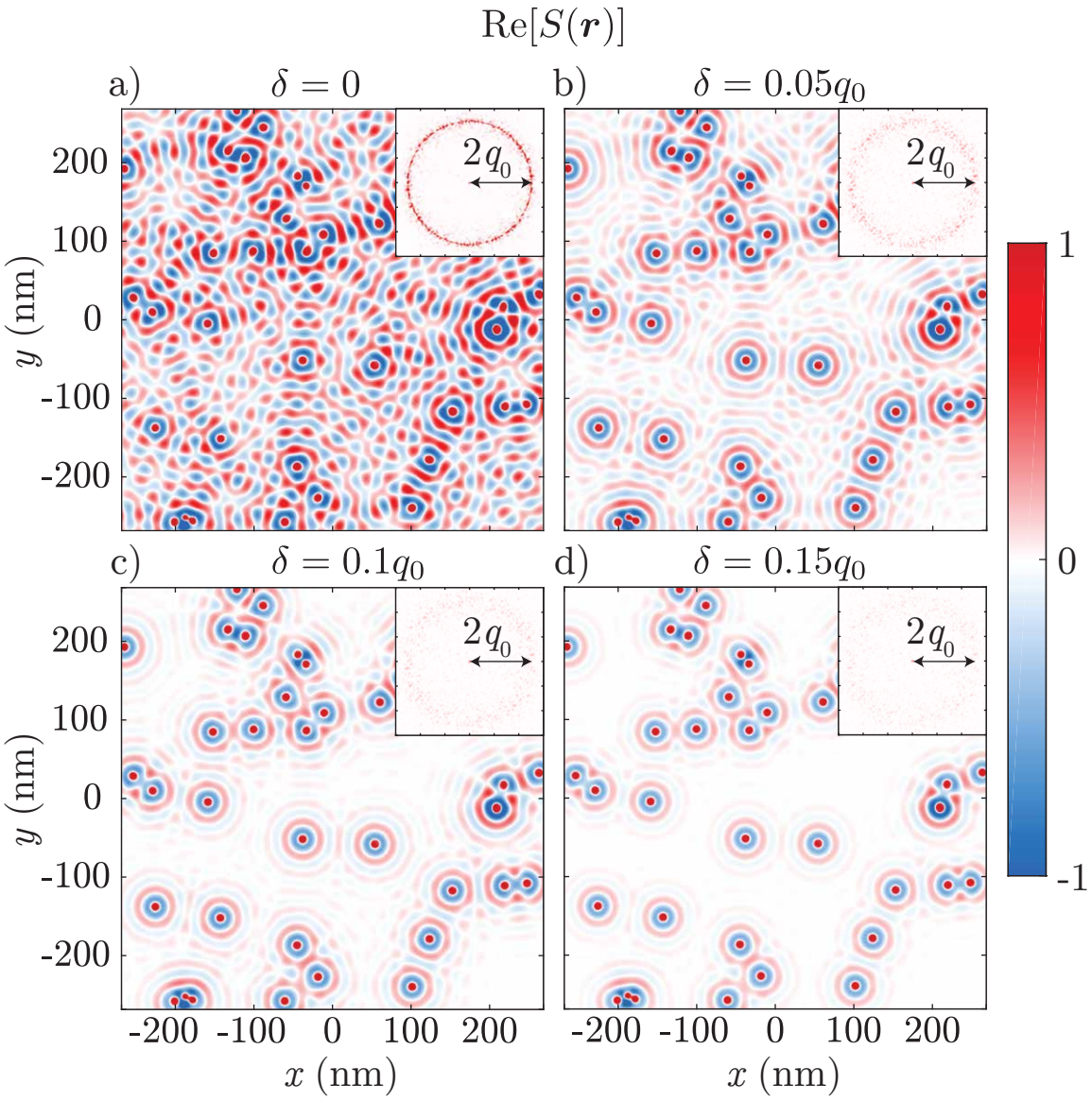

Figure 2-2: (a,b,c,d) Speckle patterns arising due to optical coherence of undamped plasmons in scanning near-field microscopy signal $S(\mathbf{r})$, (2.3), at various ratios of the incoherent to coherent damping δ/q_0. The insets show the corresponding square of the speckle pattern's Fourier transform amplitude $|S_{\mathbf{k}}|^2$. In all panels, for clarity of comparison, we set the plasmon momentum as in Fig.2-1d $q_0 = q_M/2 \approx 0.14$ nm^{-1} and vary only the ratio δ/q_0. The disorder is taken as 40 randomly placed delta functions.

where $\eta(\mathbf{r})$ is the disorder potential, J_0 is excitation amplitude, and $G_E(\mathbf{r})$ is the Green's function of the plasmon excitation (see the Appendix 2.10.1). The spatial signal, Fig.2-1d, exhibits a characteristic speckle pattern familiar from laser physics. In graphene plasmonics, speckle-like interference provides a direct manifestation of

optical coherence enhancement in the absence of Landau damping. Accordingly, the Fourier transform of the image, $S_{\mathbf{k}} = \int d^2 r S(\mathbf{r}) e^{-i\mathbf{kr}}$, yields power spectrum $|S_{\mathbf{k}}|^2$ that features a ring-like structure; the ring radius $k = 2q_0$, where q_0 is the plasmon excitation wavenumber (see Fig.2-1d inset). Simple calculation, described in the Appendix 2.10.1, predicts a sharp peak at the ring:

$$|S_{\mathbf{k}}|^2 \sim \frac{|\eta_{\mathbf{k}}|^2}{|k^2 - 4(q_0 - i\delta)^2|}, \tag{2.4}$$

where δ is a parameter characterizing extrinsic damping due to phonon scattering and other inelastic processes. In the fully coherent regime ($\delta = 0$) the quantity $|S_{\mathbf{k}}|^2$ exhibits a power law singularity at the ring, $k = 2q_0$. As the amount of incoherent scattering increases, the peak is gradually washed out. This behavior is illustrated in Fig.2-2.

2.4 Relation to previous works

We note that recent work [75] analyzed interband plasmon excitations in TBG, which are dominated by polarization of the bands above the flat band and are distinct from the flat-band plasmons analyzed here. Recent experiment[76] reported observation of plasmons in TBG, however their appeal for constructing intrinsically protected collective modes remained unnoticed in graphene literature. Also, plasmons in narrow bands were analyzed in the context of high-T_c superconductivity[77], finding that plasmon mode can rise above the flat band. However, in cuprates, unlike moiré graphene, the narrow band is not separated from higher bands by a forbidden energy gap, and thus the mode studied in Ref.[77] will plunge into a higher band before acquiring an undamped character. Our prediction of the intrinsically undamped plasmons in TBG and their potential subsequent observation therefore constitute an uncharted territory.

2.5 Minimal model

Next, we present analysis of the hexagonal-lattice toy model that mimics the key features of Landau-damped and intrinsically undamped modes in TBG. The hexagonal-lattice tight binding model possesses the same symmetry and the same number of sub-bands as the flat band in TBG. We match the energy and length scales by choosing the width of a single band W and the hexagonal lattice period L_M identical to the parameters in TBG: $W = 3.75$ meV and $L_M = a/2\sin(\theta/2)$ is the moiré superlattice periodicity. For the magic angle value $\theta = 1.05^\circ$, using carbon spacing $a = 0.246$ nm, this gives $L_M = 13.4$ nm. To ensure that a unit cell of the toy model can accommodate 4 electrons just as the moiré cell does in TBG, we make the toy model fourfold degenerate. Comparison to plasmons for the actual TBG model, presented below, will help us to identify the features which are general, as well as those which are a specific property of TBG.

Our nearest-neighbor tight-binding Hamiltonian is

$$H_{\rm toy} = \begin{pmatrix} 0 & h_{\mathbf{k}} \\ h_{\mathbf{k}}^* & 0 \end{pmatrix}, \quad h_{\mathbf{k}} = \frac{W}{3}\sum_{\mathbf{e}_j} e^{i\mathbf{k}\cdot\mathbf{e}_j}, \tag{2.5}$$

with the hopping matrix element $W/3$ to nearest neighbors at positions

$$\mathbf{e}_i = (\cos(2\pi j/3), \sin(2\pi j/3))L_M/\sqrt{3}\,, \quad j = 0, 1, 2\,. \tag{2.6}$$

Here W is the bandwidth measured from Dirac point and the nearest neighbor distance $L_M/\sqrt{3}$ is chosen such that the lattice period of the hexagonal toy model matches the moiré superlattice period. Corresponding energies $E_{s,\mathbf{k}}$ and eigenstates $\Psi_{s,\mathbf{k}}$ are then

$$E_{s,\mathbf{k}} = s|h_{\mathbf{k}}|, \quad \Psi_{s,\mathbf{k}} = \frac{1}{\sqrt{2}}\begin{pmatrix} se^{i\varphi_{\mathbf{k}}} \\ 1 \end{pmatrix}, \tag{2.7}$$

where $\varphi_{\mathbf{k}} = \arg h_{\mathbf{k}}$ and the band index $s = \pm$ labels the conduction and valence band.

2.6 Dielectric function and the RPA approximation

Plasmons can be obtained from the nodes of the complex dielectric function, describing the dynamical response of a material to an outside electric perturbation,

$$\varepsilon(\omega, \mathbf{q}) = 1 - V_{\mathbf{q}}\Pi(\omega, \mathbf{q}). \tag{2.8}$$

Here $V_{\mathbf{q}} = 2\pi e^2/\kappa q$ is the Coulomb interaction in a medium with a background dielectric constant κ and $\Pi(\omega, \mathbf{q})$ is the electron polarization function. The relation in (2.8) is exact so long as the polarization function is defined as an exact microscopic density-density pair correlator, given by a sum of all irreducible bubble diagrams. As such, this relation can yield useful information about plasmon dispersion even when electron interactions are strong.

Similar to the conventional analysis of plasmons in 2D systems, here a simplification occurs in the small-q limit regardless of whether the random phase approximation (RPA) is employed to evaluate $\Pi(\omega, \mathbf{q})$. Indeed, since the Coulomb potential diverges at small q, zeros of $\varepsilon(\omega, \mathbf{q})$ are found when the polarization function is small. However, at small q, this quantity vanishes as $\lambda q^2/\omega^2$, a behavior which is a consequence of the general symmetry requirements (namely, gauge invariance demanding that spatially uniform external potential does not perturb density)[4]. This immediately yields a $q^{1/2}$ scaling for plasmon frequency at small enough q.

Below we use the RPA approach to estimate the prefactor λ, and to demonstrate that the mode $\omega \sim q^{1/2}$ extends far above the TBG particle-hole continuum. To compare with other systems, we recall the familiar "classical acceleration" behavior found for particles with parabolic dispersion: $\Pi(\omega, \mathbf{q}) = n\mathbf{q}^2/m\omega^2$, where n is the charge density and m is the electron band mass[4]. For a more general band dispersion the ratio n/m is replaced by the band Fermi energy, $\lambda \sim E_F/\hbar^2$ [34, 33, 53]. Interactions have no impact on the behavior of $\Pi(\omega, \mathbf{q})$ for the parabolic band case, however for non-parabolic bands the band mass m must change to an effective value m^*, described by Landau Fermi-liquid renormalization [134].

In our case, the scaling relation $\Pi(\omega, \mathbf{q}) \approx \lambda q^2/\omega^2$ features different values of λ

for low and high energies, $\omega \lesssim E_F$ and $\omega > 2W$. To see this, we start with the RPA expression for polarization function

$$\Pi(\omega, \mathbf{q}) = 4 \sum_{\mathbf{k},s,s'} \frac{(f_{s,\mathbf{k+q}} - f_{s',\mathbf{k}}) F^{ss'}_{\mathbf{k+q},\mathbf{k}}}{E_{s,\mathbf{k+q}} - E_{s',\mathbf{k}} - \omega - i0}. \tag{2.9}$$

Here summation $\sum_{\mathbf{k}}$ denotes integration over the Brillouin zone (BZ), the indices s, s' run over the electron bands and the factor of 4 in front of the summation accounts for the fourfold degeneracy of the toy model. Here $f_{s,\mathbf{k}}$ is the equilibrium distribution $1/(e^{\beta(E_{s,\mathbf{k}} - E_F)} + 1)$, and $F^{ss'}_{\mathbf{k+q},\mathbf{k}}$ describes band coherence factors. For our toy model

$$F^{ss'}_{\mathbf{k+q},\mathbf{k}} = |\langle \Psi_{s,\mathbf{k+q}} | \Psi_{s',\mathbf{k}} \rangle|^2 = \frac{1 + ss' \cos(\varphi_{\mathbf{k+q}} - \varphi_{\mathbf{k}})}{2}, \tag{2.10}$$

where $\Psi_{s,\mathbf{k}}$ are pseudospinors given in (2.7).

2.6.1 Analytic results

As we now show, an analytic expression for plasmon dispersion can be obtained, describing both the Landau-damped and the undamped cases in a unified way. We first rewrite (2.9) by performing a standard replacement $\mathbf{k} + \mathbf{q} \to -\mathbf{k}$ in the term containing $f_{s,\mathbf{k+q}}$ followed by $-\mathbf{k} - \mathbf{q}, -\mathbf{k} \to \mathbf{k} + \mathbf{q}, \mathbf{k}$ justified by the $\mathbf{k} \to -\mathbf{k}$ time-reversal symmetry. This gives

$$\Pi(\omega, \mathbf{q}) = 8 \sum_{\mathbf{k},s,s'} f_{s',\mathbf{k}} \frac{F^{ss'}_{\mathbf{k},\mathbf{k+q}} (E_{s',\mathbf{k}} - E_{s,\mathbf{k+q}})}{(E_{s,\mathbf{k+q}} - E_{s',\mathbf{k}})^2 - (\omega + i0)^2}. \tag{2.11}$$

The behavior of this expression at small $\mathbf{q}$, which will be of interest for us, can be found in a closed form. In the small-q limit the coherence factors behave as

$$F^{s=s'}_{\mathbf{k+q},\mathbf{k}} \approx 1, \quad F^{s=-s'}_{\mathbf{k+q},\mathbf{k}} \approx \frac{1}{4} \left(\mathbf{q} \cdot \nabla_{\mathbf{k}} \varphi_{\mathbf{k}}\right)^2 \tag{2.12}$$

The values $O(1)$ for intraband transitions and $O(\mathbf{q}^2)$ for interband transitions might suggest that the polarization function is dominated by the intraband transitions.

However, as we now show, the interband and intraband contributions are of the same order of magnitude.

2.6.2 Interband and intraband contributions to polarization function

Indeed, the intraband contributions, $s = s'$, can be rewritten by noting that upon integration over $\mathbf{k}$ only the even-$\mathbf{k}$ part of series expansion $E_{s,\mathbf{k}+\mathbf{q}} - E_{s,\mathbf{k}}$ survives, giving $\Pi_1(\omega, \mathbf{q}) \approx \frac{4}{\omega^2} \sum_{\mathbf{k},s} f_{s,\mathbf{k}} \left(E_{s,\mathbf{k}+\mathbf{q}} + E_{s,\mathbf{k}-\mathbf{q}} - 2E_{s,\mathbf{k}}\right)$. Expanding in small $\mathbf{q}$, we have

$$\Pi_1(\omega, \mathbf{q}) \approx \frac{4}{\omega^2} \sum_{\mathbf{k},s} f_{s,\mathbf{k}} (\mathbf{q} \cdot \nabla_{\mathbf{k}})^2 E_{s,\mathbf{k}} \tag{2.13}$$

As a sanity check, for parabolic band $E_{\mathbf{k}} = \mathbf{k}^2/2m$ we recover the familiar result $\Pi(\omega, \mathbf{q}) = n\mathbf{q}^2/m\omega^2$[4].

The interband contributions, $s = -s'$, can be simplified by noting that $E_{s,\mathbf{k}+\mathbf{q}} \approx -E_{s',\mathbf{k}}$, giving

$$\Pi_2(\omega, \mathbf{q}) \approx 4 \sum_{\mathbf{k},s} f_{s,\mathbf{k}} \frac{E_{s,\mathbf{k}} \left(\mathbf{q} \cdot \nabla_{\mathbf{k}} \varphi_{\mathbf{k}}\right)^2}{4E_{s,\mathbf{k}}^2 - (\omega + i0)^2}. \tag{2.14}$$

As a sanity check, at $T = 0$ the imaginary part of Π_2, describing interband transitions, is nonzero only for $2E_F < \omega < 2W$, as expected. The real part of Π_2 is negative at small ω and positive at large ω because the valence band contribution dominates over that of the conduction band.

2.7 Over-the-band plasmon dispersion

Plasmon dispersion ω_{p} is given by the solution of the equation $\varepsilon(\omega, \mathbf{q}) = 0$ with $\Pi = \Pi_1 + \Pi_2$. Comparing the ω dependence of Π_1 and Π_2, we see that at small frequencies, $\omega < 2E_F$, the intraband contribution Π_1 dominates. This gives the

dispersion in (2.1) with

$$\beta_q = \beta_0 + \beta_1 q + O(q^2) \tag{2.15}$$

where the leading term $\beta_0 = 4\alpha v_F E_F/\hbar$ originates from Π_1 (see the Appendix 2.10.2) and the subleading q-dependent contribution is due to Π_2. Negative sign of Π_2 translates into $\beta_1 < 0$, softening the dispersion at low frequencies. This behavior, which holds the limit $\omega < 2E_F$, agrees with Refs.[34, 33, 70].

In the same manner we can obtain the dispersion at high frequencies, $\omega > 2W$ (the intrinsically undamped regime). The analysis is again simplified by noting that, since $\alpha = e^2/\hbar\kappa v_F \gg 1$, the relevant values of $\mathbf{q}$ are small compared to the Brillouin zone size, and thus the small-q limit considered above is sufficient to describe this new behavior. Taking both the intraband and interband contributions in the asymptotic form $\Pi_1 = \lambda_1 \mathbf{q}^2/\omega^2$, $\Pi_2 = \lambda_2 \mathbf{q}^2/\omega^2$ where $\lambda_1 \approx 2E_F/\hbar^2\pi, \lambda_2 \approx 2(W - E_F)/\hbar^2\pi$ (see the Appendix 2.10.2), yields (2.1) with $\beta = \frac{2\pi e^2}{\kappa}(\lambda_1 + \lambda_2)$. The first term is identical to β_0 found at low frequencies, the second term is of a positive sign, $\lambda_2 > 0$, describing hardening of the plasmon dispersion due to interband transitions.

In the undamped regime, plasmon frequency peaks at q values on the order of Brillouin zone scale. The peak value of ω_{p}, given in (2.2), can be found by estimating the energy differences $E_{s,\mathbf{k}+\mathbf{q}} - E_{s',\mathbf{k}}$ in (2.11) as W and noting that the coherence band factor for large q is in general non-vanishing and of order 1. This gives for the practically interesting case of $E_F \sim W$ the result $\omega_{\mathrm{p}} \sim \sqrt{\alpha}W$, which agrees with the dispersion $\omega_{\mathrm{p}} = \sqrt{\beta q} = 2\sqrt{\alpha v_F W q/\hbar}$ provided that $\hbar v_F q$ saturates at W. Indeed the estimated values of β_0, β as compared to the fitted curve in Fig.2-1a (see the Appendix 2.10.2) indicate that $\omega_{\mathrm{p}} = \sqrt{\beta_q q}$ relation from (2.1) is a good approximation for the plasmon dispersion at both small and large q.

The dielectric function of the two-band toy model faithfully reproduces all of the qualitative features expected for the TBG bandstructure. However, we find that, despite matching the bandwidth W and lattice period to those of TBG, the resulting plasmon dispersion extends to much higher energies then those that will be found below for the actual TBG bandstructure. This is simply because the two-band model

does not account for the effects of interband polarization of higher electron bands, which renormalize the dielectric constant down and soften the plasmon dispersion. We account for this in the toy model case by rescaling the effective fine structure constant such that the resulting plasmon dispersion is comparable in magnitude to the TBG result. Specifically in Fig. 2-1a we use an effective background dielectric constant $\kappa = 12.12$, which is four times larger than the dielectric constant $\kappa = 3.03$ corresponding to an air/TBG/hBN heterostructure.

2.8 Plasmon modes in a realistic bandstructure model

Next, we turn to the analysis of plasmons in TBG flat bands at an experimentally relevant magic angle value $\theta = 1.05°$[13, 14, 15]. To accurately describe the TBG bandstructure and eigenstates we employ the effective continuum Hamiltonian H_{TBG} introduced in Ref.[60]. The full discussion of the bandstructure details can be found in the Appendix 2.10.3; here we only discuss two relevant energy scales: flat-band bandwidth W, and the gap Δ between the flat-bands and the rest of the bandstructure. With regard to W value we note that, technically, the bandwidth of the flat-bands, as predicted by the continuum mode H_{TBG}, is on the order of $W \approx 3.75$ meV. However, the bandwidth scale relevant for the interband and intraband excitations is actually closer to $\tilde{W} \approx 2$ meV, because most of the states in the band lie below 2meV. In addition, since the states with energies outside $-2\,\mathrm{meV} < E < 2\,\mathrm{meV}$ are small-k, their contribution to polarization function, (2.14), (2.13), evaluated at small $\mathbf{q}$, is small. We also note that, while the bandgap as predicted by the continuum model is $\Delta \approx 11.75$ meV, the actual gap size is still a subject of debate[135].

2.8.1 Dielectric function of TBG

The definition of the polarization function for the TBG continuum model is identical to the one of the tight binding toy model, (2.9), with exception of requiring the valley and spin degrees of freedom to be accounted for explicitly, a larger number of electron bands and different coherence factors. The first two issues are resolved by

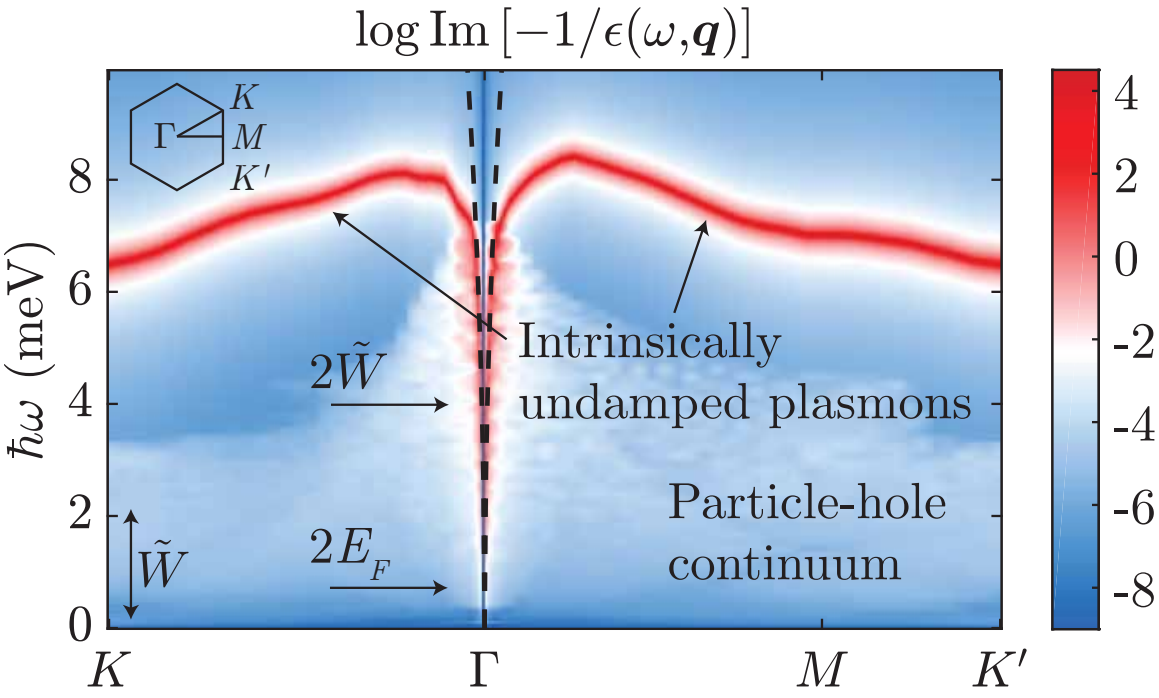

Figure 2-3: Electron loss function Im $(-1/\varepsilon(\omega, \mathbf{q}))$ for TBG bandstructure. The Fermi energy value $E_F = 0.289$meV corresponds to electron band half-filling; and set the average background dielectric constant is $\kappa = 3.03$ (typical of an air/TBG/hBN heterostructure). Log scale is used to clarify the relation between different features. Arrows mark the approximate interband p-h continuum edges, obtained for the effective bandwidth $\tilde{W} \approx 2$ meV (see text). Plasmon dispersion (red line) at small q is fitted with $\omega_{\rm p}(q) = \sqrt{\beta_q q}$, (2.1) (dashed line), demonstrating a significant deviation from the typical 2D plasmon dispersion at large q. In the calculation we used both flat-bands and the next conduction/valence non-flat bands, and verified that higher bands do not alter the quantitative and qualitative behavior.

promoting the band indices s, s' in (2.9) to composite labels n, m, which range over all electron bands, spins σ and valleys ξ making the additional factor of 4 in front of (2.9) unnecessary. Instead of the toy model coherence factors we use the TBG coherence band factors $F^{nm}_{\mathbf{k+q},\mathbf{k}}$, which are given by

$$F^{nm}_{\mathbf{k+q},\mathbf{k}} = \left| \int_\Omega d^2 r \Psi^\dagger_{n,\mathbf{k+q}}(\mathbf{r}) e^{i\mathbf{q}\cdot\mathbf{r}} \Psi_{m,\mathbf{k}}(\mathbf{r}) \right|^2, \tag{2.16}$$

where $\Psi_{n,\mathbf{k}}(\mathbf{r})$ are the Bloch wavefunctions for momentum $\mathbf{k}$ and band/valley/spin composite label n, which diagonalize the continuum Hamiltonian (see the Appendix 2.10.3). The integral in (2.16) is carried over the moiré unit cell Ω.

2.8.2 TBG plasmons - numerical solution

Once the polarization function is evaluated, we can determine the dielectric function and identify TBG's collective modes from poles of $1/\varepsilon(\omega, \mathbf{q})$, as above. An example of a TBG's dielectric function at approximately half-filling of the electron band, $E_F = 0.289$ meV, is shown in Fig.2-3; fixed-q linecuts and zeros of $\varepsilon(\omega, \mathbf{q})$ are illustrated in supplementary section 4. In discussing the figure it is helpful to contrast it with the calculation for the hexagonal-lattice toy model shown in Fig.2-1a. We again see a well defined intrinsically undamped plasmon mode ω_p (red) positioned above the p-h continuum; the mode resides inside the band gap $2W < \omega_\mathrm{p} < W + \Delta$, which peaks at $\hbar\omega_\mathrm{p} \approx 8.5$ meV before decreasing and becoming almost flat $\hbar\omega_\mathrm{p} \approx 6.5$ meV at large momenta. In agreement with the analytic considerations above, we see the interband continuum extending from $2E_F$ to $2W$, but since $E_F = 0.289$ meV is extremely small it makes the conventional (Landau-damped) part of plasmon dispersion $\omega < 2E_F$ invisible on the figure.

2.8.3 TBG plasmons - analytical considerations

There are several unique aspects of the TBG plasmon dispersion, as compared to the behavior of generic narrow-band plasmons discussed above. To analyze the dispersion

at $\omega_{\rm p} > 2W$, we proceed just as in the toy model case, rewriting the TBG polarization function in a slightly different form of (2.11), where the indices n, m and the band coherence factor are modified as described above.

However, unlike the two-band toy model case, to proceed further analytically we need to split the summation over TBG bands in (2.11) into two general types of terms: pairs of indices n, m such that (on average) we expect $\omega^2 > (E_{m,\mathbf{k+q}} - E_{n,\mathbf{k}})^2$ to hold, and pairs of indices n, m where the opposite $\omega^2 < (E_{m,\mathbf{k+q}} - E_{n,\mathbf{k}})^2$ is true. To leading order in ω we can therefore rewrite the dielectric function as

$$\varepsilon(\omega, \mathbf{q}) \approx 1 + A(\mathbf{q}) - \frac{B(\mathbf{q})}{\omega^2}, \tag{2.17}$$

where we defined two auxiliary functions:

$$A(\mathbf{q}) = \frac{8\pi e^2}{\kappa q} \sum_{\mathbf{k},n,m}{}' f_{m,\mathbf{k}} \frac{F^{nm}_{\mathbf{k+q},\mathbf{k}}}{E_{n,\mathbf{k+q}} - E_{m,\mathbf{k}}} \tag{2.18}$$

and

$$B(\mathbf{q}) = \frac{8\pi e^2}{\kappa q} \sum_{\mathbf{k},n,m}{}'' f_{m,\mathbf{k}} F^{nm}_{\mathbf{k+q},\mathbf{k}} (E_{n,\mathbf{k+q}} - E_{m,\mathbf{k}}). \tag{2.19}$$

Here the band summations $\sum'$ and $\sum''$ run over bands such that $\omega^2 > (E_{n,\mathbf{k+q}} - E_{m,\mathbf{k}})^2$ and $\omega^2 < (E_{n,\mathbf{k+q}} - E_{m,\mathbf{k}})^2$, respectively. E.g. at large momenta, as seen in Fig.2-3, the plasmon mode lies in the gap between the flat and non-flat bands and hence the $B(\mathbf{q})$ summation extends only over the flat bands, whereas the summation in $A(\mathbf{q})$ includes all of the remaining combinations of band indices. This allows us to write a closed form expression for the plasmon dispersion as

$$\omega_{\rm p}^2 \approx \frac{B(\mathbf{q})}{1 + A(\mathbf{q})}, \tag{2.20}$$

which must hold for both small and large q. We consider these two limits separately.

At small q the matrix element of the Bloch wavefunctions, just as in the toy model case, favours the overlap between states from the same band. At the same time there are fewer states in the $A(\mathbf{q})$ satisfying the condition $\omega^2 > (E_{n,\mathbf{k+q}} - E_{n,\mathbf{k}})^2$

and hence $A(\mathbf{q})$ vanishes for small q. This amounts to the plasmon dispersion ω_{p} from (2.20) reducing to $\omega_{\mathrm{p}}^2 \approx B(\mathbf{q})$ and, by comparison with (2.13), we similarly expect a conventional 2D plasmon dispersion $\omega_{\mathrm{p}} = \sqrt{\beta_q q}$ with β_q given by the series from (2.15). As we see in Fig.2-3, the $\omega_{\mathrm{p}} = \sqrt{\beta_q q}$ dispersion is a valid description only at very small q, as compared to Fig.2-1a, which can be traced back to higher bands softening the plasmon dispersion through the $A(\mathbf{q})$ term in (2.20).

To determine how high the plasmon mode rises above the p-h continuum, we consider large q values comparable to the reciprocal lattice vector. The arguments similar to those in the toy model show that, since $\alpha \gg 1$, we have $A(\mathbf{q}) \gg 1$. The dependence on the $e^2/\kappa q$ ratio therefore cancels between the $A(\mathbf{q})$ and $B(\mathbf{q})$ functions resulting in the value of the plasmon dispersion $\hbar\omega_{\mathrm{p}} \approx \sqrt{B(\mathbf{q})/A(\mathbf{q})} \sim \sqrt{W\Delta} \approx 6.6$ meV being dictated only by the continuum model's bandstructure parameters. This lack of explicit dependence on α suggests that, once the doping is such that $\alpha \gg 1$, the large-q value of $\hbar\omega_{\mathrm{p}} \approx \sqrt{W\Delta}$ becomes insensitive to doping (and hence Fermi velocity). This behavior is different than that in the toy model where $\omega_{\mathrm{p}} \sim \sqrt{\alpha}W$ at large q. The relatively more week dependence on α in the TBG case is due to interband polarization involving higher bands, which significantly alters the effective dielectric constant. The weak q dependence at large q is in agreement with the properties of interband plasmons described in Ref.[75].

We also note that although plasmons above the particle-hole continuum are kinematically protected from particle-hole excitation, which makes them undamped at the RPA level, there exist relaxation pathways through higher-order pair-production in which several electron-hole pairs are emitted with total energy exceeding $\tilde{W}$. However, analysis shows that such processes lead to imaginary corrections to the polarization function that are suppressed by factors of q^2/k_F^2 for each additional excited electron-hole pair [51]. Thus in a narrow-bandwidth system the plasmon mode will remain practically undamped for a wide range of momenta $\mathbf{q}$ before the multiparticle pair-production becomes a relevant relaxation pathway.

2.9 Outlook

Before closing, we note that suppressing damping has always been central to the quest for tightly-confined low-loss surface plasmon excitations. An early approach utilized surface EM modes traveling at the edge of an air/metal boundary[136], in which dissipation is low because most of the EM field resides outside the metal, however the field confinement scale is on the order of optical wavelength. Next came surface plasmons propagating in high-mobility 2D GaAs-based electron gases and graphene-hBN heterostructures[47], which can provide deep-subwavelength confinement[53]. However, plasmons in these systems are prone to a variety of dissipation mechanisms, with Landau damping usually regarded as the one that sets the fundamental limit on possible plasmon wavelengths and corresponding lifetimes. The possibility to overcome this fundamental limitation in narrow band systems such as moiré graphene, discussed above, opens a new line of investigation in graphene plasmonics. Damping-free plasmons can enable novel interference phenomena, dissipationless photon-matter coupling, and other interesting behaviors. It is also widely expected that low-dissipation plasmons can lead to unique applications for photon-based Quantum Information Processing [132]. Furthermore, reduced damping has more immediate consequences, as it translates into enhanced optical coherence that can be directly probed by scanning near-field microscopy, as discussed above, providing a clear signature of the intrinsically undamped collective modes.

2.10 Appendix

2.10.1 Spatial speckle patterns in near-field optical microscopy

Here we elaborate on the analysis connecting Eq.(2.3) and the speckle patterns shown in Fig.2-1d and Fig.2-2a-d. For an in-depth discussion of the near-field optical microscopy measurement technique and quantitative modeling of the detected signal we refer the reader to Refs.[50, 49, 47].

As argued in the main text, we can estimate the strength of the measured signal

in the near-field opical microscopy by evaluating the equal-point correlation function Eq. (2.3), which here we restate for convenience:

$$S(\mathbf{r}) = J_0 \int d^2\mathbf{r}' G_E(\mathbf{r}-\mathbf{r}')\eta(\mathbf{r}')G_E(\mathbf{r}'-\mathbf{r}). \tag{2.21}$$

It describes an amplitude of plasmon excitation, which traveled from the tip at position $\mathbf{r}$ to a disorder at position $\mathbf{r}'$ and was then reflected back towards the tip at $\mathbf{r}$. Here the Green's function $G_E(r)$ of the plasmon excitation of wavenumber q_0 is taken in the limit $rq_0 \gg 1$ as

$$G_E(\mathbf{r}) \approx \frac{e^{iq_0|\mathbf{r}|}}{\sqrt{2\pi|\mathbf{r}|}} e^{-\delta|\mathbf{r}|}, \tag{2.22}$$

which describes radially propagating waves in 2D. The factor $e^{-\delta|\mathbf{r}|}$ describes damping due to extrinsic effects such as phonons and other inelastic processes. Upon substitution of the Green's function into (2.21), the measured signal $S(\mathbf{r})$ is given by

$$S(\mathbf{r}) = J_0 \int d^2\mathbf{r}' \eta(\mathbf{r}') \frac{e^{i2q_0|\mathbf{r}-\mathbf{r}'|} e^{-2\delta|\mathbf{r}-\mathbf{r}'|}}{2\pi|\mathbf{r}-\mathbf{r}'|}. \tag{2.23}$$

This expression, which is a convolution of two functions, will generate a product under Fourier transform.

For purposes of Fig.2-1d and Fig.2-2a-d we evaluate the above convolution numerically by using the convolution theorem, that is first performing a fast Fourier transform of both terms individually, multiplying them and then carrying out an inverse Fourier transform. The inset of Fig.2-1d and Fig.2-2a-d is the intermediate step of this process, but we can also determine it analytically by evaluating the Fourier transform of the signal $S(\mathbf{r})$

$$S_{\mathbf{k}} = \int d^2\mathbf{r} e^{-i\mathbf{k}\cdot\mathbf{r}} S(\mathbf{r}). \tag{2.24}$$

As expected by the convolution theorem the expression factorizes into a product of

two separate factors

$$S_{\mathbf{k}} = \int d^2\mathbf{r}'\eta(\mathbf{r}')e^{-i\mathbf{k}\cdot\mathbf{r}'}\int d^2\mathbf{r}\frac{e^{-i\mathbf{k}\cdot\mathbf{r}+i2q_0|\mathbf{r}|}e^{-2\delta|\mathbf{r}|}}{2\pi|\mathbf{r}|}, \tag{2.25}$$

where the first factor is nothing but the Fourier harmonic of $\eta(\mathbf{x})$ and the second factor is the r-r' influence function, simplified by performing a variable change $\mathbf{r}-\mathbf{r}' \to \mathbf{r}$. To evaluate the integral over $d^2\mathbf{r}$ we first integrate over $|\mathbf{r}|$ and then carry out angular integration using the identity

$$\int_0^{2\pi} d\theta \frac{1}{a+b\cos\theta} = \frac{2\pi}{\sqrt{a^2-b^2}}. \tag{2.26}$$

After substituting $a = k$, $b = 2k_0 + 2\delta i$ this gives Eq. (2.4) of the main text.

2.10.2 Behavior of the intraband and interband polarization functions

Here we discuss the behavior of the intraband and interband polarization functions $\Pi_1(\omega, \mathbf{q})$ and $\Pi_2(\omega, \mathbf{q})$ of the toy model, defined in Eqs.(2.13),(2.14) of the main text. In particular, we estimate the coefficients λ_1 and λ_2 describing the small-q behavior of Π_1 and Π_2, defined in the paragraph beneath Eq.(2.15). We are mostly interested in high frequency values $\omega > 2W$ describing the intrinsically undamped regime.

We start with the quantity λ_2 describing the contribution of intraband transitions. At small q, the interband coherence factor from Eq. (2.12) is non-negligible only in proximity of the points K and K'. Near these points a linear dispersion $E_{s,\mathbf{k}} = sv_F k$, with $s = \pm 1$, is a good approximation for the bandstructure. In that limit, the small-q interband coherence band factor from Eq. (2.14) becomes

$$F^{s=-s'}_{\mathbf{k}+\mathbf{q},\mathbf{k}} \approx \frac{1}{4}\left(\mathbf{q}\cdot\nabla_{\mathbf{k}}\varphi_{\mathbf{k}}\right)^2 \approx \frac{1}{4}\frac{q^2}{k^2}\sin^2\theta, \tag{2.27}$$

where θ is the angle between $\mathbf{k}$ and $\mathbf{q}$. The quantity $\Pi_2(\omega, \mathbf{q})$ is therefore given by:

$$\Pi_2(\omega, \mathbf{q}) = -\frac{8q^2}{\omega^2} \sum_{\mathbf{k},s} f_{s,\mathbf{k}} s v_F k \frac{\sin^2\theta}{k^2}. \tag{2.28}$$

In the above we used the linear dispersion approximation $E_{s,\mathbf{k}} = s v_F k$ for the whole band and accounted for the K and K' points through an additional factor of 2. This gives

$$\Pi_2(\omega, \mathbf{q}) \approx -\frac{2E_F}{\pi}\frac{q^2}{\omega^2} + \frac{2W}{\pi}\frac{q^2}{\omega^2} = \frac{2}{\pi}(W - E_F)\frac{q^2}{\omega^2}, \tag{2.29}$$

with the first and second terms originating from the conduction band and the valence band respectively. This gives

$$\lambda_2 = 2(W - E_F)/\pi, \tag{2.30}$$

which takes positive values since $-W < E_F < W$.

Next, we proceed to estimate the λ_1. Without loss of generality, we place the Fermi energy in the conduction band. In this case, the interband contribution to the polarization function is non-vanishing only in the conduction band. This can be seen by going back to the Eq. (2.11), which for $s = s' = -1$ and small q vanishes:

$$\Pi_1(\omega, \mathbf{q}) \approx -\frac{8}{\omega^2} \sum_{\mathbf{k}} f_{-1,\mathbf{k}} (E_{-1,\mathbf{k}} - E_{-1,\mathbf{k}+\mathbf{q}}) \tag{2.31}$$

$$= -\frac{8}{\omega^2} \sum_{\mathbf{k}} (E_{-1,\mathbf{k}} - E_{-1,\mathbf{k}+\mathbf{q}}) = 0, \tag{2.32}$$

since $f_{-1,\mathbf{k}} = 1$ for all $\mathbf{k}$ in the valence band. It is therefore sufficient to focus on the contribution of the partially filled (conduction) band. To be consistent with the λ_2 analysis above we replace the dispersion energy as $E_{1,\mathbf{k}} = v_F k$. The intraband contribution to the polarization function $\Pi_1(\omega, \mathbf{q})$ is then

$$\Pi_1(\omega, \mathbf{q}) \approx \frac{8q^2}{\omega^2} \sum_{\mathbf{k}} f_{1,\mathbf{k}} v_F \frac{\sin^2\theta}{k} = \frac{2}{\pi} E_F \frac{q^2}{\omega^2}, \tag{2.33}$$

giving

$$\lambda_1 = 2E_F/\pi. \tag{2.34}$$

As argued in the main text [see discussion below Eq. (2.15)], this result remains unchanged for frequencies $\omega < 2E_F$ and, therefore,

$$\beta_0 = 4\alpha v_F E_F. \tag{2.35}$$

Going back to the $\omega > 2W$ regime, and using λ_1 and λ_2 derived above, gives the square-root plasmon dispersion $\omega_{\rm p} = \sqrt{\beta q}$ with

$$\beta = \frac{2\pi e^2}{\kappa}(\lambda_1 + \lambda_2) = 4\alpha v_F W. \tag{2.36}$$

Therefore, at small $\omega < 2E_F$ the dispersion behaves as $\omega_{\rm p} = 2\sqrt{\alpha v_F E_F q}$, becoming enhanced at high energies $\omega > 2W$, $\omega_{\rm p} = 2\sqrt{\alpha v_F W q}$ by a factor $\sqrt{W/E_F}$.

To complete the analysis of the polarization function behavior, now we focus on frequencies in the region $2E_F < \omega < 2W$. Working again in the small-q limit we find that, as pointed out earlier, only the interband contribution to the polarization function $\Pi_2(\omega, \mathbf{q})$ develops an imaginary part, whereas the intraband polarization function $\Pi_1(\omega, \mathbf{q})$ is real-valued, given by the (2.33). To determine the form of $\Pi_2(\omega, \mathbf{q})$ in the interband p-h continuum energy range, we approximate the coherence factor as in Eq.(2.27) to obtain

$$\Pi_2(\omega, \mathbf{q}) \approx 8 \sum_{\mathbf{k},s} f_{s,\mathbf{k}} \frac{s v_F k}{4 v_F^2 k^2 - (\omega + i0)^2} \times \frac{q^2}{k^2} \sin^2\theta. \tag{2.37}$$

Here we used the linear approximation to the energy dispersion $E_{s,\mathbf{k}} = s v_F k$, accounting for the fact that, because of the behavior of the coherence factors, only the states near the Dirac point contribute to Π_2. As always, we account for the K and K' points by an additional factor of 2. After carrying out integration over d^2k we arrive at:

$$\Pi_2(\omega, \mathbf{q}) \approx -i \frac{2q^2}{\omega} \Theta(\omega - 2E_F)\Theta(\omega - 2W). \tag{2.38}$$

Here $\Theta(x)$ is the Heaviside function, which ensures that the imaginary part is non-zero only in the particle-hole continuum region $2E_F < \omega < 2W$. The dielectric function in this region is therefore

$$\varepsilon(\omega, \mathbf{q}) = 1 - \beta_0 \frac{q}{\omega^2} + i \frac{\beta_0 \pi}{E_F} \frac{q}{\omega}, \tag{2.39}$$

which shows that the collective mode ω_{p} in the $2E_F < \omega_{\mathrm{p}} < 2W$ region has a damped square-root dispersion

$$\omega_{\mathrm{p}} \approx \sqrt{\beta_0 q} - i \frac{\pi \beta_0}{2E_F} q. \tag{2.40}$$

The imaginary part, which scales linearly with q, describes damping due to particle-hole pair production.

We finish the discussion of the collective modes by comparing the analytically predicted dispersion with the numerical result in Fig.2-1a. While the simulated dispersion closely follows the square-root dependence $\omega_{\mathrm{p}} \propto \sqrt{q}$, the agreement between the simulation and $\omega_{\mathrm{p}} = \sqrt{\beta_q q}$ dispersion is drastically improved if the two first terms β_0 and β_1 from the series expansion in Eq. (2.15) are used for a fitting. Although the terms β_0 and β_1 could in principle be computed by carrying out an expansion of the polarization function in Eq. (2.11) in powers of q and then evaluating the resulting integrals numerically, we instead treat β_0 and β_1 as free parameters and fit them to the simulated dispersion. This approach yields values

$$\begin{aligned} \beta_0 &= 0.96 \times 10^3 \text{ meV}^2 \text{ nm}, \\ \beta_1 &= -10^3 \text{ meV}^2 \text{ nm}^2. \end{aligned} \tag{2.41}$$

The best-fit β_0 value is close to $\beta_0 = 4\alpha v_F E_F \approx 0.86 \times 10^3$ meV^2 nm predicted from (2.35). We also see that, since β_1 is negative, the plasmon dispersion is indeed softened by interband polarization, in agreement with the argument given in the main text [see Eq. (14)].

2.10.3 Twisted bilayer graphene - details of the model

Here we describe in detail the model for twisted bilayer graphene (TBG) bandstructure used in the main text. We use the effective continuum Hamiltonian introduced in Ref.[60], adopting notations and numerical values used in Ref.[60].

The continuum approach is made possible by the small values of the twist angle θ by which the two graphene layers in TBG are rotated relative to one another. We start by taking two AA-stacked graphene layers and rotating the layer 1 and the layer 2 around the B-sites by $-\theta/2$ and $\theta/2$ respectively. For the "magic" value of $\theta = 1.05°$, the moiré real-space lattice constant is $L_M = a/2\sin(\theta/2) \approx 13.4$ nm. This is two orders of magnitudes greater than the graphene's lattice constant $a = 0.246$ nm, justifying the use of the continuum approach.

In momentum space this real-space rotation translates into two graphene Brillioun zones rotated by angle θ relative to each other. Both BZs are centered at the same Γ point but the K (and K') points of the two layers are separated by a small momentum $4\pi/(3L_M)$. As the moiré periodicity L_M is much greater than the lattice constant a, we can ignore the intervalley mixing between the two valleys K and K' of the original graphene layers - here labeled by $\xi = -1, 1$. The total Hamiltonian of the system becomes therefore block diagonal in the valley index. The blocks $H^{(\xi)}$ describing each of the two valleys take the form

$$H^{(\xi)} = \begin{pmatrix} H_1 & U^\dagger \\ U & H_2 \end{pmatrix} \tag{2.42}$$

in the basis of (A_1, B_1, A_2, B_2) sites. The matrices H_l $(l = 1, 2)$ correspond to the intralayer Hamiltonians of the layers. The latter, due to the lengthscale separation between L_M and a, can be approximated by performing the standard kp expansion around the points K and K'.

This procedure gives 2×2 Dirac Hamiltonians centered at the $\mathbf{K}_\xi^{(l)}$ points

$$H_l = -\hbar v \left[R\left(\pm\theta/2\right)\left(\mathbf{k} - \mathbf{K}_\xi^{(l)}\right) \right] \cdot \left(\xi\sigma_x, \sigma_y\right), \tag{2.43}$$

where $\mathbf{k}$ is a momentum in the BZ of the original graphene layers, and $R(\varphi)$ is the 2×2 rotation matrix

$$R(\varphi) = \begin{pmatrix} \cos\varphi & -\sin\varphi \\ \sin\varphi & \cos\varphi \end{pmatrix} \tag{2.44}$$

that accounts for rotation of the BZ of the original graphene layers. The signs $\pm$ in (2.43) correspond to the layers $l = 1$ and 2, respectively.

The energy scale for the Hamiltonians H_l is $\hbar v/a = 2.1354$ eV. The vectors $\mathbf{K}_1^{(l)}$, $\mathbf{K}_{-1}^{(l)}$, which denote the Dirac points K and K' of the layers, are given by

$$\mathbf{K}_\xi^{(1)} = -\xi \frac{4\pi}{3a} R(-\theta/2) \begin{pmatrix} 1 \\ 0 \end{pmatrix}, \quad \mathbf{K}_\xi^{(2)} = -\xi \frac{4\pi}{3a} R(\theta/2) \begin{pmatrix} 1 \\ 0 \end{pmatrix}, \tag{2.45}$$

respectively. We stress that, while $\mathbf{k}$ alone has length close to $\sim 4\pi/3a$, the difference $\mathbf{k} - \mathbf{K}_\xi^{(l)}$ is small, since $\mathbf{k}$ is always located near the vicinity of the $\mathbf{K}_\xi^{(l)}$ points. This makes the linear expansion from (2.43) a well defined approximation.

More quantitatively, the expressions in (2.43), found by Taylor expanding the graphene tight-binding Hamiltonian, are valid for momenta close enough to the Dirac points of the two layers, $|\mathbf{k} - \mathbf{K}_\xi^{(l)}|a \ll 1$. For $\theta \ll 1$ this condition is obeyed in the entire mini Brillouin zones of the TBG superlattice.

In the analysis below the moiré superlattice BZ is defined as in the inset of Fig.2-3, with the two reciprocal lattice vectors

$$\mathbf{G}_1^M = -\frac{2\pi}{\sqrt{3}L_M} \begin{pmatrix} 1 \\ \sqrt{3} \end{pmatrix}, \quad \mathbf{G}_2^M = \frac{4\pi}{\sqrt{3}L_M} \begin{pmatrix} 1 \\ 0 \end{pmatrix}. \tag{2.46}$$

We denote the reciprocal lattice vector length as $G_M = |\mathbf{G}_1^M| = |\mathbf{G}_2^M| = 4\pi/\sqrt{3}L_M$.

Matrix U is the effective moiré interlayer coupling given by:

$$U = \begin{pmatrix} u & u' \\ u' & u \end{pmatrix} + \begin{pmatrix} u & u'\nu^{-\xi} \\ u'\nu^{\xi} & u \end{pmatrix} e^{i\xi \mathbf{G}_1^M \cdot \mathbf{r}} + \\ + \begin{pmatrix} u & u'\nu^{\xi} \\ u'\nu^{-\xi} & u \end{pmatrix} e^{i\xi \left(\mathbf{G}_1^M + \mathbf{G}_2^M\right) \cdot \mathbf{r}}, \tag{2.47}$$

where we introduced a notation for the phase factor $\nu = e^{i2\pi/3}$. The interlayer couplings u and u' are taken as $u = 0.0797$ eV and $u' = 0.0975$ eV to match values in Ref.[60].

To determine the energy bands and the eigenstates we take the Bloch wavefunction ansatz for a valley ξ as

$$\Psi^X_{\xi,n,\mathbf{k}}(\mathbf{r}) = \sum_{\mathbf{G}} C^X_{\xi,n,\mathbf{k}}(\mathbf{G}) e^{i(\mathbf{k}+\mathbf{G})\cdot\mathbf{r}} \tag{2.48}$$

with X labeling the spinor components $X = A_1,\ B_1,\ A_2,\ B_2$. The band index, labeled by n and $\mathbf{k}$, is the Bloch wave vector in the BZ of the original graphene layers. Here $\mathbf{G}$ runs over all possible integer combinations of the reciprocal lattice vectors, $\mathbf{G} = m_1\mathbf{G}_1^M + m_2\mathbf{G}_2^M$ with integer m_1 and m_2. As discussed in Ref.[60], the low-energy states are expected to be dominated by states near the original Dirac points. We therefore take only not-too-large indices m_1 and m_2 that satisfy the condition

$$|\mathbf{k} + \mathbf{G} - \mathbf{M}_\xi| \leq z G_M \,, \tag{2.49}$$

where z is a conveniently chosen number of order one [Ref.[60] uses $z = 4$], and $\mathbf{M}_\xi$ are the "mean" Dirac point locations

$$\mathbf{M}_\xi = \frac{1}{2}\left(\mathbf{K}_\xi^{(1)} + \mathbf{K}_\xi^{(2)}\right) = -\frac{4\pi}{3a}\xi\cos(\theta/2)\begin{pmatrix} 1 \\ 0 \end{pmatrix}, \tag{2.50}$$

given by the midpoint between the K (or K') points of the two layers.

2.10.4 Electron loss function for the TBG bandstructure

Fig.2-4 details the behavior of the electron loss function for TBG, depicted in Fig.2-3 of the main text. Panels a and b show constant-momentum $\mathbf{q}$ linecuts of the real and imaginary parts of the dielectric function $\varepsilon(\omega, \mathbf{q})$. The finite width of the plasmon resonance in the loss function in Fig.2-4c is due to the infinitesimal imaginary part of $\omega + i0$ in the polarization function in Eq. (8) replaced with $\omega + i\gamma$, with a suitably chosen small γ introduced for illustration purposes.

Strong electron-electron interactions in the narrow electron bands lead to large dielectric function values, as can be seen in Fig.2-4. For energies $\hbar\omega < 2W$ the dielectric function imaginary and real parts take values a few orders of magnitude higher than those of graphene monolayer. The origin of these large values can be traced to the high effective fine structure constant (or, equivalently, low Fermi velocity) in the flat electron bands, as discussed in the main text. To see this in more detail, we recall the Thomas-Fermi expression for the long-wavelength static dielectric function of graphene[33]

$$\varepsilon(\omega = 0, \mathbf{q} \to 0) = 1 + q_{TF}/q \tag{2.51}$$

with the Thomas-Fermi momentum $q_{TF} = N\alpha k_F$, where N is the degeneracy factor $N = 8$ (2 spins, 2 layers, 2 valleys). For illustration purposes, taking a fine structure constant $\alpha \sim 30$ and Fermi momentum $k_F \sim K$, for the momentum $q \sim K/2$ (red line in the Fig.2-4) (2.51) predicts a dielectric function value $\varepsilon \sim 480$, which is in good agreement with the simulation results. Above $\hbar\omega > 2W$ the dielectric function rapidly decreases until $\hbar\omega > 20$ meV where the contributions of higher electron bands start to dominate.

At these energies, plasmon dispersion is strongly affected by the presence of higher electron bands. At small q plasmon dispersion is predominantly due to intraband transitions, and is thus insensitive to other electron bands. At large q the situation changes. In the absence of higher electron bands the zeros of the dielectric function would occur at much larger energy scales $\hbar\omega_{\mathrm{p}} \sim 40$ meV. However, as argued in Eq.

19 in the main text, higher electron bands push plasmon dispersion down with the large-q zeros of the dielectric function on the order $\hbar\omega_{\mathrm{p}} \approx \sqrt{W\Delta} \approx 6.6$ meV. Here W is the flat-band bandwidth and Δ is the band gap as defined in the main text. The independence of this value of α is the behavior to be expected for large enough α, such that plasmon dispersion extends above the p-h continuum. The independence of ω_{p} of α at $\alpha \gg 1$ is a characteristic feature of interband plasmons.

Lastly, we note that our simulation is expected to be accurate only for $\mathbf{q}$ inside the TBG Brillouin zone. When $\mathbf{q}$ approaches zone boundary it is necessary to consider local field effects[71, 72]. Although these effects are often small, they require careful examination and thus will be a subject of a future work.

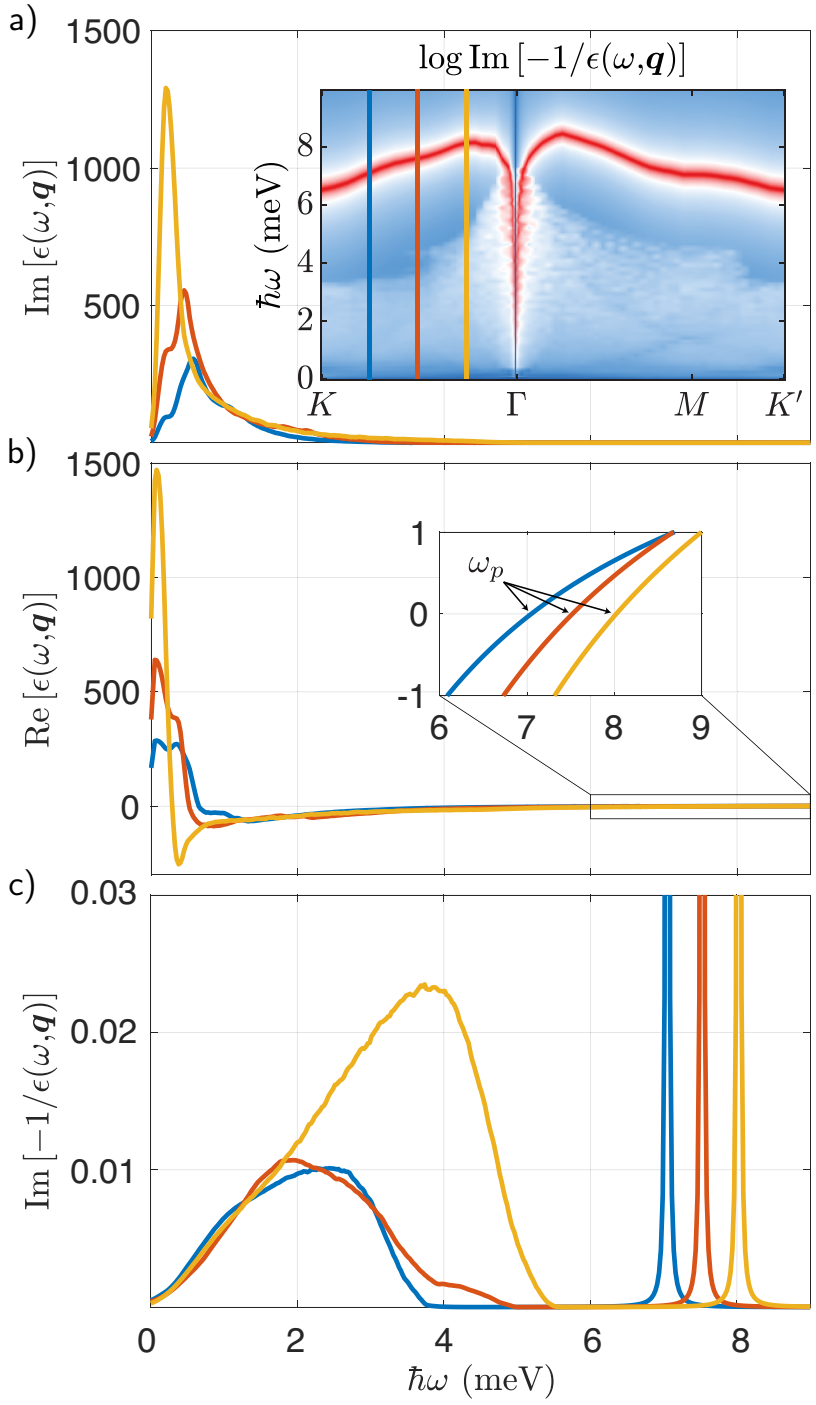

Figure 2-4: Imaginary (a) and real (b) parts of the TBG's dielectric function $\varepsilon(\omega, \mathbf{q})$ for several momenta values marked by the colored lines in the inset of (a). The zoom-in in panel (b) shows the positions of plasmon resonances found from $\varepsilon(\omega, \mathbf{q}) = 0$. The inset in (a) is a replica of the loss function shown in Fig. 2-3; higher-resolution linecuts at the selected momenta are presented in (c). The curves in (a-c) were smoothed with an equal-weighted moving filter.

Chapter 3

Robustness of the stiff dispersion in the presence of ordering

3.1 Introduction

Twisted bilayer graphene (TBG), and in general the family of moiré materials, have emerged as an ideal platform for exploring strongly interacting physics: same sample can display a record-low density superconductivity[14, 15], a Mott insulating regime[13, 56] or even an interaction-driven ferromagnetic behavior[57, 58]. In this Chapter we focus on the microscopic origins of the over-the-band modes introduced in the previous section. These modes pierce through the particle-hole continuum to emerge inside the energy gap between electron bands and become decoupled from the spectrum of electronic excitations. Such behavior is much unlike that seen in conventional materials, where plasmon's dispersion at large momenta ultimately ends inside the continuum[32, 34, 33, 53], which therefore raises multiple questions about the robustness of these over-the-band plasmon modes.

To answer these questions, we consider collective modes inside a correlated Hubbard insulator[4] and a 2D Wigner solid[79]. We find that over-the-band plasmons exist irrespective of the nature of the correlated state. This is best exemplified by the Fig.3.1 which shows a plasmon mode (bright red feature) inside an insulating regime where the gap at the Fermi level (see the inset) is opened by interactions which drive

the system towards an ordered state. While the behavior of the over-the-band modes at small momenta depends on the nature of the correlated state, for example whether the system is metallic or insulating, the large momentum behavior turns out to be robust with only the subtle details of the plasmon dispersion being sensitive to the underlying properties of the low-energy electronic excitations.

Surprisingly, the presence of the ordered state in fact helps to elucidate the microscopic mechanisms behind the over-the-band behavior rather than to obfuscate them. Specifically, in the correlated insulator regime the only electronic transitions that contribute to the behavior seen in Fig.3.1 originate from interband terms. These interband transitions, schematically depicted as blue arrows in the inset of Fig.3.1, can be thought of as strongly-coupled particle-hole excitations. Indeed, this is the same mechanism that is behind the over-the-band behavior of collective modes which we will identify in the 2D Wigner solid. In there, the over-the-band collective excitations correspond to longitudinal oscillations of electron-hole pairs strongly coupled by long-range dipole forces. This turns out to be precisely the reason for the strong dispersive character of the over-the-band modes.

3.2 Collective modes in a correlated Hubbard insulator

3.2.1 Introduction of the toy-model

We begin by analysing collective modes in a correlated Hubbard insulator. We model the TBG electron system as a narrow tight-binding band with an on-site Hubbard interaction

$$H = \sum_{\langle ii' \rangle} \sum_{\sigma} t a^{\dagger}_{i\sigma} a_{i'\sigma} + \sum_{i} \sum_{\sigma \neq \sigma'} U n_{i\sigma} n_{i\sigma'}, \tag{3.1}$$

with the interaction strength U and hopping t chosen to mimick the behavior of electrons in TBG narrow bands as discussed below. In general, the spin variables

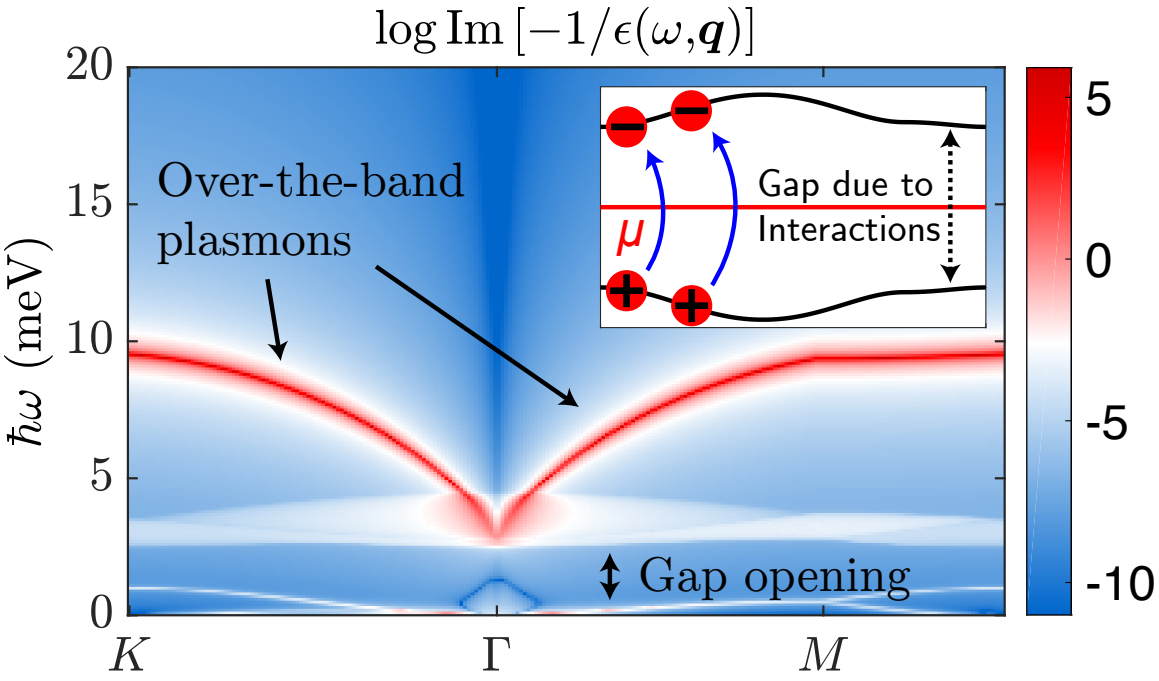

Figure 3-1: Electron loss function $\mathrm{Im}\,(-1/\varepsilon(\omega, \mathbf{q}))$ for a narrow-band toy model of a correlated Hubbard insulator. Interactions lead to a gap opening (see inset) at a Fermi level μ. Parameter values are chosen to mimic TBG bands (bandwidth $W = 3.75$ meV, lattice periodicity $L_M = 13.4$ nm, Fermi energy is placed inside the gap at $\mu = 0$ meV); log scale is used to clarify the relation between different features.

σ should account for both spin and valley degrees of freedom. Here, for illustration purposes, we suppress the valley degrees of freedom, taking spin variables to be $\sigma = \uparrow, \downarrow$. In which case the interaction term takes the usual Hubbard form $\sum_i U n_{i\uparrow} n_{i\downarrow}$. This suppression of valley degree of freedom will indirectly lead to a gap opening at a charge neutrality point of the electronic system instead of the expected TBG fillings[13, 56]. Here we use this model as a simple framework to describe order in correlated Hubbard insulator. For simplicity, we will treat hopping as nearest neighbor and take the lattice to be bipartite, with all lattice sites equivalent and, in the absence of the order, having equal on-site energies. In this case, the ordered state can be described by site occupancies that differ on the even and odd sublattices:

$$\bar{n}_{i\uparrow} = \begin{cases} \bar{n}, & \text{even sites} \\ \bar{n}', & \text{odd sites} \end{cases}, \; \bar{n}_{i\downarrow} = \begin{cases} \bar{n}', & \text{even sites} \\ \bar{n}, & \text{odd sites} \end{cases} \tag{3.2}$$

The difference in the energies between the even and odd sites for one spin polarization represents an order parameter, arising spontaneously in the ordered state

$$\Delta = u - u',\ u = Un_{i\uparrow} = Un_{i'\downarrow},\ u' = Un_{i'\uparrow} = Un_{i\downarrow} \tag{3.3}$$

(here i and i' label the even and odd sublattice sites). The quantity Δ also represents the energy gap in the ordered state.

3.2.2 Mean-field description of a correlated insulator

To describe the ordered state and to estimate Δ, we develop a mean field approximation. This is done in a standard way by writing

$$n_{i\sigma} = \bar{n}_{i\sigma} + \delta n_{i\sigma}. \tag{3.4}$$

Plugging this expression in the Hubbard interaction we expand it in fluctuations about the mean-field state:

$$\begin{aligned}
&\sum_i U n_{i\uparrow} n_{i\downarrow} = \sum_i U(\bar{n}_{i\uparrow} + \delta n_{i\uparrow})(\bar{n}_{i\downarrow} + \delta n_{i\downarrow}) \\
&= \sum_i U\bar{n}_{i\uparrow}\bar{n}_{i\downarrow} + U\delta n_{i\uparrow}\bar{n}_{i\downarrow} + U\bar{n}_{i\uparrow}\delta n_{i\downarrow} + O(\delta n^2) \\
&\approx \sum_i U\bar{n}_{i\downarrow} a^\dagger_{i\uparrow} a_{i\uparrow} + U\bar{n}_{i\uparrow} a^\dagger_{i\downarrow} a_{i\downarrow} - U\bar{n}_{i\uparrow}\bar{n}_{i\downarrow}
\end{aligned} \tag{3.5}$$

where in the last line we used the relations

$$\delta n_{i\uparrow} = a^\dagger_{i\uparrow} a_{i\uparrow} - \bar{n}_{i\uparrow}, \quad \delta n_{i\downarrow} = a^\dagger_{i\downarrow} a_{i\downarrow} - \bar{n}_{i\downarrow}. \tag{3.6}$$

Replacing the Hubbard interaction in Eq. (3.1) with the above expression yields a quadratic Hamiltonian that can be diagonalized and used to construct mean-field ordered states.

Namely, introducing local energies for the up and down spins, which take values u and u' on the two sublattices, as given in Eq.(3.3), we arrive at the Hamiltonians

for the spin-up and spin-down Bloch states:

$$H = \sum_{\sigma} \left(\sum_{\langle ii' \rangle} t a^{\dagger}_{i\sigma} a_{i'\sigma} + \sum_{i} u_i a^{\dagger}_{i\sigma} a_{i\sigma} \right) \tag{3.7}$$

Single-particle energies and eigenstates can now be described by 2×2 Bloch Hamiltonians for the bipartite lattice

$$H_{\uparrow} = \begin{pmatrix} u & f(k) \\ f(k)^* & u' \end{pmatrix}, \quad H_{\downarrow} = \begin{pmatrix} u' & f(k) \\ f(k)^* & u \end{pmatrix}, \tag{3.8}$$

where we introduced notation $f(k) = \sum_j t e^{i\mathbf{k}\mathbf{a}_j}$ (here j labels vectors pointing from a given site to nearest-neighbor sites). We will use unprimed and primed variables to label the quantities associated with each of the two sublattices. Diagonalizing these matrices yields two Bloch bands:

$$\varepsilon_{\lambda}(k) = \frac{u + u'}{2} + \lambda \sqrt{\delta u^2 + |f(k)|^2}, \quad \lambda = \pm 1, \tag{3.9}$$

where $\delta u = (u - u')/2$ and the plus/minus sign labels the conduction and valence bands.

3.2.3 Dependence of the order parameter on chemical potential

The parameter δu controls the gap between the two bands, $\Delta = 2\delta u$, and although it appears as a parameter in the toy-model Hamiltonian Eq.(3.8), its value has to be determined self-consistently at every filling density n. The equation which defines δu, Eq.(3.3), using the eigenstates and eigenvalues of the hamiltonian H, takes the form

$$\frac{1}{U} = \sum_{k} \frac{n_+(k) - n_-(k)}{\sqrt{\delta u^2 + |f(k)|^2}}, \tag{3.10}$$

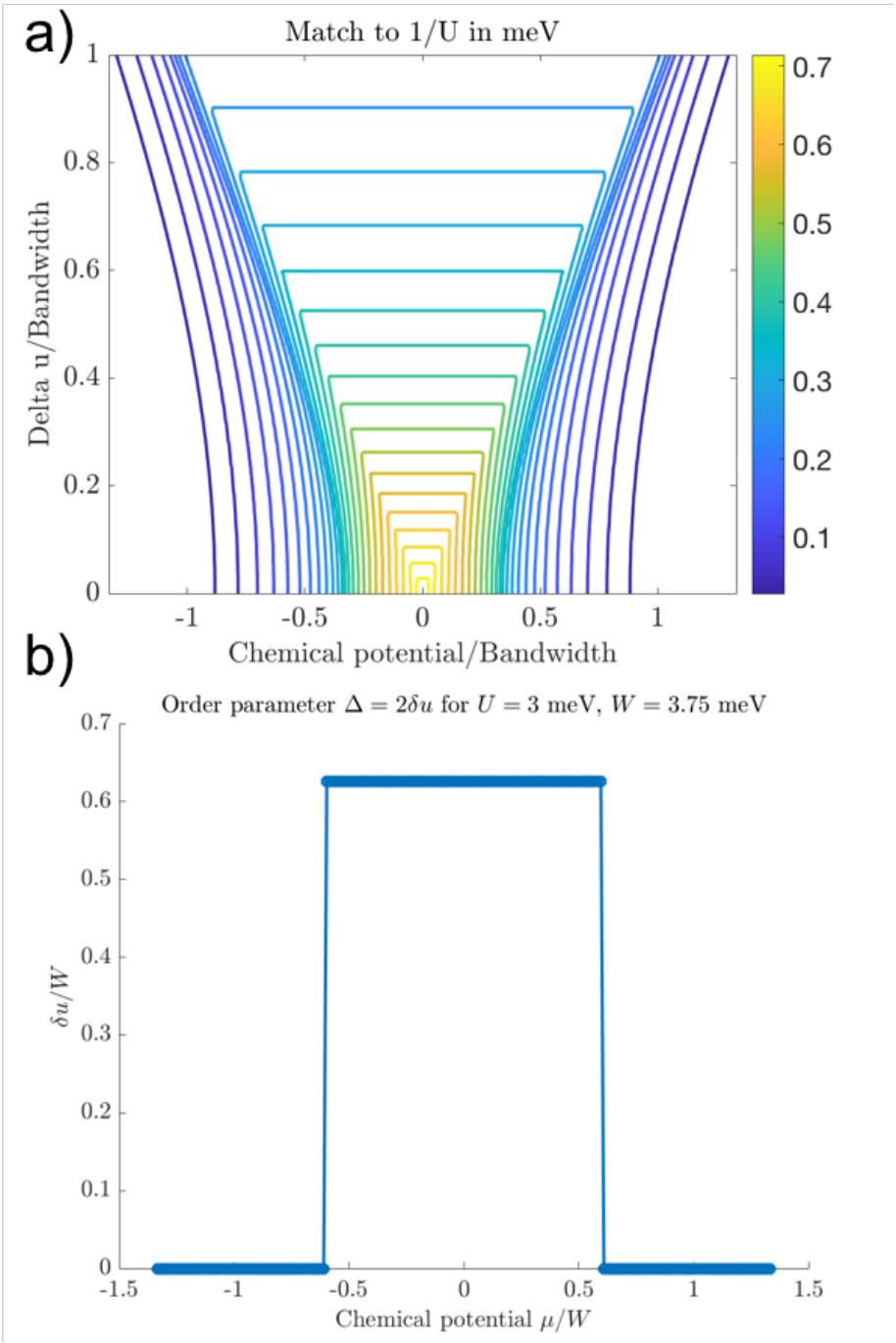

Figure 3-2: (a) Contour plots of the right-hand side of the Eq.(3.10) which constant value lines equal to $1/U$ yield the dependence of δu on chemical potential. (b) Example dependence of the order parameter δu on chemical potential μ that enters as a parameter in the Hamiltonian Eq.(3.8).

where $n_{\pm}(k)$ corresponds to an Fermi-Dirac distribution function evaluated with either the conduction $(+)$ or valence $(-)$ band dispersion from Eq.(3.9). In what follows we

solve this integral equation self-consistently, see Fig.3.2.2, to yield a dependence of δu as a function of filling n (or chemical potential μ) which is then used for the analysis of collective modes. As expected from an order parameter, δu vanishes everywhere away from the critical filling but at the critical filling it becomes non-zero.

3.2.4 Relation of the toy-model to TBG's bandstructure

Next, we discuss the bandstructure details of the model used in the above analysis. We use a hexagonal-lattice tight binding model which possesses the same symmetry and the same number of subbands as the flat bands in TBG. We match the energy and length scales by choosing the width of a single band W and the hexagonal lattice period L_M identical to the parameters in TBG: $W = 3.75$ meV and $L_M = a/2\sin(\theta/2)$ is the moiré superlattice periodicity. For the magic angle value $\theta = 1.05^\circ$, using carbon spacing $a = 0.246$ nm, this gives $L_M = 13.4$ nm. The hopping element t and nearest neighbours $\mathbf{a}_j$ in the function $f(k)$ in the above Hamiltonian are therefore equal to $t = W/3$ and $\mathbf{a}_j = (\cos(2\pi j/3), \sin(2\pi j/3))L_M/\sqrt{3}$, $j = 0, 1, 2$. The tight-binding model used here is precisely the same one that was employed in the Chapter 2 when discussing the kinematic origins of the over-the-band modes.

3.2.5 Determination of collective modes

We proceed now to find plasmon excitations of this electronic system. Dispersion of collective excitations is given by the nodes of the dynamical dielectric function

$$\varepsilon(\omega, \mathbf{q}) = 1 - V(\mathbf{q})\Pi(\omega, \mathbf{q})\,. \tag{3.11}$$

Here $V_{\mathbf{q}} = 2\pi e^2/\kappa q$ is the Coulomb interaction in a medium with a background dielectric constant κ and $\Pi(\omega, \mathbf{q})$ is the electron polarization function. We approximate the polarization function with the RPA expression[4]

$$\Pi(\omega, \mathbf{q}) = 2\sum_{\mathbf{k},s,s'} \frac{(f_{s,\mathbf{k}+\mathbf{q}} - f_{s',\mathbf{k}})F^{ss'}_{\mathbf{k}+\mathbf{q},\mathbf{k}}}{\varepsilon_{s,\mathbf{k}+\mathbf{q}} - \varepsilon_{s',\mathbf{k}} - \omega - i0}. \tag{3.12}$$

Here summation $\sum_{\mathbf{k}}$ denotes integration over the Brillouin zone (BZ), the composite indices $s = (\lambda, \sigma), s' = (\lambda', \sigma')$ run over the electron bands $\lambda = \pm$ and spins $\sigma = \uparrow, \downarrow$. The additional factor of 2 in front of the summation accounts for the valley degeneracy of the toy model. Here $f_{s,\mathbf{k}}$ is the Fermi-Dirac equilibrium distribution, and $F^{ss'}_{\mathbf{k+q},\mathbf{k}}$ describes band overlap factors

$$F^{ss'}_{\mathbf{k+q},\mathbf{k}} = |\langle \Psi_{s,\mathbf{k+q}} | \Psi_{s',\mathbf{k}} \rangle|^2. \tag{3.13}$$

To proceed further analytically, we first rewrite (3.12) by performing a standard replacement $\mathbf{k} + \mathbf{q} \to -\mathbf{k}$ in the term containing $f_{s,\mathbf{k+q}}$ followed by $-\mathbf{k} - \mathbf{q}, -\mathbf{k} \to \mathbf{k} + \mathbf{q}, \mathbf{k}$ justified by the $\mathbf{k} \to -\mathbf{k}$ time-reversal symmetry. This gives

$$\Pi(\omega, \mathbf{q}) = 4 \sum_{\mathbf{k},s,s'} f_{s',\mathbf{k}} \frac{F^{ss'}_{\mathbf{k},\mathbf{k+q}} (\varepsilon_{s',\mathbf{k}} - \varepsilon_{s,\mathbf{k+q}})}{(\varepsilon_{s,\mathbf{k+q}} - \varepsilon_{s',\mathbf{k}})^2 - (\omega + i0)^2}. \tag{3.14}$$

The behavior of this expression at small $\mathbf{q}$, which will be of interest for us, can be found in a closed form.

To understand the effect correlated state has on the plasmon dispersion, it is necessary to evaluate the polarization function in both the metallic regime where $\delta u = 0$, and the correlated regime where $\delta u \neq 0$ and the chemical potential is inside the interaction-driven gap. The sum over the band indices s, s' in the polarization function from Eq. (3.14) consists of two types of terms: those corresponding to intraband transitions $s = s'$, labelled as Π^1, and those corresponding to interband transitions $s = -s'$, labelled as Π^2. When the system is in a correlated state and the chemical potential is inside the gap, then the only contribution to the polarization function comes from interband transitions. In a metallic regime both interband and intraband transitions contribute to the polarization function with the interband contributions becoming more relevant the closer chemical potential is to the edge of the other band.

We focus first on the insulating regime as it best demonstrates the physics driving the behavior of over-the-band plasmons. When the system is correlated the chemical potential μ lies inside the gap, c.f. the inset of Fig.3.1 and Fig.3.2.2b. This translates

to a condition

$$f_{(-,\sigma),\mathbf{k}} = 1\,, \quad f_{(+,\sigma),\mathbf{k}} = 0 \tag{3.15}$$

on the Fermi-Dirac distribution functions which allows us to further simplify the polarization function from Eq.(3.14). Therefore the polarization function contains only interband terms which gives an expression

$$\Pi(\omega, \mathbf{q}) = 4 \sum_{\mathbf{k},\sigma} \frac{F^{(-,\sigma)(+,\sigma)}_{\mathbf{k},\mathbf{k}+\mathbf{q}} (\varepsilon_{(-,\sigma),\mathbf{k}} - \varepsilon_{(+,\sigma),\mathbf{k}+\mathbf{q}})}{(\varepsilon_{+,\sigma),\mathbf{k}+\mathbf{q}} - \varepsilon_{(-,\sigma),\mathbf{k}})^2 - (\omega + i0)^2}\,, \tag{3.16}$$

where we used the additional simplification that the Bloch wavefunctions for different spins are orthogonal to each other. The ω frequency regime relevant for the over-the-band behavior is that of a plasmon mode extending above the typical energy scale of electronic excitations. In the strongly interacting system such as the TBG, δu, can in principle be as large as the non-interacting system's bandwidth W. For simplicity of the analysis we can assume however that $\delta u \ll W$ and verify later on numerically that the qualitative behavior is not altered outside of this regime. The characteristic energy of interband transitions is therefore on the scale of the bandwidth W. In this limit the polarization function can therefore be expanded by treating ω as the largest energy scale to yield

$$\Pi(\omega, \mathbf{q}) \approx -\frac{4}{\omega^2} \sum_{\mathbf{k},\sigma} F^{(-,\sigma)(+,\sigma)}_{\mathbf{k},\mathbf{k}+\mathbf{q}} (\varepsilon_{(-,\sigma),\mathbf{k}} - \varepsilon_{(+,\sigma),\mathbf{k}+\mathbf{q}}). \tag{3.17}$$

In the narrow-band materials the Fermi momentum k_F is on the order of the reciprocal lattice vector and the over-the-band behavior is present at a range of momenta, see Fig.3.1. We can therefore expand all expression in the long-wavelength limit of $q \ll k_F$. To leading order in momentum q the band overlap factors therefore become

$$F^{(-,\sigma)(+,\sigma)}_{\mathbf{k},\mathbf{k}+\mathbf{q}} \approx \frac{1}{4} \sin^2\theta \frac{q^2}{k^2} + \frac{1}{4} \frac{\delta u^2}{v_F^2 k^2} \cos 2\theta \frac{q^2}{k^2} \tag{3.18}$$

where we approximated the non-interacting tight binding $|f(k)|^2 = v_F^2 k^2$ as a Dirac cone and introduced an angle θ between $\mathbf{k}$ and $\mathbf{q}$. We see that in the limit of $\delta u \to 0$

it reduces to the massless graphene result. The energy difference to leading order in q becomes

$$\varepsilon_{(-1,\sigma),\mathbf{k}} - \varepsilon_{(1,\sigma),\mathbf{k}+\mathbf{q}} \approx -2\sqrt{\delta u^2 + v_F^2 k^2}\,. \tag{3.19}$$

which when compined with the expression for the band overlap factors gives a polarization function

$$\Pi^2(\omega, \mathbf{q}) \approx \frac{2}{\pi} W \frac{q^2}{\omega^2} - \frac{2}{\pi}\frac{\delta u^2}{W}\frac{q^2}{\omega^2}\,. \tag{3.20}$$

The above polarisation function translates to a plasmon dispersion

$$\omega_p \approx \sqrt{4\alpha W\left(1 - \frac{\delta u^2}{W^2}\right) v_F q} \quad \text{for} \quad \omega_p \gg W \tag{3.21}$$

which shows that the contribution of the Mott gap δu is to soften the plasmon dispersion. This behavior is to be expected as a gap between bands, here the Mott gap δu, reduces the Bloch wavefunction overlap. Most crucially however, as we will see later, presence of a correlated state also makes the dispersion independent of the chemical potential. The latter observation is to be expected as the chemical potential is inside the Mott gap and hence plasmons simply originate from transitions from a fully filled to a fully empty band. These interband plasmons are precisely the source of the over-the-band behavior seen in Fig.3.1.

We now focus on the other limit of $\delta u = 0$ which translates to a normal system in the absence of the correlated state. The polarization function for such a system consists now of two terms that account for interband and intraband transitions. The polarization function due to intraband transitions has the simple form of[4]

$$\Pi^1(\omega, \mathbf{q}) \approx \frac{n}{m}\frac{q^2}{\omega^2} \approx \frac{2}{\pi} E_F \frac{q^2}{\omega^2}\,, \tag{3.22}$$

where n is the charge density that gives rise to intraband plasmons and $m = k_F/v_F$ is the electron mass. The charge density n denotes the concentration of the minority carriers in a band, either electrons or holes, as a fully empty or a fully filled band

does not give rise to longitudinal charge oscillations. We denote the chemical potential corresponding to the van Hove critical point (for both positive and negative filling) as μ_{VH} (see Fig.3-3a) to give

$$E_F = \begin{cases} |\mu| & \text{for } |\mu| < |\mu_{VH}|\,, \\ W - |\mu| & \text{for } |\mu| > |\mu_{VH}|\,, \end{cases}$$

for the parameter E_F dependence.

As argued above the microscopic origins behind the over-the-band modes stem from interband transitions. What controls the scale of these transitions is the Bloch wavefunction overlap Eq.(3.13), which is suppressed far from the bandstructure edges. As the chemical potential comes closer to the edge of the bandstructure near $\mu = 0$, the impact of the interband transitions on the polarization function becomes maximal. An expression that captures this behavior can be derived as

$$\Pi^2(\omega, \mathbf{q}) \approx \frac{2}{\pi}(W - |\mu|)\frac{q^2}{\omega^2}\,. \tag{3.23}$$

Note how the Eq.(3.20) can be obtained from Eq.(3.23) by setting $\delta u = 0$ and placing the chemical potential $\mu = 0$ at the band crossing point.

Stiffness of the plasmon dispersion carriers information about the underlying electron transitions that give rise to the collective modes. Far from the other bandstructure edge, shaded blue region in the Fig.3-3a, for $|\mu| > |\mu_{VH}|$, we expect the total polarization function to be dependent on the chemical potential μ. Near the bandstructure crossing, shaded yellow region in the Fig.3-3a, for $|\mu| < |\mu_{VH}|$ we expect interband and intraband contributions to the polarization function to combine and, due to the form of Eq.(3.22) and Eq.(3.23), to lead to a cancellation of the dependence on the chemical potential. Plasmon dispersion ω_p therefore should follow, in a system without a Mott gap,

$$\omega_p(\mathbf{q}) = \begin{cases} \sqrt{8\alpha(W - |\mu|)v_F q} & \text{for } |\mu| > |\mu_{VH}|\,, \\ \sqrt{4\alpha W v_F q} & \text{for } |\mu| < |\mu_{VH}|\,. \end{cases}$$

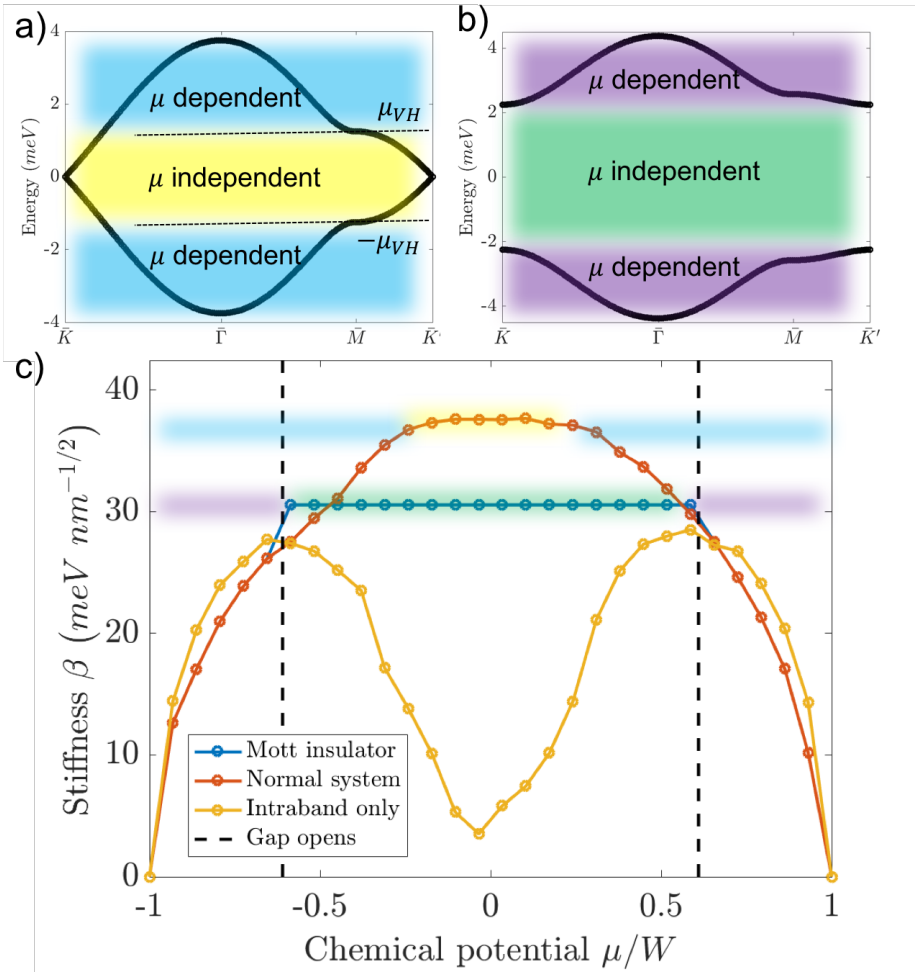

Figure 3-3: (a) Bandstructure of a normal system and its van-Hove singularity (μ_{VH}). The color shaded regions correspondong to chemical dependent or independent stiffness β, Eq.(3.2.5). (b) A bandstructure in a correlated state. A Mott gap opens a gap in the bandstructure leading to a μ independent stiffness β. (c) Dependence of stiffness β on chemical potential in a normal system, with (red line) and without (yellow line) interband transitions, and in a correlated regime (blue line). Interband transitions are behind the saturating over-the-roof behavior of plasmons in TBG. Both normal and correlated system's plasmon stiffness has regions of μ-independent plasmon stiffness (see main text).

This independence of the plasmon stiffness β, defined as $\omega_p = \beta\sqrt{q}$, on the chemical potential is a hallmark behavior of interband plasmons that are behind the over-the-band modes. This contribution of interband transitions to the plasmon stiffness β in a normal system is shown in Fig.3-3c where we plot a stiffness due to both interband and intraband transitions (red line) and due to only intraband transitions (yellow

line). As expected from Eq.(3.22) plasmon stiffness vanishes near the bandstructure edges.

Collective modes in a correlated Hubbard insulator similarly exhibit no dependence on chemical potential in the plasmon stiffness. This is shown as a blue line in Fig.3-3c. As argued in Eq.(3.21) in a correlated state plasmon dispersion has no dependence on chemical potential just as the mode in the metallic state. Here however this lack of dependence on chemical potential arises simply because plasmons originate only from interband transitions as the chemical potential lies inside the gap, the green shaded region in Fig.3-3b. The effect of the ordered state is to soften plasmon dispersion as visible on the Fig.3-3c and given by Eq.(3.21).

3.2.6 Local probe of a correlations

The chemical potential-independent plasmon stiffness in both normal and correlated Hubbard insulator has two different underlying microscopic mechanisms. One occurs due purely to inter- and intraband transition kinematics while the other is simply a property of a gap opening. It is however precisely due to the difference in these two mechanisms, and the fact that under experimental conditions the tunable parameter is charge density rather than the chemical potential, that the experimental presentation of this effect would manifest in two qualitatively different ways. In a metallic system varying chemical potential or charge density is interchangeble. We thus expect the same behavior, as that seen in Fig.3-3b (red curve), to also occur as a function of charge density. In a correlated insulator the relation between chemical potential and filling is more complicated. An interaction-driven insulating behavior which spans a whole sample occurs only precisely at the integer filling, in this model corresponding to $\mu = 0$. Yet, according to the calculation shown in Fig.3.2.2b, a gap can open far from the $\mu = 0$ value. This is because as chemical potential is brought closer to $\mu = 0$, then correlated domains of increasing spatial size are formed giving rise to a gap opening in that correlated region. Collective modes are therefore sensitive to the local Hamiltonian, i.e. whether it has a gap or not, provided that the wavelength of the plasmon is smaller than the correlation length. In a near-field optical microscopy

measurement[49, 50] a moving tip at various positions of a sample and global chemical potential could therefore be used as a probe of whether a sample region possesses a gap for an expected metallic filling - a hallmark behavior of a correlated insulator.

3.3 Collective modes in a Wigner solid

The analysis in the previous section approaches the problem of determining collective modes from the perspective of nearly-free particles - specifically it approximates the polarization function with the random phase approximation[4]. To demonstrate validity of the conclusions of this approach, and in the process gain further insight into the over-the-band behavior of the two-dimensional plasmon modes, we consider here the opposite regime: we assume interactions are so strong that the electronic system becomes a Wigner solid. Plasmons of this system are then the vibrational modes it admits [84, 85, 86, 87].

3.3.1 Introduction of a model

We model the dynamics of a Wigner solid as a harmonic problem posed for displacements of charges relative to their equilibrium positions, see Fig.3-4a. Charges displaced from equilibrium positions give rise to electric dipoles that couple to each other. To that end, we consider harmonic oscillators arranged in a 2D square lattice L, see Fig.3-4b, with long-range couplings of the form

$$\begin{aligned} H &= \sum_{\mathbf{r}} \frac{\mathbf{p}_{\mathbf{r}}^2}{2m} + \frac{m\omega_0^2}{2}\mathbf{q}_{\mathbf{r}}^2 + \frac{1}{2}\sum_{\mathbf{r},\mathbf{r}'} W_{ij}(\mathbf{r}-\mathbf{r}')q_{\mathbf{r},i}q_{\mathbf{r}',j}, \\ W_{ij}(\mathbf{x}-\mathbf{x}') &= \frac{\partial^2}{\partial x_i \partial x'_j}\frac{e^2}{|\mathbf{x}-\mathbf{x}'|}, \end{aligned} \tag{3.24}$$

where $\mathbf{r}$ and $\mathbf{r}'$ are lattice points in L; $\mathbf{p}_{\mathbf{r}}$ and $\mathbf{q}_{\mathbf{r}}$ are momenta and displacements of the oscillators. The quantity $W_{ij}(\mathbf{r}-\mathbf{r}')$ is the dipole interaction between the oscillators. Since we are interested in the over-the-band behavior of collective modes which defining feature is that collective mode's dispersion is much larger than the

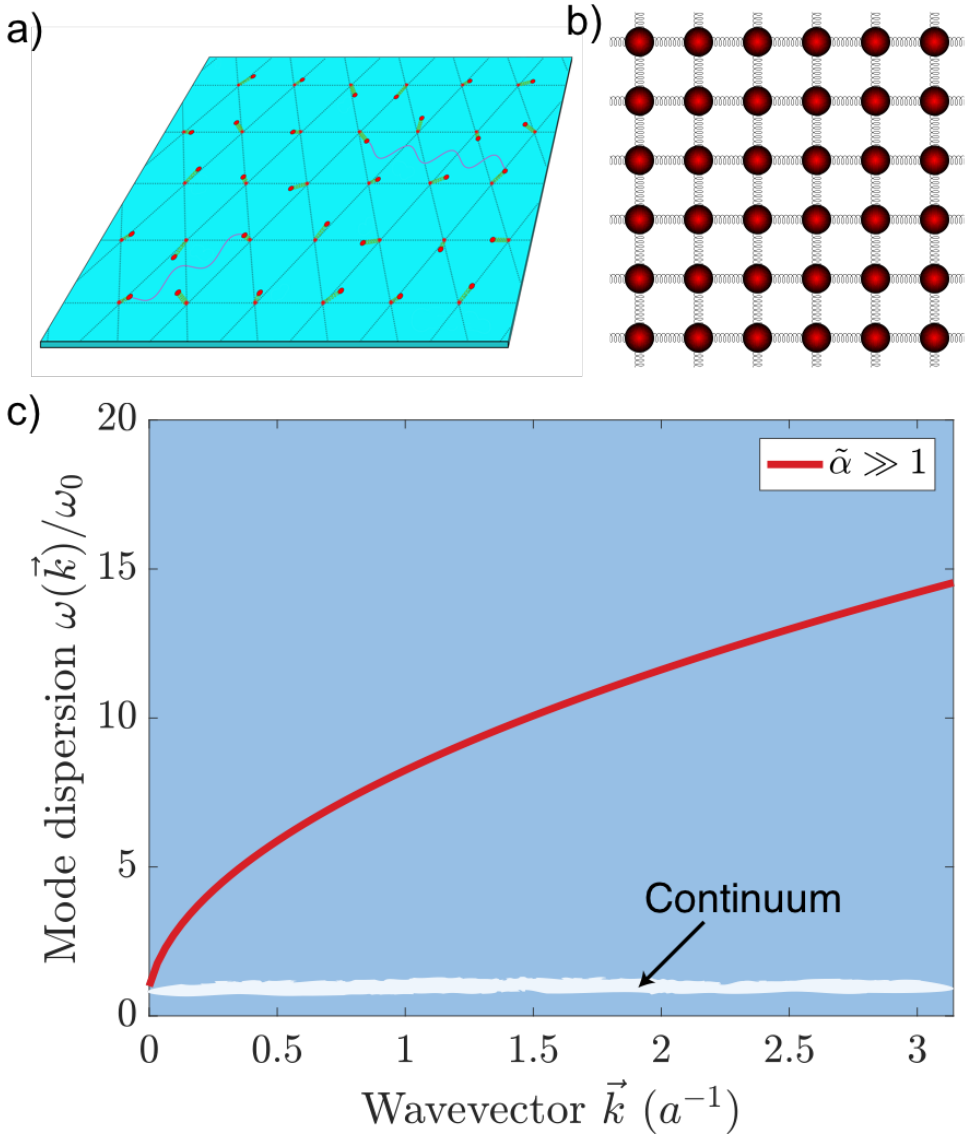

Figure 3-4: (a) Electrons in a strongly-interacting system can form a rigid lattice - the Wigner solid. Electron oscillations about the equilibrium positions give rise to electric dipoles that become strongly coupled. Figure taken from Ref.[88]. (b) We approximate the Wigner solid as a lattice of harmonic oscillators strongly coupled by dipole-dipole interactions. (c) Dispersion of longitudinal (red) and transverse (white) collective modes of the Hamiltonian from Eq.(3.26). The stiff mode corresponding to longitudinal oscillations exhibits the over-the-band behavior see in Fig.3.1.

excitation energy of the underlying particles that comprise it we can assume here an "Einstein" phonon model - we set all oscillator to have the same frequency ω_0. Fourier transforming the Hamiltonian H decouples the modes with different wavevectors,

giving a sum of 2×2 Hamiltonians, one for each $\mathbf{k}$ value:

$$H = \sum_{\mathbf{k}} \frac{1}{2m} \mathbf{p}_{-\mathbf{k}} \mathbf{p}_{\mathbf{k}} + D_{ij}(\mathbf{k}) q_{-\mathbf{k},i} q_{\mathbf{k},j} \tag{3.25}$$

$$D_{ij}(\mathbf{k}) = \frac{m\omega_0^2}{2} \delta_{ij} + \frac{1}{u} \sum_{\mathbf{g} \in L'} W_{ij}(\mathbf{k} + \mathbf{g}) - W_{ij}(\mathbf{g}) \,. \tag{3.26}$$

In the above $\mathbf{k}$ are Bloch vectors of the modes, $\mathbf{g}$ are vectors in the reciprocal lattice L'; u is the 2D area of the unit cell in the lattice L and it is equal to the inverse density of the oscillators $u = a^2 = 1/n$ with a being the lattice L periodicity.

3.3.2 Collective modes of the Wigner solid

Diagonalizing the Hamiltonian Eq.(3.26) yields two modes, one soft and one stiff. These modes are gapped near zero momentum - a consequence of the Einstein model. At long-wavelengths $ka \ll 1$ the stiff mode disperses as

$$\omega^2 = \omega_0^2 + \frac{2\pi n e^2}{m} k \tag{3.27}$$

whereas the soft mode is weakly dispersing, $\omega(\mathbf{k}) \sim \omega_0$. Both modes are shown in Fig.3-4c with the stiff mode, indicated as a red line, corresponding to the over-the-band plasmon of Fig. 3.1 and the weakly dispersing mode, shown as a white region, mimicking the particle-hole excitation continuum.

The weakly dispersing mode forms a narrow band. Physically, it describes transverse oscillations in which displacements of different oscillators are nearly perpendicular to the wavevector $\mathbf{k}$ (at $ka \ll 1$). In this band, displacements of different oscillators are not coupled by the long-range dipole forces, which explains its weak dispersion with energy set only by the oscillation frequency of individual harmonic oscillators. We note that the transverse mode here shows no dependence on the wavevector $\mathbf{k}$ as a consequence of the assumption $ka \ll 1$ which allows to neglect contribution of the states coupled by the reciprocal lattice vector $\mathbf{g}$ in Eq.(3.26). When this approximation is relaxed, then the transverse mode has a linear, sound-like, dispersion that

depends on the specifics of the crystalline order [84, 85, 86, 87].

The stiff band, on the other hand, describes longitudinal oscillations in which displacements of different oscillators are parallel to the wavevector $\mathbf{k}$ (at $ka \ll 1$). In this band, unlike the weakly dispersing modes, displacements of different oscillators are strongly coupled by the long-range dipole forces leading to its strong dispersive character.

3.3.3 Relation to TBG parameters

To understand the separation of energy scales between the longitudinal and transverse modes of the Wigner solid, it is necessary to quantify strength of interactions in this system. A dimensionless quantity which accomplishes just that is a ratio of the dipole potential energy to the kinetic energy of the dipoles

$$\tilde{\alpha} = \frac{2\pi e^2}{m\omega_0^2 a^3}\,, \tag{3.28}$$

which conceptually is precisely the same quantity as the effective fine structure constant α from the previous section. This analogy between α and $\tilde{\alpha}$ however runs deeper. We can construct an effective Fermi velocity v_F and through it define the "Fermi energy" for this model:

$$v_F \approx \omega_0 a\,, \quad E_F \approx \frac{1}{2} m v_F^2 \tag{3.29}$$

Finally, as noted before, by realising that in a narrow-band system Fermi momentum k_F is on the order of the reciprocal lattice spacing $k_F \approx \pi/a$ shows that in fact $\tilde{\alpha}$ and the effective fine structure constant α are the same two quantities. This becomes particularly evident when we rewrite the dispersion of the stiff mode as

$$\begin{aligned} \omega^2 &= \omega_0^2 + \frac{2\pi e^2}{ma^3} ka = \omega_0^2 + \tilde{\alpha}\omega_0^2 ka \\ &\approx \tilde{\alpha}\omega_0 v_F k\,, \quad \tilde{\alpha} \gg 1 \end{aligned} \tag{3.30}$$

which is precisely of the form discussed in the previous section.

3.3.4 Why does RPA capture the strongly-interacting physics?

Both the collective modes of the Wigner solid, Fig.3-3c, and the plasmons of the narrow-electron band system obtained through a free-particle approximation, Fig.3.1, manifest the over-the-band behavior. This surprising conclusion that a method targeted at a weakly interacting system agrees with results of, essentially, a non-perturbative analysis of a strongly interacting model can be ultimately traced back to the microscopic origins of the over-the-band behavior: strongly coupled electron-hole pairs. In the context of the RPA analysis these can be identified as interband transitions while in the Wigner solid case they correspond to longitudinal oscillations of electrons that form an electric dipole. In both cases the system can be described as a lattice of harmonic oscillators and, therefore, the RPA approximation, that in its roots relies on a harmonic description of collective electron oscillations[89, 2, 3], agrees with the harmonic analysis of a Wigner solid from Eq.(3.26).

3.4 Conclusion

Collective oscillations of narrow-band materials exhibit a striking over-the-band behavior which decouples them from the spectrum of underlying single-particle excitation energies. The origins of this separation of energy scales can be traced back to a strong Coulomb coupling of electron-hole pairs in these systems. By analysing collective modes of an analytically solvable strongly interacting system - a Wigner solid - we confirmed validity of the conclusions of a free-particle approximation. The origins of this surprising agreement rely on the accuracy of the harmonic description of collective excitations inherent in the RPA approach.

While the over-the-band behavior is a universal feature present in all narrow-band materials, the subtle details of the dispersion of the collective modes are dependent on the nature of the correlated state. Correlated behavior leading to an interaction-driven band gap opening softens the dispersion of collective modes. This softening of

the dispersion as a function of a filling number (or a local chemical potential) can be used in near-field optical microscopy measurements as a local probe of a correlated state.

Chapter 4

Plasmonic nonreciprocity driven by band hybridization in moiré materials

4.1 Introduction

Time-reversal symmetry (TRS) breaking leads to the emergence of unidirectional modes, such as the chiral edge states of the quantum Hall effect [90, 91, 92], the quantum anomalous Hall effect [93, 94, 95, 96, 97], or the topological photonic crystals [98, 99, 100, 101, 102]. However, such modes, while holding exceptional promise for development of new devices, often require specific experimental conditions, such as strong magnetic fields, significant magnetic doping or a large macroscopic size of a device. This means that they are not easily susceptible to miniaturization necessary for the technological applications, which usually benefit from the on-chip integration on a nanoscale or they cannot be easily coupled to electromagnetic radiation and hence providing greater experimental utility.

For these reasons, one of the alternative platforms in which nonreciprocity is a highly sought-after property are the 2D surface plasmons [103, 104, 105, 106, 107, 108, 109, 110, 111, 112, 113, 114, 115], collective modes of oscillating charge density, that are of fundamental importance to controlling light-matter interactions [11, 6, 137]. These quasiparticles can be easily excited using electromagnetic radiation and are an essential ingredient in developing optoelectronic devices. An example of a plasmon

dispersion relation with a TRS preserved is presented in Fig.4-1(a). While a nonreciprocity in the plasmon dispersion, $\omega_p(\mathbf{q}) \neq \omega_p(-\mathbf{q})$, can be induced using magnetic field [116, 117, 118, 119], the 2D plasmon platform allows for an appealing alternative based on driving electric current through the devices - the so-called plasmonic Doppler effect [120, 111, 114, 115, 113, 112]. The essence of this phenomenon boils down to a simple Galilean transformation that distinguishes plasmons moving along and against the electric current. Electron flow modifies the plasmon dispersion with a correction, $\Delta\omega_p^{(c)} \sim \mathbf{u}\cdot\mathbf{q}$, proportional to the drift velocity $\mathbf{u}$ and plasmon momentum $\mathbf{q}$. This current-induced nonreciprocity $\Delta\omega_p^{(c)}$ of the plasmon dispersion is the conventional plasmonic Doppler effect.

Unfortunately, even in pristine 2D graphene samples, the drift velocity is a small fraction of the Fermi velocity [121, 122] and hence the relative magnitude of the Doppler effect [111]

$$\frac{\Delta\omega_{\rm p}^{(c)}(\mathbf{q})}{\omega_p^0(\mathbf{q})} \sim \frac{1}{\alpha}\frac{u}{v_F}\frac{\omega_p^0(\mathbf{q})}{|\mu|}, \quad \omega_p^0(\mathbf{q}) = \sqrt{4\alpha|\mu|v_F q} \tag{4.1}$$

is a small correction on the order of $\sim 3\%$ to the graphene plasmon dispersion in the absence of electron drift, $\omega_p^0(\mathbf{q})$ [33, 34, 9]. Here v_F and $|\mu|$ are the Fermi velocity and Fermi energy, respectively. The parameter $\alpha = e^2/\hbar\kappa v_F$ characterizes the strength of the electronic interactions in a dielectric medium with a relative permittivity κ. The presence of the parameter α in the drift-free part of the plasmon dispersion $\omega_p^0(\mathbf{q})$ leads to a property $\omega_p^0(\mathbf{q}) < |\mu|$ in realistic 2D material scenarios with $\alpha \lesssim 1$, and thus is an additional limitation in attempts to observe the conventional Doppler effect.

Here we show that the materials with strongly hybridized, narrow electron bands characterized by $\alpha \gg 1$, can host another, fundamentally quantum in nature, source of plasmonic nonreciprocity. This effect results in an asymmetry of the plasmon dispersion (as demonstrated in Fig.4-1b), which is strongly enhanced by an additional factor of α:

$$\Delta\omega_{\rm p}^{(q)}(\mathbf{q}) \sim \alpha\frac{\Delta_h^2 v_F q}{|\mu|^3}\mathbf{u}\cdot\mathbf{q}\,, \quad \frac{\Delta\omega_{\rm p}^{(q)}(\mathbf{q})}{\omega_p^0(\mathbf{q})} \sim \frac{u}{v_F}\frac{\Delta_h^2\omega_p^0(\mathbf{q})}{|\mu|^3}\frac{q}{k_F}\,. \tag{4.2}$$

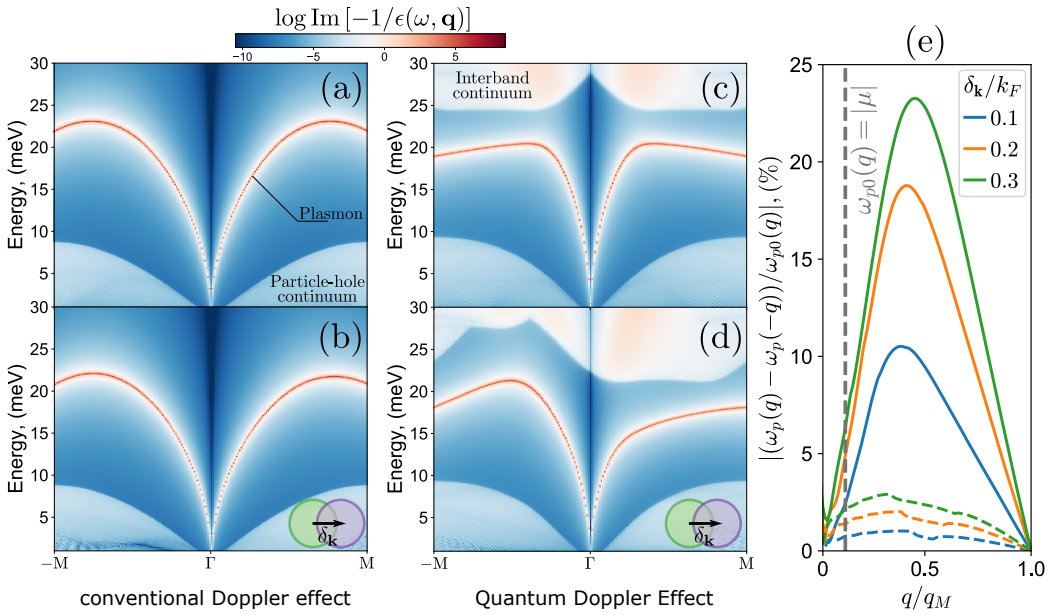

Figure 4-1: a, b) Electron loss function of a unhybridized narrow-band toy-model (a) without and (b) with applied electric current at zero temperature. The conventional Doppler effect imposes only a small change on the plasmon dispersion. c, d) Electron loss function of a hybridized narrow-band toy-model (c) without and (d) with applied electric current at zero temperature. Current flow leads to a TRS breaking and induces a nonreciprocity (asymmetry) in the plasmons' dispersion between positive and negative momenta. e) A comparison of relative asymmetry between positive and negative momenta at several electron flow values (blue, orange, green). Here $\delta_{\mathbf{k}}$ is an electric-field-driven momentum shift of the Fermi surface. The dashed lines correspond to a conventional Doppler effect present in any system, Eq.(4.1). When bands become narrow and hybridized, strong asymmetry develops (the "Quantum Doppler effect", solid line), which origin is purely a consequence of a non-vanishing interband wavefunction overlap. The dielectric function plots (a-d) are obtained by numerically evaluating the polarization function from Eq.(4.8) using a tight-binding model described in the Methods section.

Here Δ_h is the strength of hybridization between the two bands that opens up a gap between them (see Fig.4-2a). This linear dependence on α gives rise to a relative frequency shift that is amplified by the fine structure factor α unlike the conventional Doppler effect $\Delta\omega_{\mathrm{p}}^{(c)}(\mathbf{q})$. The origin of this additional source of plasmonic nonreciprocity can be traced back to the electron bandstructure where individual bands are hybridized with one another. This is in stark contrast to the conventional plasmon Doppler effect, as discussed previously, where the microscopic origins of the nonreciprocity can be ultimately understood simply through a shift of the reference frame,

largely independent of the material parameters [120, 114]. A comparison of these two sources of nonreciprocity is shown in Fig.4-1(c) for a narrow-electron band system with $\alpha \gg 1$ in the cases with and without band hybridization. As soon as the plasmon frequencies reach above the chemical potential $\omega_p(\mathbf{q}) \gtrsim |\mu|$, a plasmon regime guaranteed by the presence of strong interactions $\alpha \gg 1$ [138], the quantum correction to the Doppler effect dominates over the conventional Doppler effect leading to a strong enhancement of plasmonic nonreciprocity.

While this additional source of bandstructure-driven nonreciprocity is a general consequence of the band hybridization, a necessary ingredient which ensures a drastic increase in the magnitude of the effect is the presence of strong electron-electron interactions $\alpha \gg 1$. A natural material realizations which possess these attributes are the moiré materials, such as the twisted bilayer graphene (TBG) [13, 14, 15] and the ABC stacked trilayer graphene (TLG) [17] where $\alpha \sim 10-30$, in contrast to the monolayer graphene where $\alpha \sim 1$. This enhancment of electron-electron interaction effects is due to the emergence of a superlattice with a long lattice constant that is much larger than the atomic spacing of the original crystal. Such a long period in real space results in a small Brillouin zone in the reciprocal space that gives rise to a set of extremely narrow minibands with bandwidths on the order of tens of millielectron volts [54, 139]. Due to this feature, materials such as TBG and TLG are in many ways an ideal realization of a strongly correlated system: the same sample can display a record-low density superconductivity [14, 15, 16], a correlated insulator state [13, 17, 56], and perhaps even an interaction-driven ferromagnetic behavior [58, 57]. These narrow bands also offer a key advantage in the context of plasmonics: they allow for plasmonic dispersion to rise above the particle-hole continuum, entering the regime where Landau damping, a fundamental limitation on the lifespan of the plasmons, is quenched [138, 140]. These characteristics make moiré materials a perfect platform to realize nonreciprocal plasmons with long lifespan.

In this work we focus specifically on the case of TLG as it best exemplifies the key features of narrow moiré bandstructures, but lacks the additional complications stemming from multiple electron-hole bands present in the TBG bandstructure. This is

because the TLG bands can be gapped in a controllable manner using external electric field [16, 17]. We employ a continuum model [17, 64, 63] to describe the bandstructure in the mini Brillouin zone and perform a material-realistic calculation of the plasmon dispersion with and without applied electric current. These simulations show a significant magnitude of plasmon nonreciprocity, exceeding that predicted due to the conventional plasmon Doppler effect, as shown in Fig.4-3.

Our results have immediate consequences of both practical and fundamental importance. First of all, as mentioned above, they open a pathway to development of optoelectronic devices with suppressed backscattering [98, 123, 124, 125, 126], for example plasmonic isolators based on Mach-Zehnder interferometers [127, 128], making them a valuable addition to the nanophotonics toolbox. Moreover, the drift-based mechanism enables a highly tunable electrical control of nonreciprocity on a nanoscale by simply controlling the current flow in the device. This on-chip compactness and tunability are in striking contrast to the mechanisms that employ the magnetic-based approaches. Finally, introducing a nonreciprocity to the dispersion of plasmons with quenched Landau damping is particularly appealing, as it paves a way towards a practical realization of various theoretical predictions, such as the Dyakonov-Shur instability [120], that were previously limited by the plasmonic lifespan.

4.2 Minimal bandstructure model

In order to elucidate the microscopic origins of this additional source of nonreciprocity, we develop a minimal model which captures all of the features of the complicated moiré bandstructures that are relevant to plasmonic Doppler effect. Our toy-model Hamiltonian

$$H = H_0 + H_d + H_h, \tag{4.3}$$

consists of the terms

$$H_0 = \frac{k^2}{2m}\sigma_z, \quad H_d = \Delta_d\sigma_z, \quad H_h = \Delta_h\sigma_x \tag{4.4}$$

that give rise to two touching parabolic bands with two possible types of gap-opening: H_d and H_h. Here m is the effective mass and $\sigma_{x,y,z}$ are the Pauli matrices. These parabolas can be thought of as coming from a two-band tight-binding model described in the Appendix 4.9.1. Nevertheless, it is sufficient to consider them as a starting point of the analysis with the stipulation that the effective mass m is large enough such that the plasmons can extend above the intraband particle-hole continuum of each band. The two gap-opening mechanisms: H_d, a trivial displacement-field-like gap, and H_h, a band hybridization term, are necessary to accurately describe the presence of an energy gap separating the flat band (or bands) from the rest of the energy spectrum in the moiré materials, see Fig.4-2a. They also serve a purpose in illustrating the difference between the conventional and quantum corrections to plasmon dispersion. We label the electron energies

$$E_{s,\mathbf{k}} = s\sqrt{\Delta_h^2 + H_{\mathbf{k}}^2}, \quad H_{\mathbf{k}} \equiv k^2/2m + \Delta_d \tag{4.5}$$

and Bloch eigenstates $\psi_{s,\mathbf{k}}$

$$\psi_{s,\mathbf{k}} = \frac{1}{\sqrt{2E_{s,\mathbf{k}}\left(E_{s,\mathbf{k}} + H_{\mathbf{k}}\right)}} \begin{pmatrix} H_{\mathbf{k}} + E_{s,\mathbf{k}} \\ \Delta_h \end{pmatrix}. \tag{4.6}$$

with a momentum $\mathbf{k}$ and a band index $s = \pm$ corresponding to the conduction $(+)$ and valence $(-)$ bands of the toy-model. A schematic depiction of the bandstructure is shown in Fig.4-2a. To reproduce the physics of narrow-band plasmons in moiré materials, we place the Fermi energy μ inside the valence band. This assumes then that the valence band of the toy-model qualitatively corresponds to either the flat band of the TLG [17] or the electron band of the TBG [60].

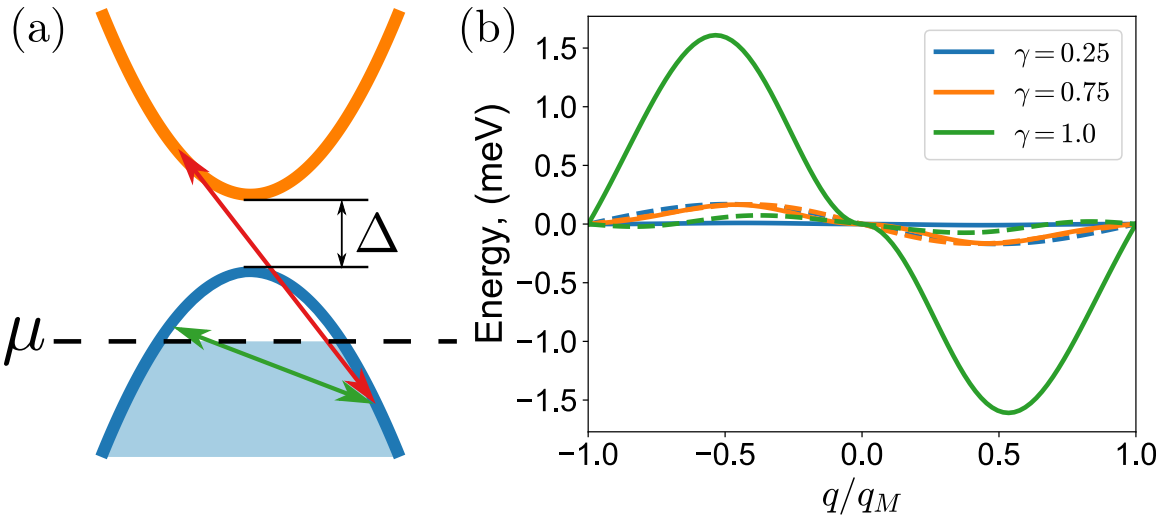

Figure 4-2: (a) Schematic depiction of intraband transitions (green) and interband transitions (red). The contribution of the latter to the polarization function is suppressed for ω smaller than the band gap $\Delta = 2\sqrt{\Delta_d^2 + \Delta_h^2}$. (b) Shift of the plasmon dispersion due to the "Quantum Doppler effect" (solid line), $\Delta\omega_{\rm p}^{(q)}(\mathbf{q})$, and the conventional Doppler effect (dashed line), $\Delta\omega_{\rm p}^{(c)}(\mathbf{q})$, for different strengths of band hybridization γ as calculated numerically using the tight-binding model. Here the gap parameters Δ_h and Δ_d are chosen as $\Delta_h = \gamma\Delta$ and $\Delta_d = \sqrt{1-\gamma^2}\Delta$, and hence preserving the gap $\Delta = 2\sqrt{\Delta_d^2 + \Delta_h^2}$ between the two bands.

4.3 Plasmons in narrow-band materials

Collective charge modes correspond to the nodes of the dynamical dielectric function $\varepsilon(\omega, \mathbf{q})$ defined as

$$\varepsilon(\omega, \mathbf{q}) = 1 - V_{\mathbf{q}}\Pi(\omega, \mathbf{q}). \tag{4.7}$$

Here $V_{\mathbf{q}} = 2\pi e^2/\kappa q$ is the Coulomb potential describing interaction between charge carries constrained to a surface of a 2D material which field lines however extend also into the surrounding medium with a relative permittivity κ. We approximate the electron polarization function $\Pi(\omega, \mathbf{q})$ with the random phase approximation [4]

$$\Pi(\omega, \mathbf{q}) = 4\sum_{\mathbf{k},s,s'} \frac{(f_{s,\mathbf{k}+\mathbf{q}} - f_{s',\mathbf{k}})F^{ss'}_{\mathbf{k}+\mathbf{q},\mathbf{k}}}{E_{s,\mathbf{k}+\mathbf{q}} - E_{s',\mathbf{k}} - \omega - i0}, \tag{4.8}$$

where summation $\sum_{\mathbf{k}}$ denotes integration over the Brillouin zone (BZ) and the indices s, s' run over electron bands. The factor of 4 in front of the summation accounts for the

four-fold spin/valley degeneracy of the toy-model included to mimic the degeneracy of the TLG/TBG superlattices. Here $f_{s,\mathbf{k}}$ is the Fermi-Dirac distribution, and $F^{ss'}_{\mathbf{k+q},\mathbf{k}}$ describes the overlap between the Bloch eigenstates

$$F^{ss'}_{\mathbf{k+q},\mathbf{k}} = |\langle\psi_{s,\mathbf{k+q}}|\psi_{s',\mathbf{k}}\rangle|^2 = \tag{4.9}$$
$$= \frac{\left((E_{s,\mathbf{k+q}} + H_{\mathbf{k+q}})(E_{s',\mathbf{k}} + H_{\mathbf{k}}) + \Delta_h^2\right)^2}{4E_{s,\mathbf{k+q}}E_{s',\mathbf{k}}(E_{s,\mathbf{k+q}} + H_{\mathbf{k+q}})(E_{s',\mathbf{k}} + H_{\mathbf{k}})},$$

which presence in the polarization function, as we will see, is crucial for the appearance of the quantum contribution to the Doppler effect.

4.4 Drift induced modifications to polarization function

To account for the influence of the electric field on the electron system it is necessary to modify the Fermi-Dirac distribution in the above definition of the polarization function [111, 114]. To leading order in the strength of the field, an electric field $\mathbf{E}$ induces a shift of the Fermi sea by a momentum $\delta_{\mathbf{k}} = -e\mathbf{E}\tau$, see the inset of Fig.4-1b. Here τ is a characteristic momentum relaxation timescale which underlying microscopic form may be highly nontrivial. We sidestep this difficulty by parametrising the momentum shift instead as $\delta_{\mathbf{k}} = -m\mathbf{u}$ with $\mathbf{u}$ being the experimentally determined drift velocity. The effect of the electron drift onto the polarization function is then simply given by a replacement

$$f_{s,\mathbf{k}} \to f_{s,\mathbf{k}+\delta_{\mathbf{k}}} \tag{4.10}$$

made in both distribution functions in Eq.(4.8).

4.5 Origins of plasmonic nonreciprocity

We now focus on explaining the behavior of the plasmon modes in this toy-model. To that end we rewrite the polarization function from Eq.(4.8) by carrying a replacement

$\mathbf{k}+\mathbf{q}\to\mathbf{k}$ and $s\to s'$ in the first fraction with the $f_{s,\mathbf{k}+\mathbf{q}}$ distribution function. This yields an expression

$$\Pi(\omega,\mathbf{q}) = 4\sum_{\mathbf{k},s,s'} f_{s,\mathbf{k}-m\mathbf{u}}\left(\frac{F^{ss'}_{\mathbf{k},\mathbf{k}-\mathbf{q}}}{E_{s,\mathbf{k}}-E_{s',\mathbf{k}-\mathbf{q}}-\omega-i0}+\right.$$
$$\left.-\frac{F^{ss'}_{\mathbf{k},\mathbf{k}+\mathbf{q}}}{E_{s',\mathbf{k}+\mathbf{q}}-E_{s,\mathbf{k}}-\omega-i0}\right), \tag{4.11}$$

which we proceed to expand in the long wavelength limit. In the small-q limit the energy associated with the intraband transitions will be always smaller than the frequency ω, while the energy of the interband transitions will be always larger than ω, see Fig.4-2a. It is therefore sufficient to focus on the intraband contribution to the polarization function only as the interband terms will be suppressed by the large denominator on the order of the bandgap energy scale. We expand the intraband terms in Eq.(4.11) in powers of ω and, keeping only first three terms in the series, we obtain

$$\Pi(\omega,\mathbf{q}) \approx \frac{A_1(\mathbf{q})}{\omega}+\frac{A_2(\mathbf{q})}{\omega^2}+\frac{A_3(\mathbf{q})}{\omega^3}, \tag{4.12}$$

where the coefficients in the above expansion are

$$A_n(\mathbf{q}) = 4\sum_{\mathbf{k}}\tilde{f}_{\mathbf{k}}\left(F^{--}_{\mathbf{k},\mathbf{k}+\mathbf{q}}\Delta E^{n-1}_{\mathbf{k}+\mathbf{q},\mathbf{k}}-F^{--}_{\mathbf{k},\mathbf{k}-\mathbf{q}}\Delta E^{n-1}_{\mathbf{k},\mathbf{k}-\mathbf{q}}\right) \tag{4.13}$$

with $\Delta E^n_{\mathbf{k},\mathbf{k}'}\equiv(E_{-,\mathbf{k}}-E_{-,\mathbf{k}'})^n$ corresponding to the nth power of the energy difference of the intraband transitions and, for clarity, we introduced a shorthand $\tilde{f}_{\mathbf{k}}\equiv f_{-,\mathbf{k}-m\mathbf{u}}$ for the drift-modified distribution function from Eq.(4.10). We reiterate that these expressions rely on the Fermi energy μ being located in the valence band $s=-$ and hence making the conduction band completely unoccupied at low temperatures.

In seeking a closed form of the coefficients $A_n(\mathbf{q})$ we focus on the most insightful limit of $|\mu|\gg\Delta_d,\Delta_h$. The largest energy scale that controls the behavior of the expansion coefficients $A_n(\mathbf{q})$ is then the Fermi energy. As such, we can therefore expand the band overlap factors and the energy differences in the small-q limit and then subsequently focus only on the leading $\mathbf{k}$ behavior of the $A_n(\mathbf{q})$ coefficients. In

practice this translates to simply approximating the exact electron energies $E_{s,\mathbf{k}}$ as parabollicaly dispersing carriers. This yields the following expression for the energy difference

$$\Delta E_{\mathbf{k+q},\mathbf{k}} \approx \frac{-q^2}{2m} - \frac{kq}{m}\cos\theta \tag{4.14}$$

and the band overlap factors

$$F^{--}_{\mathbf{k+q},\mathbf{k}} \approx 1 - \frac{4\Delta_h^2 m^2 q^2 \cos\theta}{k^6}\left(\cos\theta + \frac{q}{k}(1-4\cos^2\theta)\right) . \tag{4.15}$$

In the above we introduced an angle θ between the vectors $\mathbf{k}$ and $\mathbf{q}$. Note that in the limit of $\Delta_h \to 0$ intraband overlap approaches $F^{--}_{\mathbf{k},\mathbf{k+q}} \to 1$. This is to be expected as in the limit of $\Delta_h \to 0$ the two bands of the toy-model H become unhybridized - the matrix H is diagonal. We pause here to note that the apparent divergence of the band overlap factor, Eq.(4.15), as momentum $k \to 0$ is a consequence of the assumption $|\mu| \gg \Delta_d, \Delta_h$. This is a justified approximation as in practice, upon summation over the BZ, the contribution of the band overlap factors to the polarization function will be dominated by the momenta k close to the Fermi momentum k_F.

We begin with the $A_1(\mathbf{q})$ coefficient which turns out to be the one responsible for the additional quantum source of nonreciprocity. The difference of the band overlap factors in Eq.(4.13),

$$F^{--}_{\mathbf{k},\mathbf{k+q}} - F^{--}_{\mathbf{k},\mathbf{k-q}} \approx \frac{8\Delta_h^2 m^2 \cos\theta\,(4\cos^2\theta - 1)}{k^7} q^3 \tag{4.16}$$

projects only odd $\mathbf{k}\cdot\mathbf{q}$ components. For the integration over the direction of $\mathbf{k}$ in Eq.(4.13) not to vanish the Fermi-Dirac term $\tilde{f}_{\mathbf{k}}$ has to similarly contribute an odd harmonic of $\mathbf{k}$. As required when $\mathbf{u} = 0$, that is TRS is not broken, the Fermi surface is an even harmonic of $\mathbf{k}$ and hence the $1/\omega$ term is absent [141]. With $\mathbf{u} \neq 0$ however we expect the Fermi-Dirac distribution to develop odd harmonics linear in $\mathbf{u}$ that are centered near the Fermi momentum k_F. At zero temperature we can model such

shifted Fermi-Dirac distribution $\tilde{f}_{\mathbf{k}}$ as an θ angle dependent Heaviside function

$$\tilde{f}_{\mathbf{k}} = -\Theta\left(k_F + mu\cos(\theta_u - \theta) - k\right). \tag{4.17}$$

We choose a coordinate system such that θ, θ_u are the angles between $\mathbf{q}$ and vectors $\mathbf{k}$, and $\mathbf{q}$ and $\mathbf{u}$, respectively. Here the negative sign in front of the Heaviside function stems from setting the charge neutrality point at $\mu = 0$. This yields

$$A_1(\mathbf{q}) \approx -\frac{2}{\pi}\frac{\Delta_h^2 u q^3 \cos(\theta_u)}{|\mu|^3} \tag{4.18}$$

for the $A_1(\mathbf{q})$ term where we approximated Fermi energy as $|\mu| \approx k_F^2/2m$. We now clearly see that if there is no hybridization between the bands, $\Delta_h = 0$, then the $1/\omega$ contribution to the polarization vanishes.

Following the same approach, we now evaluate the next two coefficients $A_2(\mathbf{q})$ and $A_3(\mathbf{q})$, which give rise to the electric field independent part of the plasmon dispersion $\omega_p^0(\mathbf{q})$ and the conventional Doppler effect, respectively. To the leading non-vanishing order in $\mathbf{q}$ we can set the band overlap factors in Eq.(4.13) as unity. Using the parabolic energy dispersion approximation we find

$$A_2(\mathbf{q}) \approx \frac{2}{\pi}|\mu|q^2, \quad A_3(\mathbf{q}) \approx -\frac{4}{\pi}u\cos\theta_u|\mu|q^3\,. \tag{4.19}$$

The q^2 form of the $A_2(\mathbf{q})$ is to be expected from the classical "acceleration" [4] result just as the result that the contribution of the $A_3(\mathbf{q})$, and in fact also the $A_1(\mathbf{q})$ term, enters the polarization function at the order of q^3. This is because the lowest possible contribution to the polarization function always is of the order q^2 and thus the first term which can be an odd function of the angle $\cos(\theta_u)$ has to scale as q^3.

With the $A_n(\mathbf{q})$ coefficients known in a closed form, we are now in position to obtain the plasmon dispersion ω_p analytically. To that end we seek zeros of the dielectric function which in terms of the $A_n(\mathbf{q})$ coefficients becomes now a cubic

equation

$$0 = \omega^3 - \frac{2\pi\alpha v_F}{q}\left(A_1(\mathbf{q})\omega^2 + A_2(\mathbf{q})\omega + A_3(\mathbf{q})\right) \tag{4.20}$$

with $v_F = k_F/m$. Since $A_1(\mathbf{q})$ and $A_3(\mathbf{q})$ are both functions of the drift velocity u, they are a parametrically small correction to the dispersion as compared to the $A_2(\mathbf{q})$ term. We note in passing that the $A_1(\mathbf{q})$ coefficient enters as a prefactor of larger power of ω than the term $A_2(\mathbf{q})$ which defines the unperturbed plasmon energy scale $\omega_{\rm p}^0(\mathbf{q})$. This is in contrast to the $A_3(\mathbf{q})$ term responsible for the conventional Doppler effect, which enters as a lower power of ω and hence is suppressed by the large $\omega_{\rm p}^0(\mathbf{q})$ energy scale. Solving the equation Eq.(4.20) perturbatively in the powers of the electron drift velocity u we find the plasmon dispersion as

$$\omega_{\rm p}(\mathbf{q}) \approx \sqrt{2\pi\alpha v_F A_2/q} + \pi\alpha v_F A_1/q + \frac{A_3}{2A_2} + \mathcal{O}(u^2)\,, \tag{4.21}$$

where $A_1(\mathbf{q}$ and $A_3(\mathbf{q})$ are both linear functions of the drift velocity. Using the $A_n(\mathbf{q})$ coefficients from Eq.(4.18) and Eq.(4.19) in the above solution gives the expression

$$\omega_{\rm p}(\mathbf{q}) \approx \sqrt{4\alpha|\mu|v_F q} - 2\alpha\frac{\Delta_h^2 v_F q}{|\mu|^3}\mathbf{u}\cdot\mathbf{q} - \mathbf{u}\cdot\mathbf{q}\,, \tag{4.22}$$

which is the central result of our work. It is the last two terms in the above expression that are behind the plasmonic nonreciprocity in the presence of electron drift in a solid-state system.

4.6 Quantum Doppler Effect

The second term in the Eq. (4.22) is the new source of plasmonic nonreciprocity which dominates over the conventional Doppler effect in narrow-band materials. To see this we discuss the dependence of the Doppler corrections in Eq.(4.22) on the system parameters. The conventional Doppler shift contribution, last term, does not depend on the system parameters beyond the drift velocity u and thus its magnitude

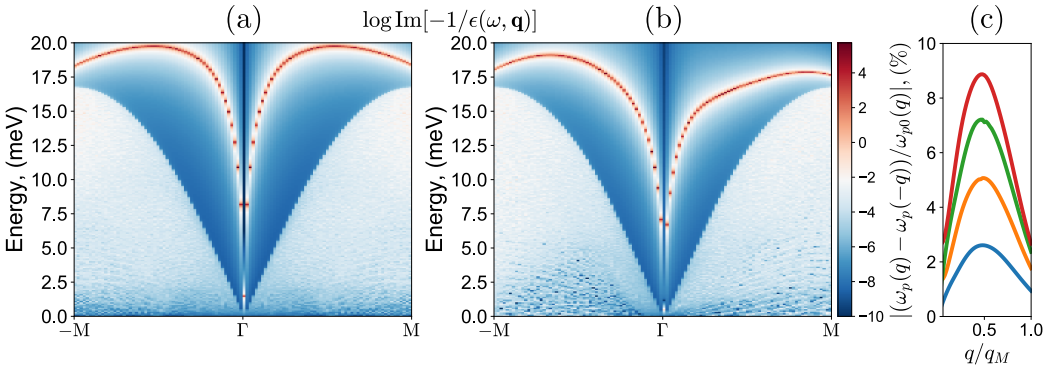

Figure 4-3: Electron loss function in an ABC stacked trilayer graphene (a) without and (b) with an applied electric field. The plasmon dispersion (sharp red feature) exhibits a nonreciprocity in its dispersion. Here the Fermi surface shift is $\delta_{\mathbf{k}} = 0.2 q_M$. (c) Relative nonreciprocity for several values of the Fermi surface shifts $\delta_{\mathbf{k}} = c\, q_M$, with $c = 0.05, 0.1, 0.15, 0.2$ and $q_M = 0.24$ nm^{-1}.

is weakly tunable. For $q \sim k_F$ it is a fraction of the chemical potential,

$$\Delta\omega_p^{(c)} \approx u k_F \approx \frac{u}{v_F}|\mu|\,, \quad |\mu| \approx v_F k_F\,, \tag{4.23}$$

as the drift velocity u is always smaller than the Fermi velocity v_F. This is in stark contrast to the the quantum contribution, the penultimate term in the above expression, where the magnitude of the effect can be drastically changed with effective fine structure constant α. At momenta $q \sim k_F$ the magnitude of the effect is

$$\Delta\omega_p^{(q)} \approx 2\alpha \frac{u}{v_F} \frac{\Delta_h^2 v_F^2 k_F^2}{|\mu|^3} \approx 2\alpha \frac{u}{v_F} \frac{\Delta_h^2}{|\mu|}\,, \tag{4.24}$$

again using $|\mu| \approx v_F k_F$, and thus a large α offers a parametric increase of the effect over the initial smallness of the drift to Fermi velocity ratio. This is exactly the behavior seen in narrow-electron band systems where effective fine structure constant satisfies $\alpha \gg 1$.

We pause here to draw attention to the q dependence of the analytic expressions for both Doppler effect contributions: $\omega_p^{(c)}$ from (4.1) and $\omega_p^{(q)}$ (4.2). The Quantum Doppler effect enters at a higher power of momentum, $\omega_p^{(q)} \propto q^2$, making it at first glance seem to be smaller than the conventional Doppler contribution, $\omega_p^{(c)} \propto q$. This difference in the powers of momentum q in both terms can be traced back to

the division by the $A_2(\mathbf{q})$ term, c.f. Eq.(4.21), as both $A_1(\mathbf{q})$, given by Eq.(4.18), and $A_3(\mathbf{q})$, given by Eq.(4.19), enter as the same power of momentum q. This lack of division in the $\omega_p^{(q)}$ term by the factor $A_2(\mathbf{q})$, which sets the scale for the main drift-free part of the plasmon dispersion ω_p^0, is ultimately behind the parametric enhancement of the Quantum Doppler effect contribution by the large effective fine structure constant α. As we will see later, this large factor of α overcomes the nominal suppression stemming from the additional factor of q/k_F present in the Quantum Doppler contribution term for plasmon frequencies larger than the chemical potential, $\omega_p(\mathbf{q}) \gtrsim |\mu|$.

To further demonstrate this point, and avoid the approximations that were necessary for the analytical derivation, we perform numerical calculations based on the narrow-band tight-binding model described in Appendix 4.9.1. An example of the plasmonic dispersion in the absence of electric current is shown in Fig.4-1(a, c) for two parameter regimes of the model: one with strongly hybridized bands due to Δ_h term, and the other with decoupled bands that are simply displaced by a finite energy Δ_d. In both scenarios the parameters are chosen to keep the same bandwidth and bandgap of 10 meV. In this case, both regimes exhibit qualitatively similar behavior - the energies of the plasmons settle between the intra- and inter-band particle-hole continua as guaranteed by $\alpha \gg 1$ [138]. However, when electric current is introduced, the striking difference between them is immediately apparent. While in the unhybridzed case the observed nonreciprocity is minute, Fig.4-1(c), in the system with hybridized bands a strong asymmetry in plasmon dispersion arises, see Fig.4-1(d). The magnitude of the nonreciprocity can be quantified by calculating the dispersion asymmetry between the $\mathbf{q}$ and $-\mathbf{q}$ modes

$$\frac{\omega_p(\mathbf{q}) - \omega_p(-\mathbf{q})}{\omega_p^0(\mathbf{q})}\,, \tag{4.25}$$

which we display in Fig.4-1(e) for both cases. While the plasmonic Doppler effect is present in both cases, the calculation in a strongly hybridized system reveals a striking enhancement by an order of magnitude over the unhybridized one in agreement with

the analytical calculation. This comparison between the conventional and the Quantum Doppler effect is further exemplified by the crossover from the strongly to weakly hybridized system shown in Fig.4-2(b), again while keeping constant bandwidths and bandgaps for all 3 values of parameter γ that controls the degree to which bands are hybridized or just trivially displaced in energy (see the caption of Fig.4-2(b)). We show there the $\Delta\omega_p^{(c)} = A_3/2A_2$ and $\Delta\omega_p^{(q)} = \pi\alpha v_F A_1/q$ components separated, with a clear domination of the latter over the former contribution evident when the bands are strongly hybridized.

It is crucial to stress that the presence of the $A_1(\mathbf{q})$ term responsible for the additional "quantum" contribution to the Doppler effect is not just a special feature of our model, but is universal to any systems with hybridized bands. In fact, the $A_1(\mathbf{q})$ coefficient is also present in the graphene Doppler shift calculations [111, 114], but because the relevant plasmon frequencies are smaller or comparable to the Fermi energy $\omega_p \lesssim |\mu|$, the $A_1(\mathbf{q})$ term is suppressed by a small ratio of q^2/k_F^2. More generally, the origins of the $A_1(\mathbf{q})$ coefficient lie solely in the non-vanishing of a difference of the band overlap functions $F^{ss'}_{\mathbf{k},\mathbf{k}+\mathbf{q}}$. This overlap is a measure of the extent to which wave functions' spectral weight at different momenta come from the same unhybridized bands and so it is strongly dependent on the band hybridization, see Fig.4-2(b), reaching unity far from the band crossing points as chemical potential $|\mu|$ becomes larger. Indeed it is the relation between the chemical potential and the plasmon frequency which determines the crossover to the regime in which quantum contribution starts to dominate,

$$\Delta\omega_{\mathrm{p}}^{(q)}(\mathbf{q}) \gtrsim \Delta\omega_{\mathrm{p}}^{(c)}(\mathbf{q}) \Rightarrow \omega_p^0(\mathbf{q}) \gtrsim |\mu|, \tag{4.26}$$

as indicated in the calculation in the Fig.4-1c.

4.7 Doppler effect in moiré materials

We turn now to a particular material realization of this phenomenon. We consider ABC stacked trilayer graphene (TLG), which has been recently shown to host narrow bands due to moiré superlattice effects [16, 17]. In order to evaluate the polarization function for a realistic bandstructure model [64, 63] it is necessary to slightly generalize the definition of the polarization function from Eq.(4.8). The only required changes are: inclusion of multiple electron and hole bands in both K and K' valleys of TLG and a change in the definition of the band overlap factors $F^{nm}_{\mathbf{k+q},\mathbf{k}}$:

$$F^{nm}_{\mathbf{k+q},\mathbf{k}} = \left| \int_\Omega d^2 r \Psi^\dagger_{n,\mathbf{k+q}}(\mathbf{r}) e^{i\mathbf{q}\cdot\mathbf{r}} \Psi_{m,\mathbf{k}}(\mathbf{r}) \right|^2 \tag{4.27}$$

In the above expression, n, m run over all the bands in both valleys, $\Psi_{m,\mathbf{k}}(\mathbf{r})$ represents the Bloch wave function for band m and the integration is over moiré unit cell Ω. To obtain electron Bloch wavefunctions and their energies we use the continuum model introduced in Ref.[16, 17], which description we reproduce in the Appendix. This model is spin-degenerate, which is taken into account by including a multiplying factor of 2 in the polarization function. With such changes to the polarization function we can numerically evaluate the the dielectric function and determine plasmon dispersion from its nodes.

The results of such a realistic material calculations are shown in Fig. 4-3(a, b) which demonstrate the plasmon dispersion in TLG without and with electric current, respectively. As in the tight binding model, an asymmetry $\omega_{\mathrm{p}}(\mathbf{q}) \neq \omega_{\mathrm{p}}(-\mathbf{q})$ develops due to the flowing electric current. In analysing this figure it is insightful to compare it with the Fig.4-1(c, d) which reproduces qualitative features of the TLG calculation. Most crucially, we see a plasmon mode which rises above the particle-hole continuum and only once the mode $\omega_{\mathrm{p}}(\mathbf{q})$ is above the Fermi energy $|\mu|$ does a strong nonreciprocity in its dispersion develop. This behavior is to be expected on the basis of the analysis leading to Eq.(4.26) discussed in the previous section.

In Fig. 4-3(b) we see by evaluating the nonreciprocity measure of Eq.(4.25) that

even for a quantitatively accurate bandstructure model and practical drift velocities the induced nonreciprocity is a significant correction to the plasmon dispersion much exceeding any, even optimistic, conventional Doppler effect predictions. We underline however again that the enhancement of the Doppler effect from Eq.(4.2) is a general feature of systems with narrow, strongly hybridized bands and thus not limited to TLG - we expect it to be present, and perhaps even more pronounced, in any material with these characteristics.

4.8 Outlook

A key feature shared by many moiré materials is their remarkable flat electron bands with extremely low Fermi velocity and, therefore, exceptionally large effective fine structure constant values α. In this work we showed how strong interactions lead to a new, significant source of plasmon nonreciprocity, which enables development of opto-electronic devices with unidirectional propagation, such as plasmonic isolators based on Mach-Zehnder interferometers[127, 128]. Moreover, introducing a nonreciprocity to the dispersion of intrinsically undamped plasmons[138] is particularly exciting as it paves way towards a practical realization of various theoretical predictions, such as the Dyakonov-Shur instability [120] that were previously limited by the plasmonic lifespan. As the collective modes in the moiré materials are actively searched for using near-field optical microscopy techniques [50, 49, 76, 142], this work can open new prospects for both fundamental and practical applications of moiré plasmons.

4.9 Appendix

4.9.1 The tight-biding model

To compare and contrast the quantum and conventional plasmonic Doppler effect we use a simple tight-binding model in which we try to retain some features of the true TLG bands. The key properties of the bandstructure that control the behavior of the collective modes are the electron band's bandwidth (a natural bandstructure cut-

off), momentum scale, and similar symmetry properties. For this purpose we we use a nearest neighbor tight-binding model on a triangular lattice with two orbitals per site. For clarity, we use hoppings of equal magnitude, but opposite sign ($t_1 = -t_2 = t$), arriving at:

$$H_{TB} = -2t\left(\cos(k_x a) + 2\cos\left(\frac{k_x a}{2}\right)\cos\left(\frac{k_y a\sqrt{3}}{2}\right)\right)\sigma_z + \Delta_d\sigma_z + \Delta_h\sigma_x \tag{4.28}$$

Here the lattice constant $a = 15$nm and σ_i are the Pauli matrices. In Fig.4-1(a), (b) the hopping magnitude is $t = 2.3\,\text{meV}$, while the gap parameters are $\Delta_d = -3\,\text{meV}$ and $\Delta_h = 10\,\text{meV}$, and the calculation is performed for $\mu = -14.5\,\text{meV}$. For the comparison of the magnitude of nonreciprocity between hybridized and unhybridized cases of Fig.4-1(c) we also use $t = 1.1\,\text{meV}$, $\Delta_d = 10\,\text{meV}$ and $\Delta_h = 0\,\text{meV}$ to obtain the unhybridized bands of comparable bandwidth. In Fig.4-2(b), where we show the quantum and conventional contributions to the plasmonic nonreciprocity we keep the bandwidth W and bandgap Δ at 10 meV while we tune between two types of the gap sources using parameter γ:

$$\Delta_h = \gamma\Delta, \quad \Delta_d = \sqrt{1-\gamma^2}\Delta \tag{4.29}$$

As indicated in the text we make the tight-binding simulation 4-fold degenerate to mimic the valley/spin degeneracy present in an actual TLG system.

4.9.2 TLG - details of the model

For the description of the TLG bandstructure and eigenstates we employ the effective continuum Hamiltonian [17, 64, 63], together with its associated notation and numerical values of simulation parameters. It consists of two parts $H_{\text{TLG}} = H_{\text{ABC}} + V_M(\mathbf{r})$, the first one describing the ABC-stacked trilayer graphene and the second one being due to moiré potential of hBN substrate. The trilayer graphene part is given by:

$$H_{\mathrm{ABC}} = \frac{\nu_0^3}{t_1^2}\begin{pmatrix} 0 & k_+^3 \\ k_-^3 & 0 \end{pmatrix} + \left(\frac{2\nu_0\nu_3 k^2}{t_1} + t_2\right)\sigma_x + \left(\frac{2\nu_0\nu_4 k^2}{t_1} - \Delta'\right)\sigma_0 + \left(\frac{3\nu_0^2 k^2}{t_1^2} + t_2\right)\Delta''\sigma_0 - \Delta\sigma_z \tag{4.30}$$

where $k_\pm = \xi k_x \pm i k_y$, $\xi = \pm 1$ for K and K' valleys, $\nu_n = \sqrt{3}/2at_n$, $a = 0.246$nm is the carbon-carbon lattice spacing and $t_0 = 2.62$eV, $t_1 = 0.358$eV, $t_2 = -0.0083$eV, $t_4 = 0.293$eV, $t_5 = 0.144$eV, $\Delta' = 0.0122$eV, $\Delta'' = -0.0095$eV. Finally, the gaps in the bandstructure are opened and controlled by the applied electric field, which is described by $\Delta = 50\,\mathrm{meV}$ in our case to enlarge the range of energies between the intra- and interband continua. The moiré potential is given by:

$$V_M(\mathbf{r}) = 2C_A \mathrm{Re}(e^{i\varphi_A} f(\mathbf{r}))\begin{pmatrix} 1 & 0 \\ 0 & 0 \end{pmatrix} \tag{4.31}$$

where $f(\mathbf{r}) = \sum_{j=1}^{6} e^{i\mathbf{q}_j\mathbf{r}}(1 + (-1)^j)/2$ and $\mathbf{q}_j$ are the reciprocal lattice vectors of the triangular moiré supperlattice. The parameters used in the calculation of this potential are $C_A = -14.88$meV and $\varphi_A = 50.19°$. We obtain the energies and the eigenstates of H_{TLG} by numerical diagonalization using a momentum cutoff $q_C = 5|\mathbf{q}_j|$. In all the calculations we are summing the results over both valleys and we take into account the 10 bands that lie the closest to the Fermi energy in order to consider all the relevant interband transitions. The Bloch wavefunction for a valley ξ is taken as

$$\Psi^X_{\xi,n,\mathbf{k}}(\mathbf{r}) = \sum_{\mathbf{G}} C^X_{\xi,n,\mathbf{k}}(\mathbf{G}) e^{i(\mathbf{k}+\mathbf{G})\cdot\mathbf{r}} \tag{4.32}$$

with X corresponding to each of the spinor components $X = A, B$. The band index is labeled by n and $\mathbf{k}$ is the Bloch wave vector in the moiré superlattice Brillouin zone. Here $\mathbf{G}$ runs over all possible integer combinations of the reciprocal lattice vectors, $\mathbf{G} = m_1\mathbf{G}_1^M + m_2\mathbf{G}_2^M$ with integer m_1 and m_2 that satisfy the momentum cutoff condition.

Chapter 5

Conclusions

The family of moiré materials, in particular the magic angle twisted bilayer graphene, is an excellent platform to study strongly interacting physics. In the thesis we analyzed the interplay of narrow electron bands and strong electron-electron interactions on the dynamical dielectric properties of these electronic systems. More specifically, we investigated properties of collective modes in these materials.

The main finding of the thesis is that strong electron-electron interactions give rise to a new type of plasmon behavior. These new plasmons pierce through the p-h continuum and extend in the forbidden energy band above it to decouple from p-h excitations. The decoupling from the spectrum of p-h excitations quenches Landau damping giving rise to long-lived plasmonic excitations.

In Chapter 2, the over-the-band plasmon modes were first derived and their smoking gun experimental signatures, speckle patterns, were identified. We analyzed the origins of the over-the-band modes to demonstrate the strong dependence on the effective fine structure constant α which quantifies the strength of electron-electron interactions. The analysis was first carried out with a help of a simple toy-model of TBG's bandstructure that allowed to identify the necessary ingredients for a system to exhibit over-the-band modes. We then introduced a realistic TBG continuum bandstructure model and used it to determine the dispersion of plasmons in MATBG demonstrating the presence of over-the-band modes.

To confirm robustness of the RPA analysis, in Chapter 3, we again studied the

collective modes in a narrow band system by focusing on a solvable model of a Wigner crystal. Strong interactions give rise to formation of an electron solid, the Wigner crystal, which collective modes are simply the oscillations of the electron lattice: phonons. With help of this model we identified the microscopic origins of the over-the-band modes as coming from strong coupling between electron-hole pairs.

In Chapter 3, we considered also the collective modes inside a correlated insulator. We found that the over-the-band plasmon behavior is robust with only the subtle details of the plasmon stiffness being dependent on the type of the low-energy order present in the system. It is this sensitivity, albeit subtle, to the nature of the low-energy state that should allow the over-the-band plasmons to be used as an experimental probe of the correlated state.

The final Chapter 4 of the thesis focuses on one application of the moiré over-the-band plasmons. A new mechanism for plasmon nonreciprocity is presented which exists in systems with strongly hybridized electron bands. The magnitude of the effect is controlled by the strength of electron-electron interactions α, which makes it particularly pronounced in the moiré materials.

This new scheme of constructing over-the-band plasmons introduced in the thesis is very fundamental. It is therefore interesting to ask what other collective modes can benefit from this dissipation-quenching mechanism. It is also very inviting to study what ultimately controls the lifespan of such plasmons, that is to incorporate processes beyond those that are accounted through the single pair-production damping mechanisms of the RPA. Lastly, an exciting consequence of the thesis which is worth exploring, is to apply the acquired understanding of the dynamical dielectric function of a narrow-electron band system and its collective modes to study superconducting properties of moiré materials.

Bibliography

[1] Tonks, L. & Langmuir, I. Oscillations in ionized gases. *Phys. Rev.* **33**, 195–210 (1929).

[2] Pines, D. & Bohm, D. A collective description of electron interactions: Ii. collective vs individual particle aspects of the interactions. *Phys. Rev.* **85**, 338–353 (1952).

[3] Bohm, D. & Pines, D. A collective description of electron interactions: Iii. coulomb interactions in a degenerate electron gas. *Phys. Rev.* **92**, 609–625 (1953).

[4] Mahan, G. *Many-particle physics* (Kluwer Academic/Plenum Publishers, New York, 2000).

[5] Giuliani, G. & Vignale, G. *Quantum Theory of the Electron Liquid* (2008).

[6] Tame, M. S. *et al.* Quantum plasmonics. *Nature Physics* **9**, 329–340 (2013).

[7] Duan, H., Fernández-Domínguez, A. I., Bosman, M., Maier, S. A. & Yang, J. K. W. Nanoplasmonics: Classical down to the nanometer scale. *Nano Letters* **12**, 1683–1689 (2012).

[8] Polman, A. Plasmonics applied. *Science* **322**, 868–869 (2008).

[9] Koppens, F. H. L., Chang, D. E. & García de Abajo, F. J. Graphene plasmonics: A platform for strong light–matter interactions. *Nano Letters* **11**, 3370–3377 (2011).

[10] Low, T. & Avouris, P. Graphene plasmonics for terahertz to mid-infrared applications. *ACS Nano* **8**, 1086–1101 (2014).

[11] Grigorenko, A. N., Polini, M. & Novoselov, K. S. Graphene plasmonics. *Nature Photonics* **6**, 749–758 (2012).

[12] García de Abajo, F. J. Graphene plasmonics: Challenges and opportunities. *ACS Photonics* **1**, 135–152 (2014).

[13] Cao, Y. *et al.* Correlated insulator behaviour at half-filling in magic-angle graphene superlattices. *Nature* **556**, 80 EP – (2018).

[14] Cao, Y. *et al.* Unconventional superconductivity in magic-angle graphene superlattices. *Nature* **556**, 43 EP – (2018).

[15] Yankowitz, M. *et al.* Tuning superconductivity in twisted bilayer graphene. *Science* **363**, 1059–1064 (2019).

[16] Chen, G. *et al.* Signatures of tunable superconductivity in a trilayer graphene moiré superlattice. *Nature* **572**, 215–219 (2019).

[17] Chen, G. *et al.* Evidence of a gate-tunable Mott insulator in a trilayer graphene moiré superlattice. *Nature Physics* **15**, 237–241 (2019).

[18] Burg, G. W. *et al.* Correlated insulating states in twisted double bilayer graphene. *Phys. Rev. Lett.* **123**, 197702 (2019).

[19] Grosso, G. *Solid state physics* (Academic Press, San Diego, 2000).

[20] Kittel, C. *Introduction to solid state physics* (Wiley, Hoboken, NJ, 2005).

[21] Kneipp, K. *et al.* Single molecule detection using surface-enhanced raman scattering (sers). *Phys. Rev. Lett.* **78**, 1667–1670 (1997).

[22] Talley, C. E. *et al.* Surface-enhanced raman scattering from individual au nanoparticles and nanoparticle dimer substrates. *Nano Letters* **5**, 1569–1574 (2005).

[23] Rodríguez-Lorenzo, L. *et al.* Zeptomol detection through controlled ultrasensitive surface-enhanced raman scattering. *Journal of the American Chemical Society* **131**, 4616–4618 (2009).

[24] Zheludev, N. I. A roadmap for metamaterials. *Opt. Photon. News* **22**, 30–35 (2011).

[25] Atwater, H. A. & Polman, A. Plasmonics for improved photovoltaic devices. *Nature Materials* **9**, 205–213 (2010).

[26] Novotny, L. & van Hulst, N. Antennas for light. *Nature Photonics* **5**, 83–90 (2011).

[27] Gonzalez-Tudela, A. *et al.* Entanglement of two qubits mediated by one-dimensional plasmonic waveguides. *Phys. Rev. Lett.* **106**, 020501 (2011).

[28] Savasta, S. *et al.* Nanopolaritons: Vacuum rabi splitting with a single quantum dot in the center of a dimer nanoantenna. *ACS Nano* **4**, 6369–6376 (2010).

[29] Dzsotjan, D., Sørensen, A. S. & Fleischhauer, M. Quantum emitters coupled to surface plasmons of a nanowire: A green's function approach. *Phys. Rev. B* **82**, 075427 (2010).

[30] Chang, D. E., Sørensen, A. S., Hemmer, P. R. & Lukin, M. D. Quantum optics with surface plasmons. *Phys. Rev. Lett.* **97**, 053002 (2006).

[31] Yoon, H., Yeung, K. Y. M., Kim, P. & Ham, D. Plasmonics with two-dimensional conductors. *Philosophical transactions. Series A, Mathematical, physical, and engineering sciences* **372**, 20130104–20130104 (2014).

[32] Stern, F. Polarizability of a two-dimensional electron gas. *Phys. Rev. Lett.* **18**, 546–548 (1967).

[33] Hwang, E. H. & Das Sarma, S. Dielectric function, screening, and plasmons in two-dimensional graphene. *Phys. Rev. B* **75**, 205418 (2007).

[34] Wunsch, B., Stauber, T., Sols, F. & Guinea, F. Dynamical polarization of graphene at finite doping. *New Journal of Physics* **8**, 318–318 (2006).

[35] Geim, A. K. & Grigorieva, I. V. Van der waals heterostructures. *Nature* **499**, 419–425 (2013).

[36] Castro Neto, A. H., Guinea, F., Peres, N. M. R., Novoselov, K. S. & Geim, A. K. The electronic properties of graphene. *Rev. Mod. Phys.* **81**, 109–162 (2009).

[37] Vicarelli, L. *et al.* Graphene field-effect transistors as room-temperature terahertz detectors. *Nature Materials* **11**, 865–871 (2012).

[38] McCann, E. & Koshino, M. The electronic properties of bilayer graphene. *Reports on Progress in Physics* **76**, 056503 (2013).

[39] Novoselov, K. S. *et al.* Electric field effect in atomically thin carbon films. *Science* **306**, 666–669 (2004).

[40] Zhang, Y. *et al.* Direct observation of a widely tunable bandgap in bilayer graphene. *Nature* **459**, 820–823 (2009).

[41] Gmitra, M. & Fabian, J. Graphene on transition-metal dichalcogenides: A platform for proximity spin-orbit physics and optospintronics. *Phys. Rev. B* **92**, 155403 (2015).

[42] Mattheakis, M., Tsironis, G. P. & Kaxiras, E. Graphene and active metamaterials: Theoretical methods and physical properties. In Barbillon, G. (ed.) *Nanoplasmonics*, chap. 1 (IntechOpen, Rijeka, 2017).

[43] Allen, P. B. Single particle versus collective electronic excitations. In Petru, Z., Przystawa, J. & Rapcewicz, K. (eds.) *From Quantum Mechanics to Technology*, 125–141 (Springer Berlin Heidelberg, Berlin, Heidelberg, 1996).

[44] Ritchie, R. H. Plasma losses by fast electrons in thin films. *Phys. Rev.* **106**, 874–881 (1957).

[45] Landau, L. On the vibrations of the electronic plasma. *J. Phys. (USSR)* **10**, 25–34 (1946).

[46] Malmberg, J. H. & Wharton, C. B. Collisionless damping of electrostatic plasma waves. *Phys. Rev. Lett.* **13**, 184–186 (1964).

[47] Woessner, A. *et al.* Highly confined low-loss plasmons in graphene–boron nitride heterostructures. *Nature Materials* **14**, 421–425 (2014).

[48] Ni, G. X. *et al.* Fundamental limits to graphene plasmonics. *Nature* **557**, 530–533 (2018).

[49] Fei, Z. *et al.* Gate-tuning of graphene plasmons revealed by infrared nano-imaging. *Nature* **487**, 82–85 (2012).

[50] Chen, J. *et al.* Optical nano-imaging of gate-tunable graphene plasmons. *Nature* **487**, 77–81 (2012).

[51] Mishchenko, E. G., Reizer, M. Y. & Glazman, L. I. Plasmon attenuation and optical conductivity of a two-dimensional electron gas. *Phys. Rev. B* **69**, 195302 (2004).

[52] Langer, T., Baringhaus, J., Pfnür, H., Schumacher, H. W. & Tegenkamp, C. Plasmon damping below the landau regime: the role of defects in epitaxial graphene. *New Journal of Physics* **12**, 033017 (2010).

[53] Buljan, H., Jablan, M. & Soljačić, M. Damping of plasmons in graphene. *Nature Photonics* **7**, 346–99 (2013).

[54] Bistritzer, R. & MacDonald, A. H. Moiré bands in twisted double-layer graphene. *Proceedings of the National Academy of Sciences* **108**, 12233–12237 (2011).

[55] Lopes dos Santos, J. M. B., Peres, N. M. R. & Castro Neto, A. H. Graphene bilayer with a twist: Electronic structure. *Phys. Rev. Lett.* **99**, 256802 (2007).

[56] Lu, X. *et al.* Superconductors, orbital magnets and correlated states in magic-angle bilayer graphene. *Nature* **574**, 653–657 (2019).

[57] Serlin, M. *et al.* Intrinsic quantized anomalous hall effect in a moiré heterostructure. *Science* **367**, 900–903 (2020).

[58] Sharpe, A. L. *et al.* Emergent ferromagnetism near three-quarters filling in twisted bilayer graphene. *Science* **365**, 605–608 (2019).

[59] Liu, X. *et al.* Spin-polarized Correlated Insulator and Superconductor in Twisted Double Bilayer Graphene. *arXiv e-prints* arXiv:1903.08130 (2019). .

[60] Koshino, M. *et al.* Maximally localized wannier orbitals and the extended hubbard model for twisted bilayer graphene. *Phys. Rev. X* **8**, 031087 (2018).

[61] Talantsev, E. F., Mataira, R. C. & Crump, W. P. Classifying superconductivity in moirégraphene superlattices. *Scientific Reports* **10**, 212 (2020).

[62] Lee, P. A., Nagaosa, N. & Wen, X.-G. Doping a mott insulator: Physics of high-temperature superconductivity. *Rev. Mod. Phys.* **78**, 17–85 (2006).

[63] Koshino, M. & McCann, E. Trigonal warping and Berry's phase π in ABC-stacked multilayer graphene. *Physical Review B* **80**, 165409 (2009).

[64] Zhang, F., Sahu, B., Min, H. & MacDonald, A. H. Band structure of ABC-stacked graphene trilayers. *Physical Review B* **82**, 035409 (2010).

[65] Das Sarma, S., Adam, S., Hwang, E. H. & Rossi, E. Electronic transport in two-dimensional graphene. *Rev. Mod. Phys.* **83**, 407–470 (2011).

[66] Emani, N. K. *et al.* Electrically tunable damping of plasmonic resonances with graphene. *Nano Letters* **12**, 5202–5206 (2012).

[67] Principi, A., Vignale, G., Carrega, M. & Polini, M. Bulk and shear viscosities of the two-dimensional electron liquid in a doped graphene sheet. *Phys. Rev. B* **93**, 125410 (2016).

[68] Polini, M. *et al.* Plasmons and the spectral function of graphene. *Phys. Rev. B* **77**, 081411 (2008).

[69] Yan, H. *et al.* Damping pathways of mid-infrared plasmons in graphene nanostructures. *Nature Photonics* **7**, 394–399 (2013).

[70] Principi, A., Polini, M. & Vignale, G. Linear response of doped graphene sheets to vector potentials. *Phys. Rev. B* **80**, 075418 (2009).

[71] Adler, S. L. Quantum theory of the dielectric constant in real solids. *Phys. Rev.* **126**, 413–420 (1962).

[72] Wiser, N. Dielectric constant with local field effects included. *Phys. Rev.* **129**, 62–69 (1963).

[73] Sturm, K. & Oliveira, L. E. High-frequency dielectric properties of covalent semiconductors within the nearly-free-electron approximation. i. the one-plasmon-band model. *Phys. Rev. B* **22**, 6268–6282 (1980).

[74] Oliveira, L. E. & Sturm, K. High-frequency dielectric properties of covalent semiconductors within the nearly-free-electron approximation. ii. the two-plasmon-band model. *Phys. Rev. B* **22**, 6283–6293 (1980).

[75] Stauber, T. & Kohler, H. Quasi-flat plasmonic bands in twisted bilayer graphene. *Nano Letters* **16**, 6844–6849 (2016).

[76] Hu, F. *et al.* Real-space imaging of the tailored plasmons in twisted bilayer graphene. *Phys. Rev. Lett.* **119**, 247402 (2017).

[77] Pashitskii, E. A. Plasmon mechanism of high-temperature superconductivity in cuprate metal-oxide compounds. *JETP* **76**, 425–444 (1993).

[78] Giuliani, G. F. & Vignale, G. *Quantum theory of the electron liquid* (Cambridge Univ. Press, Cambridge, 2005).

[79] Wigner, E. On the interaction of electrons in metals. *Phys. Rev.* **46**, 1002–1011 (1934).

[80] Hew, W. K. *et al.* Incipient formation of an electron lattice in a weakly confined quantum wire. *Phys. Rev. Lett.* **102**, 056804 (2009).

[81] Andrei, E. Y. *et al.* Observation of a magnetically induced wigner solid. *Phys. Rev. Lett.* **60**, 2765–2768 (1988).

[82] Shapir, I. *et al.* Imaging the electronic wigner crystal in one dimension. *Science* **364**, 870–875 (2019).

[83] Padhi, B., Setty, C. & Phillips, P. W. Doped twisted bilayer graphene near magic angles: Proximity to wigner crystallization, not mott insulation. *Nano Letters* **18**, 6175–6180 (2018).

[84] Crandall, R. S. Collective modes of a two-dimensional wigner crystal. *Phys. Rev. A* **8**, 2136–2142 (1973).

[85] Côté, R. & MacDonald, A. H. Collective modes of the two-dimensional wigner crystal in a strong magnetic field. *Phys. Rev. B* **44**, 8759–8773 (1991).

[86] Platzman, P. M. & Fukuyama, H. Phase diagram of the two-dimensional electron liquid. *Phys. Rev. B* **10**, 3150–3158 (1974).

[87] Bonsall, L. & Maradudin, A. A. Some static and dynamical properties of a two-dimensional wigner crystal. *Phys. Rev. B* **15**, 1959–1973 (1977).

[88] Moroz, S., Hoyos, C., Benzoni, C. & Son, D. T. Effective field theory of a vortex lattice in a bosonic superfluid. *SciPost Phys.* **5**, 39 (2018).

[89] Bohm, D. & Pines, D. A collective description of electron interactions. i. magnetic interactions. *Phys. Rev.* **82**, 625–634 (1951).

[90] Klitzing, K. v., Dorda, G. & Pepper, M. New method for high-accuracy determination of the fine-structure constant based on quantized hall resistance. *Phys. Rev. Lett.* **45**, 494–497 (1980).

[91] Halperin, B. I. Quantized hall conductance, current-carrying edge states, and the existence of extended states in a two-dimensional disordered potential. *Phys. Rev. B* **25**, 2185–2190 (1982).

[92] MacDonald, A. H. & Středa, P. Quantized hall effect and edge currents. *Phys. Rev. B* **29**, 1616–1619 (1984).

[93] Haldane, F. D. M. Model for a quantum hall effect without landau levels: Condensed-matter realization of the "parity anomaly". *Phys. Rev. Lett.* **61**, 2015–2018 (1988).

[94] Yu, R. *et al.* Quantized anomalous hall effect in magnetic topological insulators. *Science* **329**, 61–64 (2010).

[95] Nomura, K. & Nagaosa, N. Surface-quantized anomalous hall current and the magnetoelectric effect in magnetically disordered topological insulators. *Phys. Rev. Lett.* **106**, 166802 (2011).

[96] Wang, Q.-Z. *et al.* Quantum anomalous hall effect in magnetically doped inas/gasb quantum wells. *Phys. Rev. Lett.* **113**, 147201 (2014).

[97] Chang, C.-Z. *et al.* Experimental observation of the quantum anomalous hall effect in a magnetic topological insulator. *Science* **340**, 167–170 (2013).

[98] Ozawa, T. *et al.* Topological photonics. *Rev. Mod. Phys.* **91**, 015006 (2019).

[99] Lu, L., Joannopoulos, J. D. & Soljačić, M. Topological photonics. *Nature Photonics* **8**, 821–829 (2014).

[100] Lu, L., Joannopoulos, J. D. & Soljačić, M. Topological states in photonic systems. *Nature Physics* **12**, 626–629 (2016).

[101] Khanikaev, A. B. & Shvets, G. Two-dimensional topological photonics. *Nature Photonics* **11**, 763–773 (2017).

[102] Sun, X.-C. *et al.* Two-dimensional topological photonic systems. *Progress in Quantum Electronics* **55**, 52 – 73 (2017).

[103] Bliokh, K. Y., Rodríguez-Fortuño, F. J., Nori, F. & Zayats, A. V. Spin–orbit interactions of light. *Nature Photonics* **9**, 796–808 (2015).

[104] Song, J. C. W. & Rudner, M. S. Chiral plasmons without magnetic field. *Proceedings of the National Academy of Sciences* (2016).

[105] Shi, L.-k. & Song, J. C. W. Plasmon geometric phase and plasmon hall shift. *Phys. Rev. X* **8**, 021020 (2018).

[106] Kumar, A. *et al.* Chiral plasmon in gapped dirac systems. *Phys. Rev. B* **93**, 041413 (2016).

[107] Principi, A., Katsnelson, M. I. & Vignale, G. Edge plasmons in two-component electron liquids in the presence of pseudomagnetic fields. *Phys. Rev. Lett.* **117**, 196803 (2016).

[108] Jin, D. *et al.* Topological magnetoplasmon. *Nature Communications* **7**, 13486 (2016).

[109] Jin, D. *et al.* Infrared topological plasmons in graphene. *Phys. Rev. Lett.* **118**, 245301 (2017).

[110] Yu, Z., Veronis, G., Wang, Z. & Fan, S. One-way electromagnetic waveguide formed at the interface between a plasmonic metal under a static magnetic field and a photonic crystal. *Phys. Rev. Lett.* **100**, 023902 (2008).

[111] Borgnia, D. S., Phan, T. V. & Levitov, L. S. Quasi-Relativistic Doppler Effect and Non-Reciprocal Plasmons in Graphene. *arXiv e-prints* arXiv:1512.09044 (2015). .

[112] Duppen, B. V., Tomadin, A., Grigorenko, A. N. & Polini, M. Current-induced birefringent absorption and non-reciprocal plasmons in graphene. *2D Materials* **3**, 015011 (2016).

[113] Bliokh, K. Y., Rodríguez-Fortuño, F. J., Bekshaev, A. Y., Kivshar, Y. S. & Nori, F. Electric-current-induced unidirectional propagation of surface plasmon-polaritons. *Opt. Lett.* **43**, 963–966 (2018).

[114] Sabbaghi, M., Lee, H.-W., Stauber, T. & Kim, K. S. Drift-induced modifications to the dynamical polarization of graphene. *Phys. Rev. B* **92**, 195429 (2015).

[115] Morgado, T. A. & Silveirinha, M. G. Drift-induced unidirectional graphene plasmons. *ACS Photonics* **5**, 4253–4258 (2018).

[116] Glattli, D. C., Andrei, E. Y., Deville, G., Poitrenaud, J. & Williams, F. I. B. Dynamical hall effect in a two-dimensional classical plasma. *Phys. Rev. Lett.* **54**, 1710–1713 (1985).

[117] Mast, D. B., Dahm, A. J. & Fetter, A. L. Observation of bulk and edge magnetoplasmons in a two-dimensional electron fluid. *Phys. Rev. Lett.* **54**, 1706–1709 (1985).

[118] Heitmann, D. Two-dimensional plasmons in homogeneous and laterally microstructured space charge layers. *Surface Science* **170**, 332 – 345 (1986).

[119] Allen, S. J., Störmer, H. L. & Hwang, J. C. M. Dimensional resonance of the two-dimensional electron gas in selectively doped GaAs/AlGaAs heterostructures. *Phys. Rev. B* **28**, 4875–4877 (1983).

[120] Dyakonov, M. & Shur, M. Shallow water analogy for a ballistic field effect transistor: New mechanism of plasma wave generation by dc current. *Phys. Rev. Lett.* **71**, 2465–2468 (1993).

[121] Dorgan, V. E., Bae, M.-H. & Pop, E. Mobility and saturation velocity in graphene on SiO_2. *Applied Physics Letters* **97**, 082112 (2010).

[122] Yu, J., Liu, G., Sumant, A. V., Goyal, V. & Balandin, A. A. Graphene-on-diamond devices with increased current-carrying capacity: Carbon sp2-on-sp3 technology. *Nano Letters* **12**, 1603–1608 (2012).

[123] Manipatruni, S., Robinson, J. T. & Lipson, M. Optical nonreciprocity in optomechanical structures. *Phys. Rev. Lett.* **102**, 213903 (2009).

[124] Kamal, A., Clarke, J. & Devoret, M. H. Noiseless non-reciprocity in a parametric active device. *Nature Physics* **7**, 311–315 (2011).

[125] Hua, S. *et al.* Demonstration of a chip-based optical isolator with parametric amplification. *Nature Communications* **7**, 13657 (2016).

[126] Jalas, D. *et al.* What is —and what is not —an optical isolator. *Nature Photonics* **7**, 579–582 (2013).

[127] Yu, Z. & Fan, S. Optical isolation based on nonreciprocal phase shift induced by interband photonic transitions. *Applied Physics Letters* **94**, 171116 (2009).

[128] Fujita, J., Levy, M., Osgood, R. M., Wilkens, L. & Dötsch, H. Waveguide optical isolator based on mach–zehnder interferometer. *Applied Physics Letters* **76**, 2158–2160 (2000).

[129] Mele, E. J. Commensuration and interlayer coherence in twisted bilayer graphene. *Phys. Rev. B* **81**, 161405 (2010).

[130] San-Jose, P., González, J. & Guinea, F. Non-abelian gauge potentials in graphene bilayers. *Phys. Rev. Lett.* **108**, 216802 (2012).

[131] Fang, S. & Kaxiras, E. Electronic structure theory of weakly interacting bilayers. *Phys. Rev. B* **93**, 235153 (2016).

[132] Gullans, M., Chang, D. E., Koppens, F. H. L., de Abajo, F. J. G. & Lukin, M. D. Single-photon nonlinear optics with graphene plasmons. *Phys. Rev. Lett.* **111**, 247401 (2013).

[133] Cohen, M., Shavit, R. & Zalevsky, Z. Observing optical plasmons on a single nanometer scale. *Scientific Reports* **4**, 4096 (2014).

[134] Levitov, L. S., Shtyk, A. V. & Feigelman, M. V. Electron-electron interactions and plasmon dispersion in graphene. *Phys. Rev. B* **88**, 235403 (2013).

[135] Tomarken, S. L. *et al.* Electronic compressibility of magic-angle graphene superlattices. *Phys. Rev. Lett.* **123**, 046601 (2019).

[136] Raether, H. *Surface plasmons on smooth surfaces*, 4–39 (Springer Berlin Heidelberg, Berlin, Heidelberg, 1988).

[137] Barnes, W. L., Dereux, A. & Ebbesen, T. W. Surface plasmon subwavelength optics. *Nature* **424**, 824–830 (2003).

[138] Lewandowski, C. & Levitov, L. Intrinsically undamped plasmon modes in narrow electron bands. *Proceedings of the National Academy of Sciences* **116**, 20869–20874 (2019).

[139] Trambly de Laissardière, G., Mayou, D. & Magaud, L. Numerical studies of confined states in rotated bilayers of graphene. *Phys. Rev. B* **86**, 125413 (2012).

[140] Khaliji, K., Stauber, T. & Low, T. Plasmons and screening in finite-bandwidth 2D electron gas. *arXiv e-prints* arXiv:1910.01229 (2019). .

[141] Landau, L. D. & Lifshitz, E. M. *Electrodynamics of Continuous Media* (Pergamon, New York, 1984).

[142] Hesp, N. C. H. *et al.* Collective excitations in twisted bilayer graphene close to the magic angle. *arXiv e-prints* arXiv:1910.07893 (2019). .